Doctoral Dissertation
Doctoral Program in Mechanical Engineering (38^{th}cycle)

Structural Dynamics Design of Steam Turbine Blades with Friction Contacts for Renewable Energy

By

Enio Colonna

******

Supervisor(s):
Prof. Teresa Maria Berruti,Prof. Daniele Botto, Academic Supervisors
Ing. Francesco Bagnera, Ing. Andrea Bessone Company Supervisors

Doctoral Examination Committee:
Prof. Marcelo Braga Dos Santos, Referee, University of Uberlândia
Prof. Mario Lavella, Referee, University of Bergamo

Politecnico di Torino
2026

Declaration

I hereby declare that, the contents and organization of this dissertation constitute my own original work and does not compromise in any way the rights of third parties, including those relating to the security of personal data.
I declare that all numerical data used in this doctoral thesis are simulated and not related to the context.

Enio Colonna
2026

* This dissertation is presented in partial fulfillment of the requirements for **Ph.D. degree** in the Graduate School of Politecnico di Torino (ScuDo).

The completion of this PhD programme represents a very important milestone for me, culminating a university career marked by a passion for engineering, sacrifices and also moments of leisure.

I have certainly achieved this goal thanks to my efforts and abilities, but these are not the only things that matter. I must thank all the people who made this journey possible and who have always supported me, even in the darkest moments.

First and foremost is my family, which includes my parents, my brothers, my girlfriend and my grandmother. My parents and brothers are my biggest supporters. They have been there from day one and have given me the opportunity to follow my passions, always supporting me on all fronts.

My Loquita is my life partner. Every day I look at her and think how lucky I am to have such a wonderful, intelligent, empathetic girl by my side, who can brighten my day with just a smile. I don't consider her an external source of my success, but an integral part of my life and my goals. We share everything together, both the joyful moments and the most difficult ones, which makes her truly my girlfriend.

Last but not least, I would like to thank my grandmother, who taught me true values and opened my eyes to what really matters in life. Unfortunately, she is no longer with us, but I am sure she is looking down on me with pride, knowing that she raised a son who has given me a full life rich in authentic happiness.

I would also like to thank my friends, who have always given me days of leisure and allowed me to live life to the full outside of work.

Acknowledgements

In this section, I would like to thank all the people in academia and at Ansaldo Energia who made this PhD programme and the completion of this thesis possible.
First of all, I would like to thank Prof. Stefano Zucca, who gave me the opportunity to obtain this scholarship and collaborate with a company like Ansaldo Energia, which focuses on young people and is always open to innovation.
I would like to thank my academic supervisors, Prof. Teresa Berruti and Prof. Daniele Botto, who have supported my work throughout the programme, working with me to find solutions to the problems we encountered.
I would also like to thank my company supervisors, Andrea Bessone and Francesco Bagnera, who welcomed me and made me feel at home as soon as I arrived at Ansaldo. They gave me constant technical support and contributed significantly to the completion of this thesis.
Finally, I would like to thank my fellow PhD students in the AERMEC group, with whom I have been able to exchange work ideas, enjoy moments of leisure and take many coffee breaks.

Abstract

Sustainable electricity production has always been a very complex engineering challenge, as the amount of energy required daily by human activities is extremely high. Nowadays, most electricity is produced using steam and gas turbines, or combined cycle turbines. New-generation turbines can achieve very high efficiency, but the problem of CO_2 emissions remains a difficult challenge to overcome, as their operation is still linked to the use of fossil fuels. The energy market is evolving very quickly, and there is a growing trend towards electricity production from renewable sources. In particular, the possibility of producing electricity through nuclear fusion is becoming a reality. In fact, many companies, including Ansaldo Energia, have joined the ITER (International Thermal Experimental Reactor) program, which involves the construction of a working demonstration nuclear fusion reactor. The steam turbine that will be powered by this reactor is designed and manufactured by Ansaldo Energia. The last stage turbine blades are subjected to high stresses during turbine operation, which are caused by forced vibrations induced by the fluid-blade interaction. The vibration amplitudes may reach critical values, causing HCF (High Cycle fatigue) problems and the blades catastrophic failure. To avoid structural failure, dry friction devices are used to mitigate vibrations, dissipating a portion of the kinetic energy of the system. The dry friction devices commonly used for turbomachinery applications are shrouds, snubbers and underplatform dampers. These devices base their operation on the relative motion, caused by vibration, involving the contact surfaces between two adjacent blades. The relative motion between two surfaces in contact generates frictional forces, which cause the dynamic response of the system to be non-linear, as they depend on the relative displacements. This leads to the necessity to adopt a non-linear tool to predict the blades forced response considering the frictional forces effect.

The AERMEC research group at the Polytechnic University of Turin has developed a tool for Ansaldo Energia for the non-linear forced response computation of turbine

blades with friction contacts. For convenience of notation, this tool will simply be referred to as the Ansaldo's non-linear tool in this doctoral thesis.
the Ansaldo's non-linear tool is capable to compute the non-linear displacements field of the reduced blade model, taking as input the reduced stiffness and mass matrices, but is not able to compute the non-linear dynamic stresses because the reduced model does not include the FEM model elements. This represent a critical drawback in the mechanical design cycle because to predict the blade fatigue life is mandatory to compute the dynamic stresses amplitude.
Ansaldo Energia is one of the partners in the ITER (International Thermal Experimental Reactor) program, a European project that aims to build a demonstration power plant (DEMO), capable of powering the Ansaldo steam turbine and thus producing electricity without CO_2 emissions. The structural integrity of the nuclear reactor is guaranteed by the toroid, that has the crucial function on confining the high temperature plasma with a powerful magnetic field. The toroid has to handle very high currents for generating the magnetic field, this leads to its overheating.
At the current state of the art,to avoid this, the nuclear fusion reactor must be shut down and restarted periodically, causing the turbine to operate in transient conditions where the steam flow rate is extremely low. Very low steam flow rates can power the first stages, but the last stage is dragged by the previous ones and operates in compressor mode, dragging the residual steam in the chamber. These particular conditions are known as ventilation conditions, which cause asynchronous excitation, rotating stall cells and an increase in blade temperature. Under these conditions, the blades of the last stage can vibrate with very high amplitudes, which is why it is important to use mechanical devices to reduce these amplitudes and to have a robust procedure in place to predict the stresses on the blade, taking into account the effect of friction contacts.
This doctoral thesis deals with the development of a robust procedure for computing the dynamic stresses in turbine blades taking into account the friction contacts behavior during forced vibrations. This procedure will be applied on the last stage blades of the steam turbine designed by Ansaldo Energia, that will be powered by the nuclear fusion plant. The procedure developed during this doctoral program has the ultimate goal of calculating dynamic stresses, but to achieve this, it was necessary to perform some intermediate steps. The first problem addressed during this PhD concerns the generation of reduced mass and stiffness matrices. It is important to generate a reduced model that takes into account both the effect of centrifugal force

and the effect of static contact forces but does not include ANSYS contact elements. This was achieved by performing a preliminary static analysis with contact elements on the contacting surfaces, extracting the contact forces into a local reference system that is consistent with the blade deformation, and finally performing a second static analysis without the contact elements but importing the contact forces calculated in the preliminary analysis as external forces. The second problem encountered was the generation of a preload matrix on the contact nodes that takes into account the large deformation of the blade, thus avoiding the Ansaldo's non-linear tool convergence problems. The solution to this problem is found in the previous step, where the static contact forces, which constitute the pre-loads, are extracted into a local reference system that is defined on the deformed geometry.
The last problem addressed in this doctoral thesis is the calculation of stresses on the blade, taking into account the behavior of friction contacts during vibrations. As mentioned above, it is not possible to calculate the stress state in the Ansaldo's non-linear tool, so to overcome this problem, the friction forces calculated with the Ansaldo's non-linear tool in the frequency range defined for the non-linear calculation were extracted, and a linear harmonic analysis was then performed in ANSYS on the full FEM model, importing the friction forces as external harmonic excitations. This step allows the stress state on the blade to be calculated taking into account the friction forces. A check that was performed before the stress calculation was a comparison between the non-linear frequency response curve calculated with the Ansaldo's non-linear tool and that calculated with ANSYS, in order to ensure a correspondence of the non-linear displacements and, consequently, a correct evaluation of the stress state.
The nuclear fusion reactor is currently under construction, so the aerodynamic excitations under ventilation conditions are not known, but the procedure described so far constitute a robust a mechanical design tool for turbine blades that can be used in the future to evaluate the dynamic stresses on the blade with realistic aerodynamic excitation values.

Contents

List of Figures

List of tables

Symbols and Abbreviations

This section lists all the main symbols and abbreviations used in this doctoral dissertation.
The main used symbols are listed below:

Symbols

$\boldsymbol{\Omega}$	Turbine rotation speed
$\boldsymbol{K}$	Stifness of the system
$\boldsymbol{C}$	Linear damping of the system
$\boldsymbol{M}$	Total mass of the system
$\boldsymbol{X}(\boldsymbol{t})$	Displacement of the system in time domain
$\boldsymbol{F}(\boldsymbol{t})$	External forcing term in time domain
$\boldsymbol{N}_0$	Normal pre-load acting on the contact element
$\boldsymbol{T}(\boldsymbol{t})$	Tangential friction force in time domain
$\boldsymbol{N}(\boldsymbol{t})$	Normal force in time domain
$\boldsymbol{\mu}$	Friction coefficient
$\boldsymbol{w}$	Displacement of the contact element
$\boldsymbol{\omega}$	Pulsation
$\boldsymbol{k}_t$	Tangential stiffness of the contact element
$\boldsymbol{k}_n$	Normal stiffness of the contact element
$\bar{\boldsymbol{X}}$	Displacement of the system in frequency domain
$\bar{\boldsymbol{F}}$	External forcing term in frequency domain
$\left\{\bar{\boldsymbol{F}}\right\}$	External forcing vector in frequency domain
$\left\{\bar{\boldsymbol{\Theta}}\right\}$	Complex mode shapes vector
$\bar{\boldsymbol{T}}$	Tangential friction force in frequency domain

$\bar{\boldsymbol{D}}$	Dynamic stiffness of the system
$\boldsymbol{Z}$	Tangent vector
$\boldsymbol{h}$	harmonic index
$\boldsymbol{\alpha}$	Ground inclination
$\boldsymbol{gap}$	Initial distance between the mass and the ground
$\boldsymbol{R}$	Residual term
$[\boldsymbol{K}]_{CB}$	Stiffness matrix of the reduced order model
$[\boldsymbol{M}]_{CB}$	Mass matrix of the reduced order model
$[\boldsymbol{M}]$	Mass matrix
$[\boldsymbol{K}]$	Stiffness matrix
$[\boldsymbol{\Phi}]$	Mode shapes matrix
$\boldsymbol{\zeta}$	Damping ratio
$\boldsymbol{f}$	Frequency
$\boldsymbol{\Delta}$	Tolerance on turbine rotation speed
$\boldsymbol{eo}$	Engine order
$\boldsymbol{N}_{SC}$	Number of rotating stall cells
$\left\{\boldsymbol{U}\right\}$	Displacements vector of the reduced order model
$\left\{\boldsymbol{X}\right\}$	Displacements vector of the two degrees of freedom model of the fundamental sector
$\left\{\boldsymbol{F}\right\}_{nl}$	Friction forces vector
$\left[\boldsymbol{D}\right]$	Dynamic stiffness matrix
$\left\{\boldsymbol{R}\right\}$	Residual vector
$\left[\boldsymbol{J}\right]$	Jacobian matrix
$\boldsymbol{\varphi}$	Interphase Blade Angle
$\boldsymbol{N}_{teta}$	Number of points for discretizing the time signal within the contact model

The main used abbreviations are listed below:

Abbreviations

FEM	Finite Element Model
MHBM	Multi Harmonic Balance Method

IFFT	Inverse Fast Fourier Transform
FFT	Fast Fourier Transform
AFT	Alternating Frequency Time
DOF	Degree of Freedom
DOFs	Degrees of Freedom
HCF	High Cycle Fatigue
ULS	Underlying Linear System
IPBA	Interphase Blade Angle
PS	Pressure side
SS	Suction side
ITER	International Thermal Experimental Reactor

Chapter 1

Introduction

1.1 Steam turbines

The production of electricity while minimizing CO_2 emissions is a very challenging engineering task that is still ongoing. Currently, most electricity is produced using gas, steam, or combined cycle turbines. In the latest generation of turbines, efficiency has reached very high levels, but energy production remains tied to the use of fossil fuels. However, the energy market is constantly evolving, and electricity production from renewable sources is becoming increasingly feasible. In particular, nuclear fusion could be the only solution to meet the energy demands of human activities while reducing emissions to virtually zero. This technology is currently still in the design and development phase, but a European project is underway with the aim of building a working demonstration nuclear fusion reactor. Many European companies have joined this project, including Ansaldo Energia. The use of this technology in the future would shift the center of gravity of the electricity production market towards steam turbines. Steam turbines operate using high-enthalpy steam that expands through different stages.
Figure 1 shows the low-pressure section of a steam turbine with the different stages:

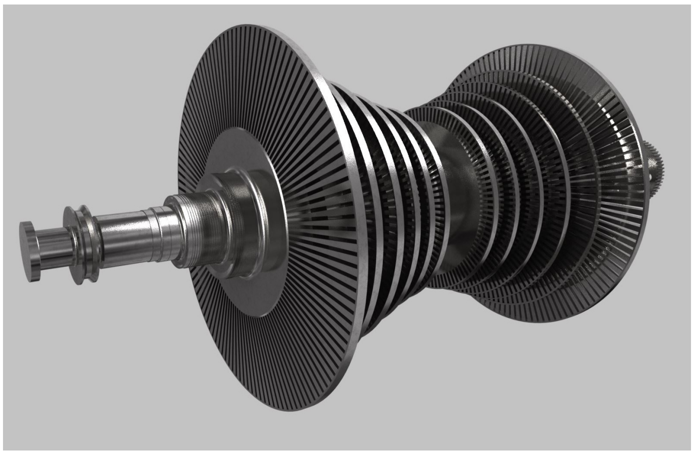

Figure 1: Low pressure section of a Steam turbine generator
(https://grabcad.com/library/steam-turbine-runner-1)

The low-pressure section shown in Figure 1 represents a double-flow turbine configuration, in which the steam expands in both directions, axially.
This configuration allows the axial thrust due to the variation in the momentum of the fluid in the axial direction to be self-balanced.
What can be observed in Figure 1 is that the blades of the last stage are much longer than those of the previous stages. The blades of the last stage are designed in this way to make the most of the enthalpy jump of the steam, which is greatly reduced when it reaches the last stage.
Since the blades of the last stage are very long, they are the most critical part of the turbine because they are subjected to high static and dynamic stresses. The blades of the last stage are much larger than those of the previous stages, which leads to greater static stresses due to centrifugal force and also to greater dynamic stresses due to forced vibrations induced by aeroelastic phenomena such as flutter [1–3].

1.1.1 Last stage turbine blades vibrations

The forced vibrations to which the blades of the last stage are subjected, if not adequately damped, cause large deformations, which lead to high dynamic stresses that cause HCF problems [4, 5]. HCF (High Cycle Fatigue) can lead to the initiation and propagation of cracks after a high number of cycles, resulting in catastrophic blade failure [6]. Blade breakage is a very serious problem as the part of the component that detaches impacts against the other rotating blades, this leads to catastrophic stage failure resulting in the need to stop the turbine. These problems can be avoided by designing the system so that the natural frequencies are different from the synchronous exciting frequencies, which are multiples of the turbine's rotational speed. This can be achieved by changing the number of blades, changing the mass distribution or using coupling devices between adjacent blades to increase the natural frequencies of the system. This is not always sufficient to completely avoid vibration phenomena since the frequency range of aerodynamic forces is widespread. Consequently, it is important to provide devices at the design stage that are capable of reducing vibration amplitudes by dissipating some of the kinetic energy of the system. For this purpose dry friction devices are widely used in the field of turbomachinery, they will be described in detail in the next subsection. Steam turbines do not usually suffer from fluid temperature issues, as the steam does not reach temperatures that can damage the blades if the machine operates under design conditions, which provide for a continuous steam flow. In the future, where steam turbines may be powered by steam produced by nuclear fusion power plants, the steam flow rate will not be continuous, as the machine needs to be switched off and on again periodically for plant-related needs. This situation causes transients, in which the turbine operates with very small steam flow rates. Low flow rates lead to rotating instabilities [7–14] and flow separation [15], that can cause asynchronous excitations and vortices. Under these conditions, known as ventilation conditions, the last stage operates in compressor mode, resulting in a temperature increase on the blades due to friction between the blades themselves and the residual fluid in the chamber [16–18]. This increase in temperature modifies the natural frequencies of the system, how can be seen in [19], leading to possible resonances, so it is mandatory, as mentioned before, to provide at the design stage devices capable of reducing vibration amplitudes.

1.1.2 Dry friction devices for forced vibrations damping

Dry friction devices [20–22], as mentioned in previous subsection, are designed to reduce the forced vibrations amplitude during resonance phenomena. Their operation is based on the relative motion of contact surfaces placed between two adjacent blades. There are different kinds of dry friction devices, the most used for turbomachinery application are the following:

- Underplatform damper: it is a dry fricion device placed underp-latform between two adjacent blades.
- shroud: this device couples the blades on the tip [23–26].
- snubber [27].

These devices have a dual function, they are used both to reduce vibration amplitudes and to couple adjacent blades in order to stiffen the system and increase its natural frequencies. Examples of the friction devices just mentioned are shown in Figure 2:

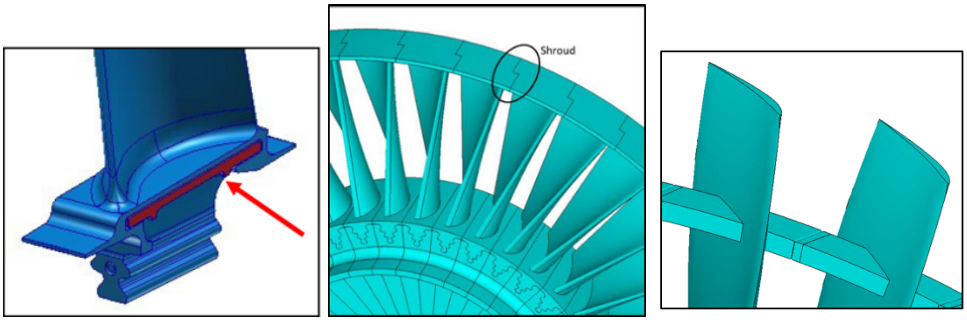

(a) Underplatform damper (b) Shroud (c) Snubber

Figure 2: Dry friction devices for turbomachinery applications

These devices are usually designed so that the blades only make contact when the turbine is rotating, otherwise the blades are free standing. In Figure 2 it can be seen that in the undeformed geometry there is an initial gap between the contact surfaces, this is very evident in the case of the snubber. When the turbine starts to rotate, the blades deform due to the centrifugal force, until the speed of 3000 rpm is reached. At this angular speed, the contact surfaces are coupled with a certain preload, which depends on the design of the device and the deformation of the blades. During forced vibrations, the amplitudes of the dynamic displacements can reach values such that the tangential forces exceed the Coulomb limit, defined as $|\mu N|$, where μ is the coefficient of friction and N is the preload normal to the contact surfaces. When the Coulomb limit is exceeded, the contact surfaces begin to slip and this causes there to be relative motion between them. This mechanism generates friction forces that dissipate some of the kinetic energy of the system, thus reducing vibration amplitudes and limiting HCF (High Cycle Fatigue) problems.

1.2 Research goals

The previous subsection explained in detail how mechanical damping devices work. Their effectiveness is based on the relative motion between two surfaces in contact, which leads to the generation of friction forces that dissipate part of the kinetic energy, thus reducing the vibration amplitudes of the blades. Friction forces are non-conservative forces dependent on relative displacement, which means that the dynamic behavior of the blades in the presence of friction contacts cannot be characterized by a linear dynamic model.
In order to study the forced response of turbine blades in the presence of friction contacts, it is necessary to use specific tools that take into account the dependence of friction forces on relative displacement. For this purpose, The AERMEC research group at the Polytechnic University of Turin has developed a tool for Ansaldo Energia for the non-linear forced response computation of turbine blades with friction contacts. The Ansaldo's non-linear tool was developed in Matlab and takes as input the mass and stiffness matrices of the reduced FEM model, in which only a few physical degrees of freedom, called master nodes, and a certain number of modal degrees of freedom are condensed. Using reduced matrices to calculate the non-linear forced response drastically reduces calculation times, but it is a major limitation for calculating stresses, the evaluation of which is fundamental in the mechanical design cycle of the blades.
What has been said so far introduces the goal of this research, the development of a robust and repeatable procedure capable of calculating the stress state on turbine blades, taking into account the presence of friction contacts.
This goal was achieved by following several steps, which will be explained in detail in the relevant chapters.
The procedure developed has been applied to the last stage blades of the steam turbine manufactured by Ansaldo Energia, which will in future be powered by the DEMO nuclear fusion demonstration reactor.
When the turbine will be powered by steam produced by the nuclear fusion plant, the operating conditions will no longer be those of the design, in which the steam flow is continuous, but will vary according to the needs of the plant.
In particular, to prevent overheating of the toroid, which has the fundamental function of isolating the plasma and thus ensuring the integrity of the plant, the reactor will have to undergo periodic shutdowns and restarts. Under these conditions, the

steam flow rate is no longer constant, leading to transients in which the turbine must operate with very low steam flow rates.
Small steam flow rates are sufficient to power the first stages, while the last stage is driven by the previous stages and operates in compressor mode. These particular conditions are known as ventilation conditions, and cause asynchronous excitation, rotating stall cells and an increase in blade temperature, causing the blades to operate outside their design conditions, with possible unexpected resonances and thus a drastic reduction in component life.
To avoid catastrophic failures, it is therefore essential to use devices capable of mitigating vibrations. At the same time, however, it is necessary to have a robust tool that is capable of predicting the dynamic behavior of the system, taking into account the non-linearity caused by friction contacts.
Figure 3 shows a scheme of the mechanical integrity design cycle:

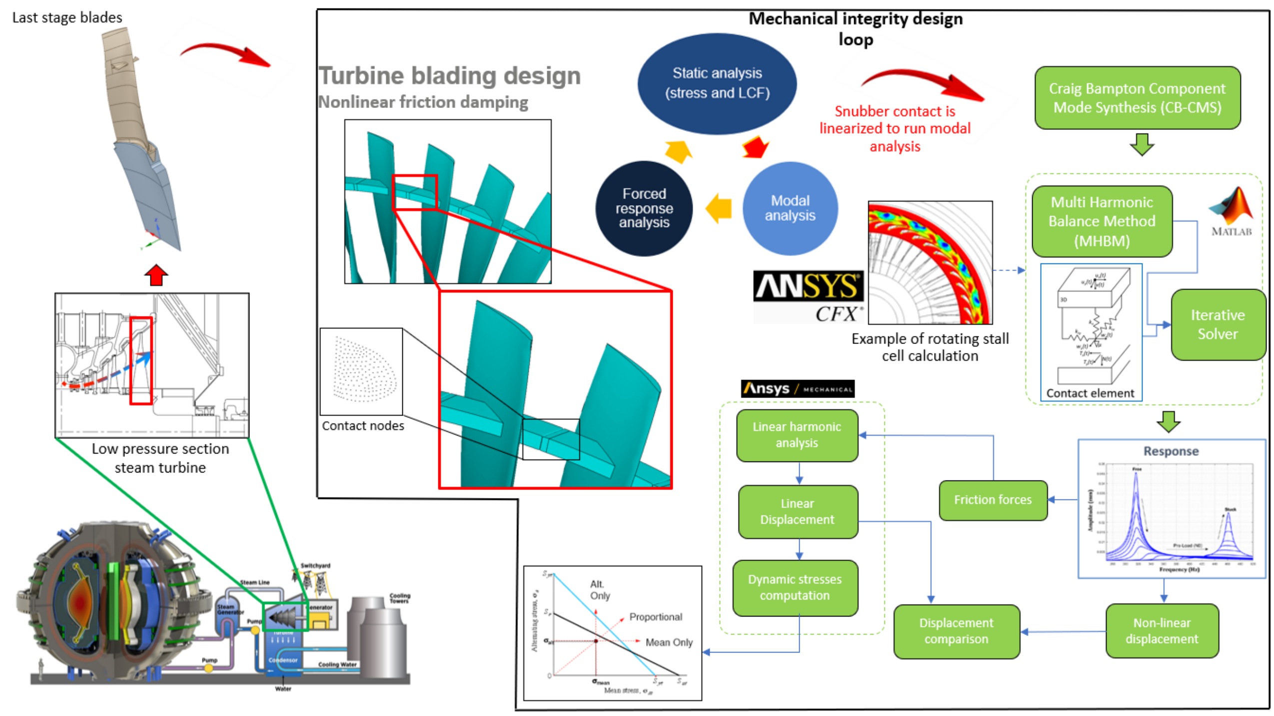

Figure 3: Mechanical integrity design cycle

The diagram shown in Figure 3 highlights the importance of being able to accurately predict dynamic stresses in the mechanical design cycle of blades, especially if this phase requires the evaluation of conditions never experienced by the turbine. The procedure developed in this thesis is a robust and reliable tool designed for

this purpose, which Ansaldo Energia can implement within the mechanical integrity cycle, thereby optimizing the prediction of component fatigue life.
The next chapter will provide an overview of the thesis, first explaining the approach adopted to achieve the objectives of the PhD, and then summarizing the contents of the various chapters to clarify the structure of this thesis to the reader. Before this, however, it is important to explore the work carried out in the literature on the topics mentioned so far.

1.3 Literature overview

As mentioned above, this section aims to explore the work carried out in the literature on three main topics:

- The efficient generation of reduced models.
- The calculation of the forced response of bladed disks in the presence of friction contacts.
- The calculation of dynamic stresses on bladed disks due to vibration phenomena.

The calculation of non-linear forced response requires the use of specific tools, as the presence of friction forces introduces non-linearity into the equations of motion of the system. Until recently, commercial finite element software, such as ANSYS, did not allow forced response calculations to be performed taking friction contacts into account. New features have now been introduced that allow non-linear calculations to be performed. However, it is still more advantageous to use specific tools, as the calculation times are significantly shorter.
These non-linear tools are usually developed in programming environments, such as Matlab, which cannot handle models as large as FEM models with a very high number of nodes. For this reason, it is necessary to use reduced-order models, within which a certain number of physical and modal degrees of freedom of the full model are condensed. In addition, the reduced models must take into account the effect of the various static forces acting on the system, such as centrifugal force and contact forces.

The following subsection reports the state of the art regarding the topics discussed in this introductory part, divided into two parts:

- The first part presents papers related to the generation of reduced models and the calculation of non-linear forced response in the presence of friction contacts.
- The second part discusses papers related to the calculation of dynamic stresses.

1.3.1 Overview

Sommariva et. al [28] compares two different Craig-Bampton reduction strategies, which are applied to different test cases, on which cyclic symmetry conditions must also be imposed. What comes out of this work is that both strategies provide very good accuracy, so they can be used to generate reduced-order models, which are the main input for a non-linear solver.

Tamatam et. al [29] addresses the problem of evaluating the effect of wear due to the relative motion of the contacting surfaces during blade vibrations. In order to evaluate the effect of wear, a computational scheme is proposed in this paper that couples a model for calculating the non-linear forced response with a model for calculating the wear depth. One of the model inputs for calculating wear depth is the energy dissipated by friction during an hysteresis cycle, which is calculated using the first model previously mentioned. The calculation of the non-linear forced response requires the use of a reduced-order model, which was obtained in this work by the use of the Craig-Bampton reduction method. The calculation scheme proposed in this paper was successfully applied to a cantilever beam and a shrouded blade.

Pourkiaee et. al [30] proposed an efficient method for generating reduced-order models for calculating the non-linear forced response of bladed disks. In this paper, the Craig-Bampton reduction method is applied to a bladed disk with shrouded blades to generate a reduced-order model in which the degrees of freedom are expressed in terms of relative coordinates. This allow to reduce the computational effort and to include the full-stick modes of the fundamental sector.

Mashayekhy et. al [31] proposed an efficient reduction technique that can be applied to mistuned bladed disks. The proposed method is defined as an hybrid technique because involve two reduction strategies: the Component Mode Mistuning

(CMM) and the dual model order reduction. This hybrid method was applied in this paper to a simplified bladed disk model with shrouded blades. The obtained results show a good accuracy of the proposed method.

Quaegbeur et. al [32] discuss about a reduction technique that can be applied to cyclic symmetry models subjected to prestress loads, such as centrifugal loads, and strong non linearities such as friction and separation. The proposed method is applied in this paper to different test cases, showing an optimal accuracy.

Drowzdoski et. al [33] deals with the calculation of the non linear forced response of a steam turbine last stage blades. The analyzed last stage blades are coupled by friction bolt damping elements. The non linear forced response is carried out with DATES, that is a numerical code. DATES couples the contact nodes with 3D contact elements, capable of calculating the tangential contact forces on the contact surface for each couple of contact nodes. The results obtained with numerical simulations are compared with experimental data, showing a good accuracy of the numerical code.

Siewert et. al [34], similar to what was done by [33], performed a numerical calculation of the non linear forced response of a steam turbine last stage blades. The numerical results are compared with experimental data deriving from spin-pit tests. The comparison shows a good robustness of the numerical calculation.

Ferhatoglu et. al [35] deals with the non linear forced response of bladed disks with mid-span dampers. The non linear forced response is computed with a reduced order model, obtained from the full FEM model. Different values of static preloads and external excitations are explored. The calculation performed in this paper consider a coupled approach of static and dynamic equations, The obtained results show a good damping performance of mid-span dampers, that significantly reduce vibration amplitudes. Another interesting result of this paper is the variability of the non linear response due to the non uniqueness of the friction forces.

Finally, Zucca et. al [36] performed the non linear forced response of a steam turbine last stage shrouded blades. The calculation is carried out with a numerical code, following three main steps:

- Static calculation carried out on the full FEM model. This preliminary calculation provide the static contact forces, that are an input for the numerical code.

- Reduction of the full FEM model, taking into account the effect of the centrifugal force.
- Import of the reduced order model into the numerical code for the forced response calculation

In this paper the calculation was carried out considering the first bending mode shape and the first torsional mode shape. The obtained results are compared with experimental data, showing a good accuracy of the numerical code.
This paper concludes the first part of this literature overview. The second part will be dedicated to the papers that discuss the computation of dynamic stresses on bladed disks.

Vyas et. al [37] developed an analytical code capable of computing dynamic stresses and predicting the fatigue life of turbine blades. The life prediction algorithm is based on a combination method, which combines the local strain approach to predict the initiation life and fracture mechanics approach to predict the propagation life. The modeling is done for a general tapered, twisted and asymmetric cross section blade mounted on a rotating disc at a stagger angle.
Critical cases of resonant conditions of blade operation are considered.
The main result of this paper is to have an analysis package that include both dynamic stresses and fatigue life prediction. The analytical model is an approximation of the real problem , so the results are not the exact solution of the problem, but still remain an improvement of the conventional stress-based approach for life estimation.

In this paper, Tie et. al [38] perform a calculation of the dynamic stresses on the blades of a steam turbine by coupling a finite element solver, in this case ABAQUS, with an in-house CFD solver. The analysis was performed on free-standing blades, taking into account both material damping and mechanical damping due to contact between the blades and the disk at the blade root. The mechanical damping at the blade root was calculated using a very simple two-degree-of-freedom model, in which the masses and stiffnesses were tuned so that the natural frequencies of the concentrated-parameter model matched those of the full FEM model. The two-degree-of-freedom model used to calculate mechanical damping was verified by performing an explicit, time-domain calculation on the FEM model. A comparison between the results obtained from the two-degree-of-freedom model and those from the FEM model shows a good match. In fact, the amplitudes calculated on the lumped parameters model are comparable to those calculated on the FEM model, albeit with a certain frequency shift.

The last paper analyzed in this section is the work done by Battiato et. al [39], which presents a workflow for calculating dynamic stresses on turbine blades in the presence of frictional contact. The workflow presented in the paper is structured as follows:

- The first step is the reduction of the FEM model, from which the reduced mass and stiffness matrices are obtained.
- The second step involves defining the contact parameters and calculating the non-linear forced response of the reduced model.
- The third step involves expanding the non-linear displacements to all master nodes of the reduced model.
- The next step involves applying the non-linear displacements to the master nodes of the superelement and then performing a harmonic analysis on it at the resonance frequency. This step allows the non-linear displacements to be transferred to the master nodes of the superelement.
- Next, the real and imaginary parts of the solution are expanded separately to all nodes of the FEM model.
- Using the displacements from the previous step as input, two static analyses are performed to calculate the real and imaginary parts of the dynamic stresses.

The stress recovery algorithm described here was applied to a bladed disk for various non-linear forced responses, calculated using different values of normal preload n_0. The results obtained by Battiato et al. highlight two main aspects. The first aspect concerns the need for an algorithm to calculate dynamic stresses on turbine blades. In fact, in the technical literature, the non-linear forced response is usually evaluated solely in terms of the maximum amplitude of the structure measured at specific points. Although this allows for the determination and quantification of the structure's non-linear behavior, it constitutes a major limitation for blade design, which requires the calculation of stresses in order to subsequently determine the

blades' fatigue life. The second aspect highlighted concerns the importance of having an algorithm capable of calculating dynamic stresses while taking into account the effect of friction damping. In fact, as shown in the paper, when the algorithm is applied to cases close to the linear case, the stress distribution does not change significantly compared to the full-stick case. The situation is, however, very different when the algorithm is applied to a highly non-linear case. In this situation, the stress distribution is markedly different from that of the full-stick case.
This demonstrates that friction damping influences the stress distribution and, consequently, the location of the most critical areas; for this reason, it is important to be able to calculate stresses without neglecting this effect.

The three issues addressed in the aforementioned papers are closely related. In fact, for an accurate calculation of dynamic stresses, it is necessary to correctly calculate the non-linear forced response, which requires the generation of an appropriate reduced model.
As can be seen from the literature, various reduction methods have been successfully applied to bladed disks, obtaining reduced-order models that have been used to calculate the non-linear forced response. The results obtained showed an excellent match with the experimental data, highlighting that the reduced models used are able to correctly approximate the dynamic behavior of the full FEM model.
As regards the calculation of dynamic stresses, several codes, both analytical and numerical, have been developed for this purpose. The results obtained show good stability and robustness of the codes used. What can be concluded from the work done in the literature can be summarized as follows:

- The accuracy of reduced models has been significantly improved, allowing for more realistic simulation of the dynamic behavior of the system.

- Improvements in reduction techniques have made it possible to calculate the non-linear forced response of bladed disks more accurately.

- Algorithms for computing the dynamic stresses due to vibrations, taking friction forces into account, have been developed.

Chapter 2

Thesis overview

2.1 Novel approach

The purpose of this chapter is to discuss in detail the workflow developed during my doctoral research, and to highlight the main differences from the work reported in the literature. As mentioned earlier, the ultimate goal of my research is to develop a stress recovery procedure for calculating dynamic stresses on turbine blades in the presence of frictional damping. The preliminary steps for calculating dynamic stresses are:

- Model reduction.
- Calculation of the non-linear forced response.

The typical workflow described in the literature for calculating the non-linear forced response of reduced-order models is structured as follows:

- The first step is the reduction of the FEM model, performed by removing contact elements. Contact elements are removed to avoid overestimating the stiffness matrix of the reduced model.
- The second step is the calculation of static preloads, which are necessary for the calculation of the non-linear forced response. The static preloads are calculated using a preliminary static analysis performed on the FEM model.

- The third step is the actual calculation of the non-linear forced response, which is performed using in-house software that takes the reduced matrices and static preloads as inputs.

The workflow proposed for the preliminary steps in this doctoral dissertation differs from the work reported in the literature in two main aspects:

- The FEM model was reduced by removing the contact elements from ANSYS, while at the same time taking into account the effect of static contact forces.
- The static preloads were calculated using a preliminary static analysis, defining a local reference system on the contact surfaces that is consistent with the deformation of the blades.

This workflow offers several advantages over the one proposed in the literature. First, generating a reduced-order model that accounts for the effect of static contact forces ensures greater accuracy in the calculation of the non-linear forced response and, consequently, of the dynamic stresses.
Second, calculating the static preloads in a reference system consistent with the deformation of the blades allows the displacement of the contact surfaces to be accounted for, thereby avoiding convergence issues with the tool used to calculate the non-linear forced response.
This aspect has been neglected in the literature workflow, but this remains a valid approximation only for small deformations. The blades of the last stage of the Ansaldo steam turbine, however, undergo significant deformation before the snubber surfaces come into contact; consequently, this aspect cannot be neglected.
The generation of a reduced model that takes into account both centrifugal force and static contact forces was made possible by performing two static analyses. The first static analysis was performed by inserting the contact elements on the snubber, with the aim of calculating the static contact forces. This step is essential for two main reasons:

- It allows the static contact forces to be obtained, which are necessary for the second static analysis.
- It allows the input file of static preloads to be obtained in a reference system integral with the deformed geometry.

The second static analysis is performed by removing the contact elements on the snubber. This is crucial, as importing the ANSYS contact elements into the reduced model could lead to an incorrect calculation of the natural frequencies of the system and, consequently, to an inaccurate calculation of the non-linear forced response.
To avoid neglecting the effect that the snubber has on blade deformation, the static contact forces calculated with the previous static analysis are imported as external forces.
This allows the effect of contact closure to be simulated without the contact elements being physically defined.
Once the second static analysis had been performed, the model was reduced using the Craig-Bampton algorithm implemented in ANSYS. At this point, the matrices of the reduced model obtained take into account both the effect of centrifugal force and the effect of static contact forces.
As discussed earlier, the ultimate goal of my research is to develop a stress recovery procedure for steam turbine blades with frictional contacts.
The reference paper on the work carried out in this field is that of Battiato et al. [39]. The previous chapter described in detail the workflow used by the authors to calculate dynamic stresses. The preliminary steps are always the reduction of the FEM model and the calculation of the non-linear forced response.
For stress recovery, the following steps are performed:

- Expansion of the non-linear displacements calculated on the reduced model to the master nodes of the superelement. This step involves performing a linear harmonic analysis on the superelement by applying the non-linear displacements derived from the forced response calculation.
- Expansion of the non-linear displacements to the entire FEM model.
- Two static analyses, in which the inputs are the non-linear displacements calculated in the previous step, are performed.
- Stress recovery.

The approach I used during my research differs from the work reported in the literature. The workflow I developed during my doctoral studies is structured as follows:

- FEM model reduction.

- Non-linear forced response computation.
- Extraction of non-linear friction forces.
- Application of the non-linear forces extracted in the previous step to the same contact nodes that were condensed in the reduced model.
- Linear harmonic analysis in ANSYS.
- Stress recovery.

The key difference between the workflow used in the literature and the one presented here lies in the use of the non-linear forced response outputs for stress recovery. In the literature, stress recovery was performed using one linear harmonic analysis and two static analyses. This entails a fairly high computational cost, considering that FEM models of real blades can have over 2 million nodes. An advantage of the workflow proposed in the literature is that it is not necessary to define the damping matrix for stress recovery, since this effect is already included in the non-linear displacements.

The workflow proposed in this research allows dynamic stresses to be calculated directly by performing a linear harmonic analysis, since the friction forces provided as input to the FEM model were calculated using a non-linear forced response analysis and therefore inherently include the effect of friction damping. This makes it possible to limit the number of analyses performed on the FEM model, thereby reducing computation time.

One drawback of the developed workflow is the presence of fictitious stress peaks at the points where forces are applied. However, this issue is negligible for evaluating the stress distribution across the entire blade.

The workflow developed in this thesis is a robust and reliable tool for calculating the dynamic stresses of turbine blades in the presence of friction contacts, and although it was developed for a specific application, it can be applied to any type of blade.

The steps of the procedure have been described in a generic manner at this level, with the aim of helping the reader understand what has been done and with what objective. In the dedicated chapters, each individual step of the procedure will be explained in detail, step by step.

The next section will provide an overview of the thesis, summarizing the content of each chapter.

2.2 Overview

This section provides a general description of all the topics covered in the various chapters of this thesis. This makes it easier for the reader to understand this work and the logical order chosen for the different chapters.

Chapter 1: The introductory part of Chapter 1 provides a general overview of steam turbines and the vibration problems associated with the final stages. It then discusses the mechanical friction devices most commonly used in turbomachinery for vibration damping, and the problems they introduce in solving the equations of motion of the system. This links to the objective of this doctoral thesis, which is discussed in the last part of this chapter. The final part of Chapter 1 is devoted to an overview of the work carried out in the literature on the calculation of non-linear forced response and dynamic stresses on turbine blades.

Chapter 2: Chapter 2 is divided into two parts. The first part is devoted to explaining the approach adopted in this thesis to achieve the objectives of the PhD, highlighting the differences with the work present in the literature. The second part is devoted to an overview of the topics covered in the thesis.

Chapter 3: Chapter 3 provides a detailed explanation of all the numerical methods used in this thesis to solve the non-linear equations of motion of the reduced blade model. All the numerical methods described in this chapter are implemented in the Ansaldo's non-linear tool, the tool for calculating the non-linear forced response of turbine blades developed by the Aermec group at the Polytechnic University of Turin for Ansaldo Energia.

Chapter 4: Chapter 4 in the first part briefly explains the input and output of Ansaldo's non-linear tool, and why it is important to generate an efficient reduced-order model that is capable of taking into account all the effects that influence the reduced matrices. The second part of the chapter is devoted to a detailed description of all the steps necessary for generating the reduced model.

Chapter 5: Chapter 5 is dedicated to a detailed description of all the steps involved in the procedure for calculating dynamic stresses in the presence of friction contacts. To clarify each individual step, the procedure has been applied to a case study and the results obtained are shown at the end of the chapter.

Chapter 6: Chapter 6 considers a case study in which the last stage blades of the steam turbine discussed in this thesis vibrate due to a resonance condition caused by ventilation conditions. The procedure explained in Chapter 6 was applied to calculate the dynamic stresses due to vibrations. This chapter demonstrates the effectiveness of the procedure developed in this thesis, highlighting the importance of having a robust and reliable tool for this purpose.

Chapter 7: Chapter 7 concludes this doctoral thesis and aims to summarize the work carried out, highlighting the robustness and reliability of the procedure developed during these three years of doctoral study. The final part of the chapter focuses on future work, discussing possible improvements to the procedure developed and the methods used.

Chapter 3

Solution methods

The purpose of this chapter is to provide a detailed description of the mathematical solution methods used in this dissertation to solve the equation of motion of the bladed disk being studied during this doctorate. These methods become necessary when frictional forces on the contacting surfaces are taken into account, since they depend on the displacements of the system. This leads to the need to solve the equation of motion iteratively. The two solution methods that will be discussed in this chapter are listed below:

1. MHBM (Multi Harmonic Balance Method)

2. MHBM coupled with pseudo arc length continuation

The MHBM is a numerical method, widely used in literature [40], for calculating with accuracy and efficiency the non-linear steady-state dynamic response of mechanical systems.
The MHBM coupled with the pseudo arc length continuation is the same numerical method, but an additional constraint is added on the residual. This aspect will be widely discussed in next subsections.

3.1 MHBM (Multi Harmonic Balance Method)

The MHBM, as mentioned earlier, is a numerical method used for steady-state non-linear response response of mechanical systems. For simplicity of notation, in this section this method will be explained taking as example a 1 DOF system connected to the ground with a contact element. All that will be shown for the 1 GDL system is replicable on systems with many DOFs and real bladed disks FEM models. Let's now consider the 1 GDL system shown in Figure 4:

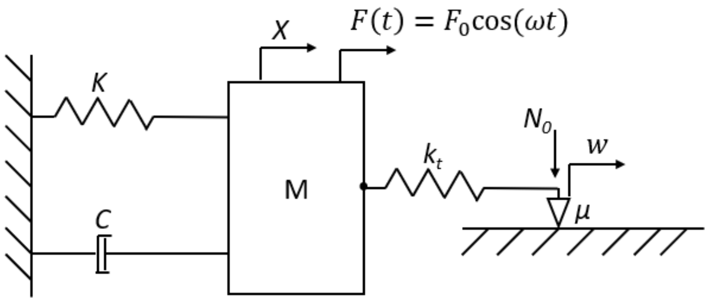

Figure 4: 1 GDL system with Jenkins contact element

in which:

- K is the stiffness of the system.
- C is the linear damping of the system.
- X is the displacement of the system
- $F(t)$ is the external forcing term
- k_t is the tangential stiffness of the Jenkins contact element
- N_0 is the normal pre-load acting on the contact element
- μ is the friction coefficient
- w is the displacement of the contact element
- M is the total mass of the system

The forces acting on the mass M are shown in Figure 5:

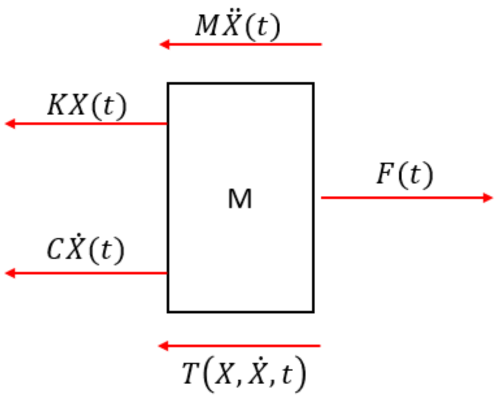

Figure 5: Forces acting on the system

Looking at Figure 5, the equation of motion of the system in Figure 4 can be written as follow:

$$F(t) - M\ddot{X}(t) - C\dot{X}(t) - KX(t) - T(X,\dot{X},t) = 0 \tag{1}$$

Changing all the signs the following equation can be written:

$$M\ddot{X}(t) + C\dot{X}(t) + KX(t) = F(t) - T(X,\dot{X},t) \tag{2}$$

Equation 2 is a second order differential equation and it cannot be solved directly because there is a non-linear term that depends on the displacement of the system, the friction force $T(X,\dot{X},t)$. The presence of a non-linear term in the equation causes the displacement not to be harmonic, even though the external forcing term is. The displacement of the system is not harmonic but assuming that is periodic, the MHBM method can be used to solve Equation 2. Considering that the displacement is not harmonic but periodic, it can be written as Fourier series:

$$X(t) = \bar{X}^0 + \sum_{n=1}^{nh} \bar{X}^{(n)} e^{in\omega t} \tag{3}$$

The same expression can be written for the friction force:

$$T(X,\dot{X},t) = \bar{T}^0 + \sum_{n=1}^{nh} \bar{T}^{(n)} e^{in\omega t} \tag{4}$$

In Equation 3 and Equation 4:

- $\bar{X}^0$ is the static Fourier coefficient of the displacement.
- $\bar{T}^0$ is the static coefficient of the non-linear friction force.
- $\bar{X}^{(n)}$ is the n-th Fourier coefficient of the displacement
- $\bar{T}^{(n)}$ is the n-th Fourier coefficient of the non-linear friction force.

Neglecting the static terms, that in real turbine applications are computed with a dedicated static analysis, and computing the derivatives of the displacement, Equation 2 can be rewritten as follow:

$$-(n\omega)^2 M \sum_{n=1}^{nh} \bar{X}^{(n)} e^{in\omega t} + i\omega C \sum_{n=1}^{nh} \bar{X}^{(n)} e^{in\omega t} + K \sum_{n=1}^{nh} \bar{X}^{(n)} e^{in\omega t} = \bar{F} e^{i\omega t} - \sum_{n=1}^{nh} \bar{T}^{(n)} e^{in\omega t} \tag{5}$$

Bringing together the similar terms at the first member of the Equation 5, the following expression can be written:

$$\sum_{n=1}^{nh} ((-n\omega)^2 M + in\omega C + K)\bar{X}^{(n)} e^{i\omega t} = \bar{F} e^{i\omega t} - \sum_{n=1}^{nh} \bar{T}^{(n)} e^{i\omega t} \tag{6}$$

In Equation 6 the time dependent term, $e^{i\omega t}$, can be simplified and the following equation is obtained:

$$\sum_{n=1}^{nh} ((-n\omega)^2 M + in\omega C + K)\bar{X}^{(n)} = \bar{F} - \sum_{n=1}^{nh} \bar{T}^{(n)} \tag{7}$$

Equation 7 is a set of coupled equations, known as harmonic balance equations, in fact for each harmonic component,n, can be written a non-linear equation in which the n-th harmonic component of the displacement depends on all others harmonic component. Defining the dynamic stiffness matrix as $D^{(n)} = (-n\omega)^2 + in\omega C + K$, the harmonic balance equations can be written as follows:

for $n = 1$

$$D^{(1)}\bar{X}^{(1)} = \bar{F} - \bar{T}^{(1)} \tag{8}$$

for $n > 1$

$$D^{(n)}\bar{X}^{(n)} = -\bar{T}^{(n)} \tag{9}$$

For simplicity of notation, in this example only the first harmonic component will be taken into account, but consider that in real turbine applications more than one harmonic components are always taken in non-linear calculations.
If only the fundamental harmonic component is considered, Equation 8 can be rewritten as follow:

$$D^{(1)}\bar{X}^{(1)} - \bar{F} + \bar{T}^{(1)} = R \tag{10}$$

Equation 10 is a non-linear equation in frequency domain, in which the unknown is the first Fourier coefficient of the displacement, $\bar{X}^{(1)}$. This non-linear equation cannot be solved directly, but an iterative non-linear solver is necessary. The iterative solver starts from an initial guess and performs some iterations, following for example a Newton-Raphson iteration scheme, until the residual function R is minimized. The main issue of this solution scheme is that at each iteration the value of the first Fourier coefficient of the friction force, $\bar{T}^{(1)}$, is required, so a further step is necessary. For this purpose is important to have a contact model, that take as input the displacement and come out with the friction force.
The following sub-section will discuss the most widely used contact models in the literature, then the discussion regarding the solution of Equation 10 will be taken up.

3.1.1 Contact models

This subsection will discuss about the input and output of the contact models and how the friction force is computed inside the single contact model.
There are three types of contact models:

- 1D contact model with fixed normal load.
- 2D contact model with variable normal load.
- 3D contact model with variable normal load and tangential stiffness along both X and Y direction.

The simplest contact model is the 1D contact model with fixed normal load, it is shown in Figure 6:

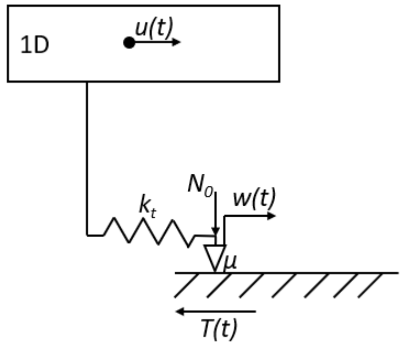

Figure 6: 1D contact model with fixed normal load

in which:

- $u(t)$ is the tangential displacement of the system in time domain.
- k_t is the tangential stiffness.
- N_0 is the preload acting on the contact element.
- μ is the friction coefficient.
- $w(t)$ is the displacement of the Jenkins contact element in time domain.
- $T(t)$ is the tangential friction force in time domain

The input of the contact model is the tangential displacement of the system in time domain, $u(t)$, then the tangential force in time domain is computed for the single time instant with a predictor-corrector model. The predictor always assumes that the system is in full stick condition:

$$T_{Predicted}(t) = k_t(u(t) - w(t)) \tag{11}$$

After the computation of the predicted tangential force there is the corrector step:

$$T(t) = \begin{cases} T_{Predicted} & stick \quad T_{Predicted}\mu N_0 \\ \mu N_0 sign(T_{Predicted}(t)) & slip \quad T_{Predicted} \geq \mu N_0 \end{cases} \tag{12}$$

The 1D contact model with fixed normal load does not take into account the fact that the normal load may vary and that there may be partial detachment between the contact surfaces. To take into account the variability of the normal load is necessary to use a 2D contact model, with a normal stiffness:

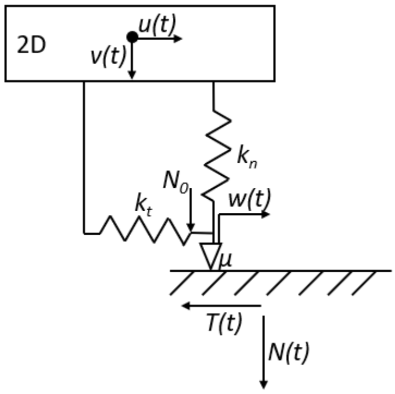

Figure 7: 2D contact model with variable normal load

in which:

- $u(t)$ is the tangential displacement of the system in time domain.
- $v(t)$ is the normal displacement of the system in time domain.
- k_t is the tangential stiffness.
- k_n is the normal stiffness
- μ is the friction coefficient.
- N_0 is the fixed preload acting on the contact element.
- $w(t)$ is the tangential displacement of the Jenkins contact element in time domain.
- $T(t)$ is the tangential friction force in time domain.
- $N(t)$ is the normal force in time domain

The normal force and the tangential one are respectively computed as follows:

$$N(t) = max(k_n v(t), 0) \tag{13}$$

$$T_{Predicted}(t) = k_t(u(t) - w(t)) \tag{14}$$

$$T(t)=\begin{cases} T_{Predicted}(t) & stick \\ \mu N(t) sign(T_{Predicted}(t)) & slip \\ 0 & separation \end{cases} \tag{15}$$

This contact model is capable to take into account the separation between the contact surfaces, computing more accurately the tangential friction force. In real turbines applications the contact surfaces between two adjacent blades are subject to a 3D displacement field, so to compute correctly the normal force and the tangential one a 3D contact model is necessary, which is shown in Figure 8:

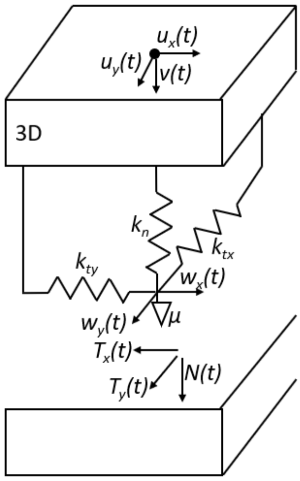

Figure 8: 3D contact model

in which:

- $u_x(t)$ is the tangential displacement of the system in X direction in time domain.
- $u_y(t)$ is the tangential displacement of the system in Y direction in time domain.
- $v(t)$ is the normal displacement of the system in time domain.
- k_t is the tangential stiffness.
- k_n is the normal stiffness.
- μ is the friction coefficient.
- N_0 is the fixed preload acting on the contact element.

- $w_x(t)$ is the tangential displacement of the Jenkins contact element in X direction in time domain.
- $w_y(t)$ is the tangential displacement of the Jenkins contact element in Y direction in time domain.
- $T_x(t)$ is the tangential friction force in X direction in time domain.
- $T_y(t)$ is the tangential friction force in Y direction in time domain.
- $N(t)$ is the normal force in time domain.

The normal force and the tangential ones are computed as follows:

$$T_{xPredicted}(t) = k_x(u_x(t) - w_x(t)) \tag{16}$$

$$T_{yPredicted}(t) = k_y(u_y(t) - w_x(t)) \tag{17}$$

$$N(t) = max(k_n v(t), 0) \tag{18}$$

$$T_x(t) = \begin{cases} T_{xPredicted}(t) & stick \\ \mu n(t) sign(T_x(t)) & slip \\ 0 & separation \end{cases} \tag{19}$$

$$T_y(t) = \begin{cases} T_{yPredicted}(t) & stick \\ \mu n(t) sign(T_y(t)) & slip \\ 0 & separation \end{cases} \tag{20}$$

In this subsection the most widely contact models used in literature were discussed, the next step is to integrate the contact model into the solution process of the Equation 10.

3.2 MHBM-AFT

Equation 10 is a non-linear equation in frequency domain, in fact the unknown is the first Fourier coefficient of the displacement. In order to compute the friction force at each solver iteration a contact model become necessary. For this example a 1 GDL system is considered, so a 1D contact model with fixed preload can be used

(what will be said for this example is extensible to systems with 2D and 3D contact models).
Let's consider the 1D contact model shown in Figure 6, it works in time domain, in fact the output is a time signal of the tangential friction force. To integrate the contact model into the solution process a further step is necessary: starting from the tangential force time signal the first Fourier coefficient must be computed. There are two possibilities to compute the Fourier coefficient of the friction force:

1. The first possibility is to write the analytical expressions of the friction force along all parts of the hysteresis cycle, and then to calculate the real and imaginary parts of the first Fourier coefficient with the following expressions:

$$\Re(\bar{T}^{(1)}) = \frac{1}{\pi}\int_{0}^{2\pi} T(t)cos(\omega t)dt \tag{21}$$

$$\Im(\bar{T}^{(1)}) = -\frac{1}{\pi}\int_{0}^{2\pi} T(t)sin(\omega t)dt \tag{22}$$

2. The second possibility is to process the tangential force time signal with the FFT algorithm and take only the first Fourier coefficient of the frequency output.

The first approach is completely analytical and provide the correct Fourier coefficient. The main drawback with this approach is that in order to be applied the hysteresis cycle must be known a priori. The hysteresis cycle is known in advance only for few simple cases, in fact in real turbine applications is very often very difficult or even impossible to derive the analytical expressions of the friction force.
The second approach is much more versatile, in fact the FFT algorithm is able to process any input signal, so it is always preferred and the most adopted method in literature. The main drawback with this approach is the time discretization, in fact for some cases (for example intermittent contact) is necessary to oversample the force time signal to not have aliasing errors, as reported by [41] .
This time-frequency switch is known as AFT(Alternating Frequency Time) scheme, and was introduced by [42]. In Figure is shown a scheme representing the MHBM with AFT scheme for solving Equation 10:

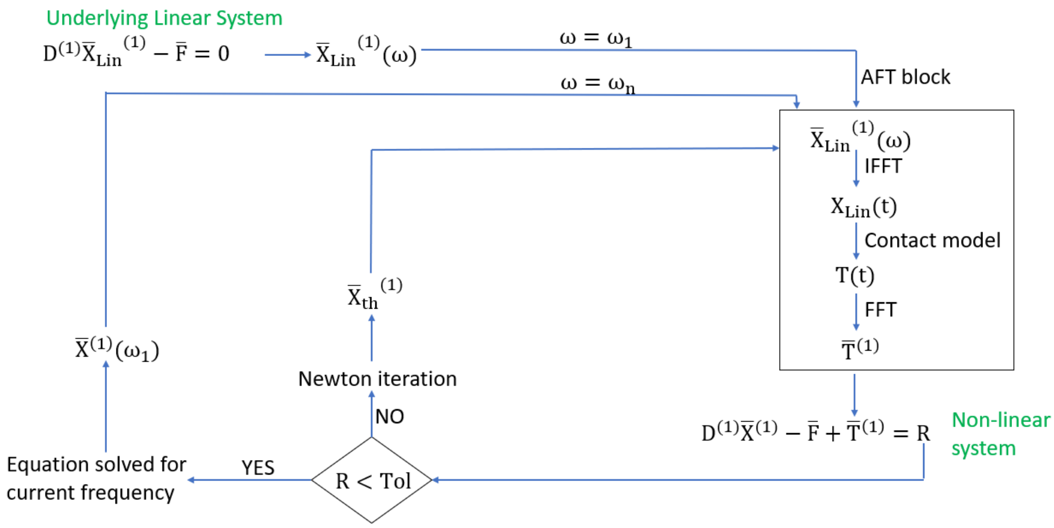

Figure 9: MHBM-AFT solution scheme

The solution process can be summarized in the following steps:

- The first step is to solve the ULS, in wich the non-linear term is neglected. This step is necessary to have the initial guess for the first frequency value of the analyzed frequency range.
- The linear displacement calculated for the first frequency value is the input for the AFT block.
- The linear displacement is a complex number, but the contact model works in time domain, so it is necessary to process the displacement with the IFFT algorithm in order to switch in time domain.
- The displacement time signal is the input for the contact model, that give as output the tangential friction force in time domain.
- Equation 10 must be solved in frequency domain, so the tangential friction force in time domain is processed with the FFT algorithm in order to compute the first Fourier coefficient of the friction force.
- At this step both the displacement and the friction force in time domain are computed, so the residual function can be evaluated.
- If the residual function is over the set tolerance a Newton iteration is performed and the next displacement computed is the new input for the AFT block.

- The previous step is repeated until the residual function is below the set tolerance. When the residual function is less than the set tolerance the equation is solved for the current frequency, and the solution is the initial guess for the next frequency solution process.
- This solution scheme is repeated until the non-linear equation is solved for all frequency values of the frequency range of interest.

3.2.1 Pseudo Arc Length continuation solution scheme

The solution scheme shown in Figure 9 is known as natural continuation scheme. This solution method works very well if during vibrations no detachment of contact surfaces occurs. This is a very simplified situation, in fact in real turbines applications the blades experience 3D displacements field, so there is also a normal relative displacement between the contact surfaces of two adjacent blades. The normal relative displacement can significantly influence the non-linear response, in fact during vibrations some points can lose contact intermittently, causing the appearance of "turning points" in the FRF curve. In Figure 10 is shown an example of turning point:

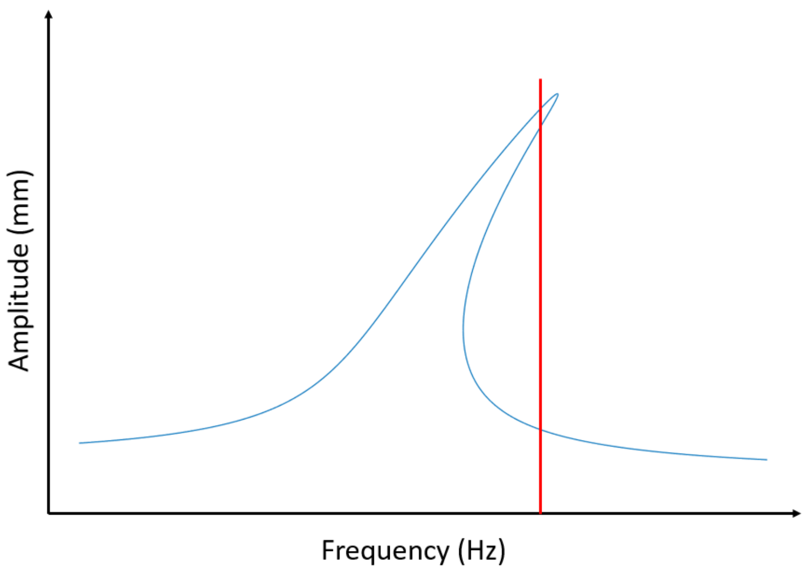

Figure 10: Turning point in non-linear FRF curve

In Figure 10 can be observed that the non-linear FRF curve exhibit a turning point, in fact there is a frequency value beyond which the curve bends in on itself. This particular shape of the FRF causes that for a single frequency value two or more solutions in terms of physical displacements are possible. This behavior entails convergence issues with natural continuation, this is because with this computational scheme the frequency step is imposed, so once the turning point is passed it forces the solver to minimize the residual function at a point outside the solution curve, leading the solution scheme to fail.
To get around this issue the frequency should not be imposed but should become an unknown of the problem. This approach is known in literature as pseudo arc length continuation method, widely discussed and shown by [43]. The first version of the code for Ansaldo's non-linear tool was developed by implementing only the classical MHBM method. During my research, I improved the tool's robustness by also implementing the Pseudo Arc Length Continuation method within it.
The pseudo arc length continuation technique is able to get around turning points because an additional constraint is added to the residual function, this causes the frequency to become an unknown of the problem, in this way the solver is able to follow the solution curve, calculating also the multiple solutions. To understand the constraint that is added to the residual function, let's consider a graphical representation of the pseudo arc length continuation technique, shown in Figure 11:

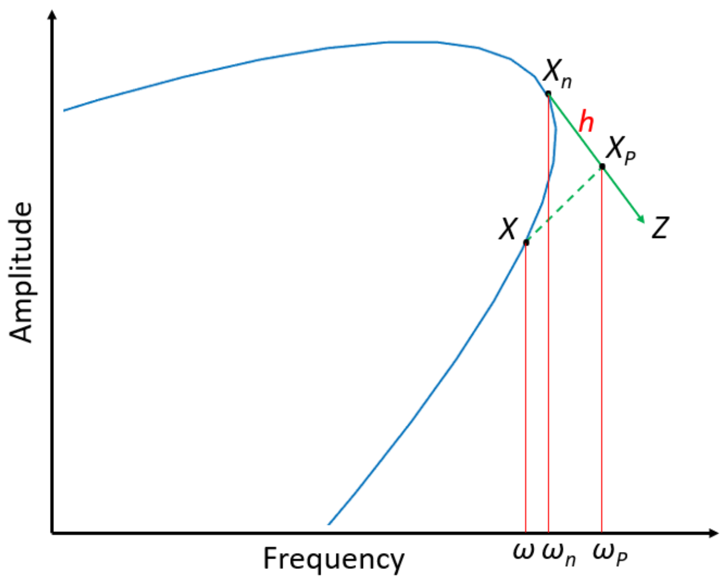

Figure 11: Graphical representation of the Pseudo Arc Length continuation technique

Referring to Figure 11, how pseudo arc length continuation works will be widely discussed. First of all let's define all the variables:

- X_n is the starting point, that is the solution for the frequency ω_n. The vector y_n can be defined as: $y_n = \begin{pmatrix} \Re(X_n) \\ \Im(X_n) \\ \omega_n \end{pmatrix}$
- h is the step length along the tangent vector.
- Z is the tangent vector computed at the point X_n, that is composed by three components: $Z = \begin{pmatrix} Z_1 \\ Z_2 \\ Z_3 \end{pmatrix}$
- X_p is the predicted point along the tangent vector at the frequency ω_p. The vector y_p can be defined as: $y_p = \begin{pmatrix} \Re(X_p) \\ \Im(X_p) \\ \omega_p \end{pmatrix}$
- X is the unknown displacement at frequency value ω. The vector y can be defined as: $y = \begin{pmatrix} \Re(X) \\ \Im(X) \\ \omega \end{pmatrix}$

The goal is to find the unknown displacement X and the unknown frequency ω. The solution process can be summarized in the following steps:

- The first step is to compute the tangent vector Z at the known solution point X_n.
- Then the predictor step is performed to reach the point X_p: $y_p = y + hZ$. The vector y_p is the initial guess for the non-linear solver.
- The third step is the corrector step, in which some iterations are performed following the direction perpendicular to the tangent vector (linear constraint) to reach the solution point y.
- The previous steps are repeated for each curve solution point, until all the non-linear FRF is computed.

This solution procedure is known as a predictor-corrector technique, that is able to get around turning points, avoiding convergence issues.
What was discussed previously was just a graphical point of view of this continuation technique, now the pseudo arc length continuation will be discussed also from mathematical point of view and how it can be embraced in MHBM-AFT scheme will be shown.
Let's consider the system shown in Figure:

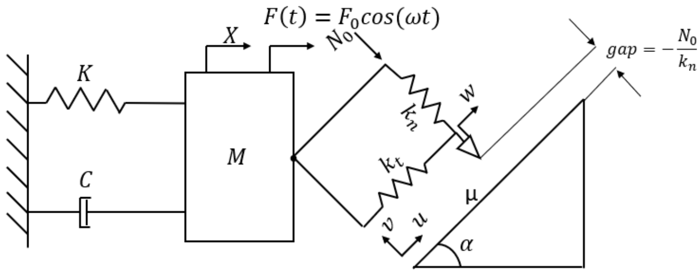

Figure 12: 1 GDL system with 2D contact model

in which:

- K is the stiffness of the system.
- C is the linear damping of the system.
- M is the mass of the system.
- X is the displacement of the mass in global reference system.
- $F(t)$ is the external excitation force.
- u is the tangential displacement of the mass in the local contact reference system.
- v is the normal displacement of the mass in the local contact reference system.
- k_t is the tangential stiffness of the contact element.
- k_n is the normal stiffness of the contact element
- w is the tangential displacement of the contact element.

- α is the inclination of the ground.
- N_0 is the preload acting on the contact element.
- μ is the friction coefficient.
- *gap* is the initial distance between the mass and the ground

The system represented in Figure 12 is very similar to the one shown in Figure 4, the main difference is that in this case the mass is in contact with an inclined ground. Considering the global reference system, the displacement is 1D, while in the local contact reference system there are two component displacement, tangential and normal, thus the friction force will depend also on the variable normal displacement. To take into account of this aspect become necessary to have a 2D contact model with both tangential and normal stiffness. In this example is also considered a gap, that take into account the possible initial distance between two contact surfaces. The gap and the variable normal load influence significantly th non-linear response of the system, causing turning points in the FRF curve, so in MHBM-AFT scheme is necessary to add the pseudo arc length continuation constraint.
The equation of motion of the system in Figure 12 can be written, similarly to Equation 10, as follows:

$$D^{(1)}\bar{X}^{(1)} - \bar{F} + \bar{T} = R_1 \tag{23}$$

Considering what was discussed before, the residual function R_1 must be coupled with pseudo arc length continuation constraint to embrace this continuation technique in MHBM-AFT scheme. The augmented system can be written as follows, the complex terms are expanded in real and imaginary parts:

$$\begin{cases} \begin{bmatrix} D_{11} & D_{12} \\ D_{12} & D_{22} \end{bmatrix}^{(1)} \begin{pmatrix} \Re(\bar{X}^{(1)}) \\ \Im(\bar{X}^{(1)}) \end{pmatrix} - \begin{pmatrix} \Re(\bar{F}) \\ \Im(\bar{F}) \end{pmatrix} + \begin{pmatrix} \Re(\bar{T}^{(1)}) \\ \Im(\bar{T}^{(1)}) \end{pmatrix} = \begin{pmatrix} \Re(R_1) \\ \Im(R_1) \end{pmatrix} \\ \left(\begin{pmatrix} \Re(\bar{X}_p^{(1)}) \\ \Im(\bar{X}_p^{(1)}) \\ \omega_p \end{pmatrix} - \begin{pmatrix} \Re(\bar{X}^{(1)}) \\ \Im(\bar{X}^{(1)}) \\ \omega \end{pmatrix} \right)^T \begin{pmatrix} Z_1 \\ Z_2 \\ Z_3 \end{pmatrix} = R_2 \end{cases} \tag{24}$$

The first term of the system of equations 20 is equal to Equation 10, while the second term is the pseudo arc length continuation constraint. From mathematical point of view this constraint is a scalar product between the vector connecting the predicted point and the searched one and the tangent vector. Minimizing this residual term means that the solver iterations are following a direction that is perpendicular to the tangent vector, being able to get around turning points and finding the solution curve. The solution scheme that embrace pseudo arc continuation constraint is shown in:

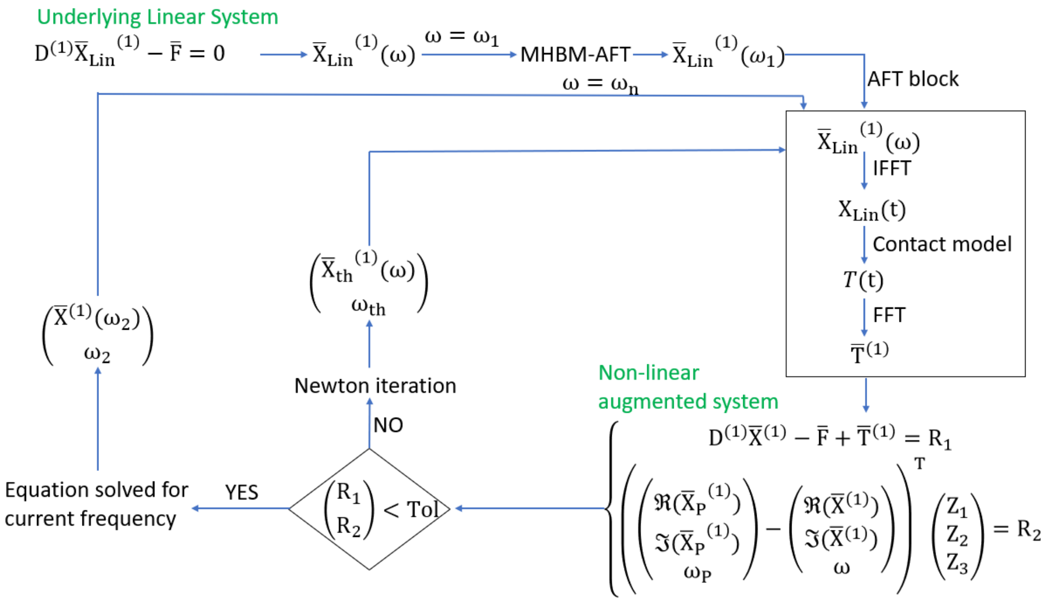

Figure 13: MHBM-AFT solution scheme with pseudo arc length continuation constraint

The solution process represented in Figure 13 can be summarized into the following steps:

- The first step is always the solution of the ULS, that provide the initial guess for the first frequency of the studied range.
- The solution to the non-linear equation for the first frequency must be calculated using the MHBM-AFT scheme discussed above. This is because for the first frequency I do not have two adjacent solutions to calculate the tangent vector and find the predicted point along that vector.
- The non-linear displacement calculated for the first frequency is the input for the AFT block, in which it is processed with the IFFT algorithm, to switch in time domain.

- The displacement in time domain is the input for the contact model, that come out with the friction force in time domain.
- The friction force time signal is processed with the FFT algorithm in order to compute the first Fourier coefficient of the friction force.
- The next step is to evaluate the residual terms with the current displacement and friction force.
- If the residual terms are over the set tolerance values, a Newton iteration is performed and the value of displacement computed is the new input for thr AFT block.
- The previous step is performed until the residual terms are under the set tolerances.
- When the residual terms are minimized, the system of equations is solved for the current frequency.
- This solution process is repeated until all the frequency range of interest is covered and the FRF curve is computed.

Summarizing what was discussed in this section, the natural continuation is a solution technique that works very well if the FRF curve doesn't show turning points, while convergence problems arise when turning points appear in the solution curve. This is due to the fact that with natural continuation the frequency step is imposed, so when the solver go through a turning point tries to minimize the residual function on a point out from the solution curve, so it will not be able to converge.
To avoid this convergence issues is necessary to adopt a MHBM-AFT solution scheme coupled with pseudo arc length continuation technique. With this approach, the frequency is no longer imposed but become an unknown of the problem, so the solver is able to get around turning points, ensuring the solution convergence. The main drawback of the pseudo arc length continuation technique is the computation time, in fact to ensure the convergence the step taken along the tangent vector must be small enough, so also the frequency step will be small. This results in higher but inevitable computation times.

Chapter 4

Generation of an efficient reduced-order model for non-linear forced response computation

The purpose of this chapter is to explain in detail all the steps necessary to generate an efficient reduced order model for calculating the non-linear forced response. Ansaldo's non-linear tool takes the reduced mass and stiffness matrices, obtained from the full FEM model, as input and returns the non-linear displacement as output. Figure 14 shows a general scheme of the non-linear forced response computation with the Ansaldo's non-linear tool:

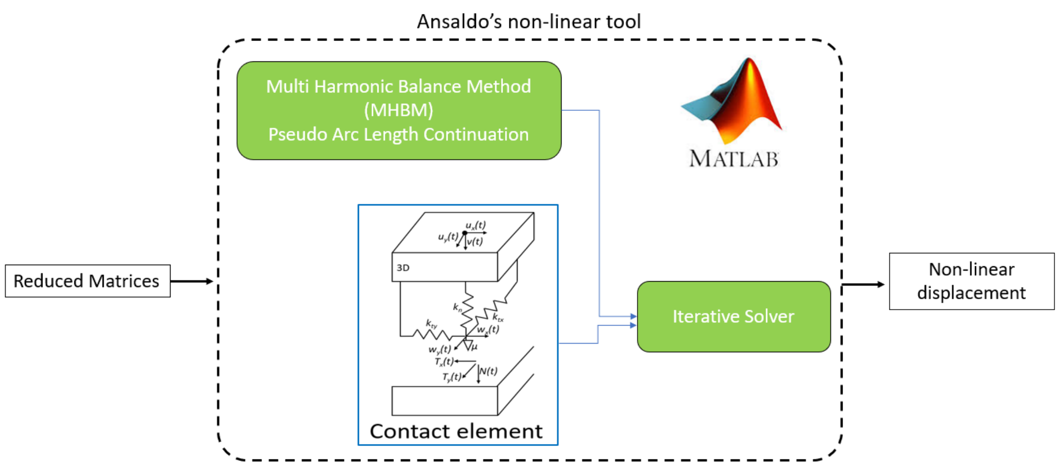

Figure 14: Non-linear forced response computation scheme

As can be seen in Figure 14, the input for calculating the non-linear forced response is represented by the matrices of the reduced model.
The equation of motion of the reduced model is solved using the solution methods widely discussed in Chapter 3.
As mentioned above, the objective of this doctoral thesis is to calculate the dynamic stresses on turbine blades with friction contacts.
In order to calculate the stresses accurately, it is first necessary to calculate the non-linear response accurately, as the displacements of the system are closely related to the stresses.
In order to optimally calculate the forced non-linear response, it is necessary to generate an efficient reduced model that takes into account all the effects that influence the reduced matrices.
As discussed in the introduction to this thesis, blades that are subject to high static displacements, such as the blades of the last stage blades of the Ansaldo steam turbine, introduce a problem in the reduction process. In fact, these displacements must be taken into account, otherwise the obtained reduced model is unable to correctly simulate the dynamic behaviour of the full system.
The following sections will discuss and explain in detail all the steps necessary to obtain an efficient reduced-order model that takes into account all the effects that influence the calculation of the non-linear forced response and, consequently, leads to an accurate calculation of the dynamic stresses on the blades.

4.1 Generation of the Reduced Order Model (ROM)

The generation of a reduced order model is the fundamental step in performing a non-linear forced response calculation with the Ansaldo's non-linear tool. the Ansaldo's non-linear tool takes as input the mass and stiffness matrices of the reduced system, which are obtained through a dynamic sub-structuring process in the Ansys environment. The sub-structuring process allows a series of physical degrees of freedom, called master nodes, and a series of modal degrees of freedom to be condensed within the reduced matrices. The physical degrees of freedom that are condensed within the reduced model must ensure excellent reproducibility of the dynamic behavior of the full FEM model and are usually divided into three types:

- Force node: this is the physical node on which the external force is applied.
- Response nodes: these are the physical nodes used for plotting the non-linear displacement of the system.
- Contact nodes: these are the physical nodes on which the friction forces generated by the relative motion between two adjacent blades act. Friction forces are non-conservative forces and depend on the relative displacements of the nodes themselves. Therefore, in order to calculate the displacements of the contact nodes, an iterative solution is necessary because the system is non-linear.

To obtain reduced mass and stiffness matrices, it is not sufficient to perform only a dynamic substructuring process, as it is necessary to take into account all the effects due to static forces acting on the blade, such as centrifugal force and static contact forces. Static forces modify the stiffness of the system, so it is essential to consider them in the reduction process in order to ensure a correct modal calculation on the reduced model. Considering static forces in the reduction process requires several preliminary steps, which are shown in Figure 15:

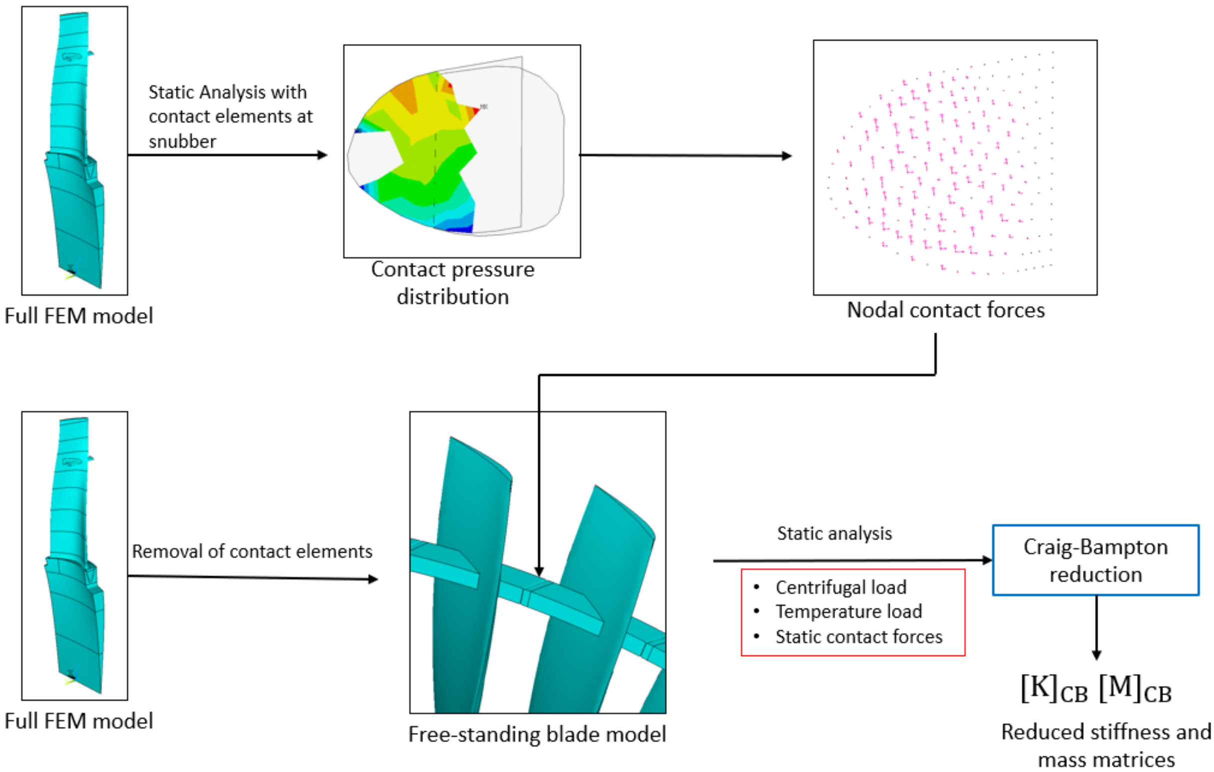

Figure 15: Reduced Order Model generation scheme

Figure 15 shows the steps required to obtain the reduced mass and stiffness matrices, including the effects of static forces. The Reduced Order Model (ROM) generation process can be summarized in the following steps:

- Static analysis performed with contact elements on the snubber contact nodes and subsequent evaluation and extraction of the contact nodal forces acting on snubber contact nodes.
- Static analysis performed without contact elements on snubber contact nodes, importing as static forces those obtained with the previous static analysis. This step allows to simulate the effect of the static friction forces without including the contact elements in the reduced model. The contact elements that couple the contact nodes will be placed in the Ansaldo's non-linear tool, for this reason is crucial to non include ANSYS contact elements in the reduced order model.

- Craig-Bampton reduction. This is the final step and as output produces the reduced mass and stiffness matrices.

The entire procedure summarized above and the procedure that will be discussed in next chapters are applied on the last stage blades of the Ansaldo steam turbine. A detail that should not be overlooked is that all the procedure described so far will be performed on the FEM model without cyclic symmetry constraints, because the cyclic symmetry boundary conditions are defined in the Ansaldo's non-linear tool with the nodal diameter input. In the FEM model used, cyclic symmetry surfaces are constrained using the cp command, which defines constraint equations for the selected nodes. This allows only the zero nodal diameter to be considered for subsequent analyses.
The reduced matrices are only a part of the inputs required by the Ansaldo's non-linear tool to calculate the non-linear forced response. Another fundamental input is the preload matrix, which defines the static, normal and tangential preloads acting on the contact elements. To avoid convergence problems in the Ansaldo's non-linear tool, it is important that these preloads are extracted correctly.
The following sections will discuss in detail all the preliminary steps necessary to obtain the reduced matrices.

4.2 Step 1: static analysis performed with contact elements on snubber nodes

This section focuses on a detailed description of the static analysis performed by inserting contact elements on the snubber nodes.
Specifically, an asymmetric contact type was defined for this analysis, which allows the contact forces to be calculated on a single surface, thus making it easier to define the external forces for the subsequent static analysis performed without the contact elements. This aspect will be clarified later.
Before continuing, it is important to define the loads used for this analysis:

- Centrifugal load: this load represent the angular velocity of the turbine during its operation, 3000 *rpm*.

- Temperature load: this is a thermal load, simulating the effect of the temperature on the blade.

Figure 16 shows the contact surfaces and the corresponding contact elements adopted for this static analysis:

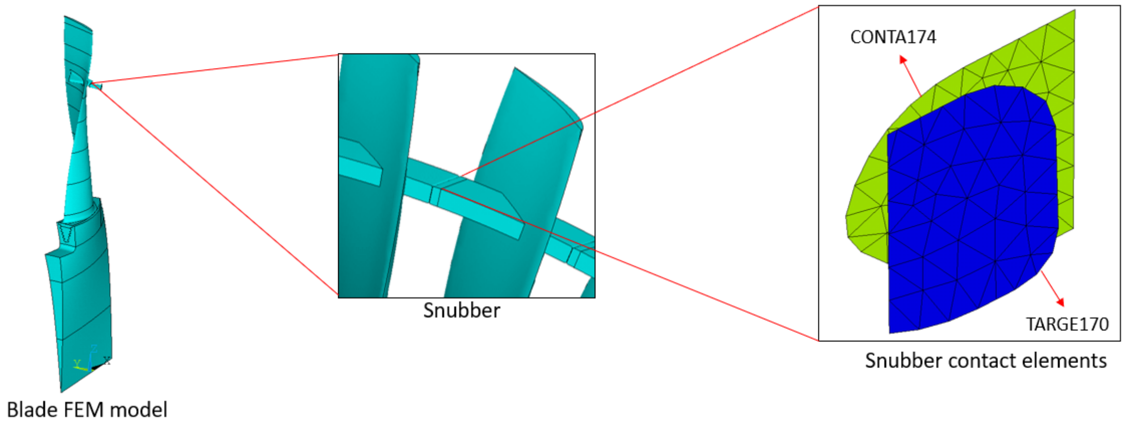

Figure 16: Snubber contact elements

As shown in Figure 16, the contact elements used for this static analysis are:

- CONTA174: these are the elements on which the stresses and contact forces are actually calculated. They are defined on the suction side contact surface.
- TARGE170: no quantities are calculated on these elements. They are defined on the pressure side contact surface.

This step is essential as it allows the static preloads to be obtained, which constitute an input for both the Ansaldo's non-linear tool and the subsequent static analysis. However, particular attention must be paid to the reference system from which the contact forces will be extracted. The blades of the last stages are usually very long, which means that the displacements in the tip area are very large. The snubber is located near the tip, which means that it is located in an area subject to high deformations. Consequently, the snubber surfaces undergo large translations and rotations before coming into contact. The deformation of the blade cannot be neglected, otherwise the contact forces are calculated in a reference system that is not consistent. To better understand this aspect, consider Figure 17:

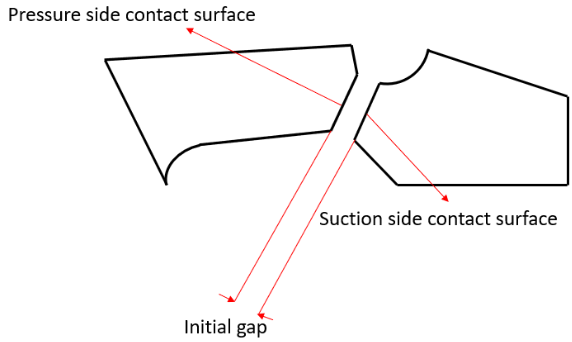

(a) Undeformed snubber geometry: open contact

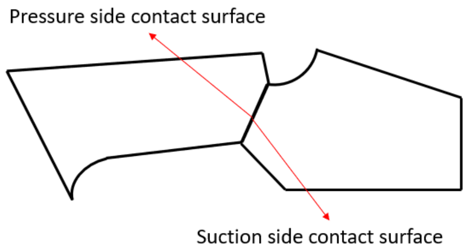

(b) Deformed snubber geometry: closed contact

Figure 17: Snubber geometry

Figure 17 clearly shows what was stated above, namely that the snubber undergoes significant translation and rotation, due to centrifugal load, before its surfaces come into contact and the initial gap is closed.
The focus must now be placed on the contact surface of the suction side, on which the CONTA174 contact elements have been defined. These contact elements are those on which the static contact pressures and forces are actually calculated. Consider Figure 18, which shows two different cases:

- Case 1: The blade is in undeformed condition and it is defined a local coordinate system on the snubber suction side contact surface that will be identified as 21.

- Case 2: The blade is in deformed condition and it is defined a local coordinate system on the snubber suction side contact surface that will be identified as 11. In this case is also shown the blade undeformed condition.

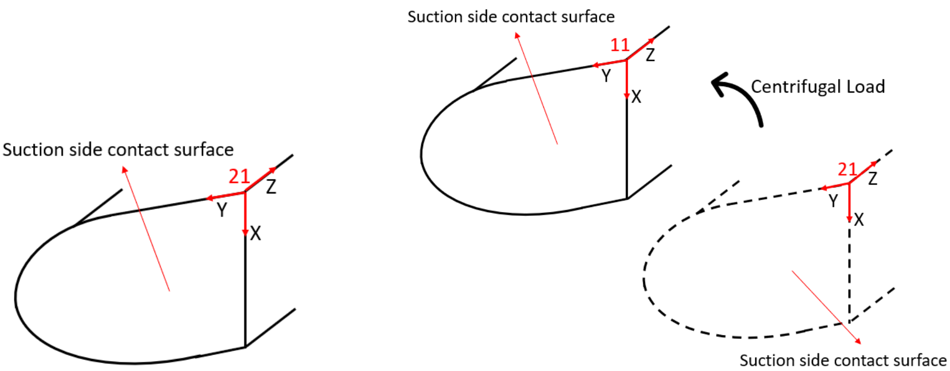

(a) Case 1 (b) Case 2

Figure 18: Local coordinate systems defined on the snubber suction side contact surface

As mentioned above, the two cases shown in Figure 18 refer to two conditions: one condition in which the blade is not subjected to any load, Figure 18a, and one condition in which the blade deforms due to centrifugal load, Figure 18b.
Reference system 21 was defined on the undeformed geometry, so when the snubber surfaces move due to centrifugal load, this reference system is no longer consistent with the snubber contact surfaces, in fact remains in the position of the undeformed geometry (dotted line in Figure 18a).
If the contact forces are extracted in reference system 21, incorrect components are considered because the tangential and normal components are no longer consistent with the contact surface.
To consider the correct components of the contact forces, it is necessary to define a local reference system downstream of the static analysis, so that this reference system is consistent with the contact surfaces of the snubber. As can be seen in Figure 18b, reference system 11 is consistent with the contact surfaces of the snubber, as it has been defined on the deformed geometry.
To clarify what has been discussed above, consider Figure 19, which shows the previous problem from a mathematical point of view. For convenience of representation, the example will be carried out only for a single contact node, 251363, but the reasoning remains valid for all contact nodes on the surface:

RSYS 21					
Node	X Force	Y Force	Z Force	Force resultant in XY plane	Friction coefficient
251363	$T_X = -1.32$	$T_Y = 0.28$	$N = 2.35$	$T_{XY} = \sqrt{T_X{}^2 + T_Y{}^2} = 1.35$	$\mu = \frac{T_{XY}}{N} = 0.57$

(a) Local contact forces in reference system 21

RSYS 11					
Node	X Force	Y Force	Z Force	Force resultant in XY plane	Friction coefficient
251363	$T_X = -0.57$	$T_Y = -1.07$	$N = 2.42$	$T_{XY} = \sqrt{T_X{}^2 + T_Y{}^2} = 1.35$	$\mu = \frac{T_{XY}}{N} = 0.5$

(b) Local contact forces in reference system 11

Figure 19: Local contact forces

In which:

- RSYS 21 is the local reference system 21, look at Figure 18.
- RSYS 11 is the local reference system 11, look at figure 18.
- T_X is the tangential component of the friction force along X direction,in Newton, evaluated the local reference system.
- T_Y is the tangential component of the friction force along Y direction, in Newton, evaluated in the local reference system.
- T_{XY} is the resultant of the tangential friction forces,in Newton, on XY plane.
- N is the normal component of the friction force, in Newton evaluated in the local reference system.
- μ is the friction coefficient.

Referring to Figure 19, note that the friction coefficient is defined as the ratio between the resultant of the tangential forces on the XY plane and the normal component to the same plane. Refer to Figure 18 for the XYZ axes.
Consider Figure 19a, in which the calculation of the friction coefficient is performed by considering the components of the static contact forces taken in reference system 21. For the calculation of the friction coefficient to be consistent, the ratio between the resultant of the tangential forces and the normal force must return the friction

coefficient value defined for the FEM model, which in this case has been set to $\mu_{FEM} = 0.5$.
The friction coefficient calculated in Figure 19a is $\mu = 0.57$, which differs from that of the FEM model. This occurs because the components of the static contact forces are considered in reference system 21, which is not consistent with the contact surfaces of the snubber.
Looking at Figure 19b, we can see that the calculated friction coefficient is exactly 0.5. In this case, the calculated friction coefficient coincides with that defined for the FEM model, because the components of the static contact forces are considered in reference system 11, consistent with the contact surfaces of the subber.
This intermediate step is essential as it allows two objectives to be achieved:

- obtaining the correct preloads for the Ansaldo's non-linear tool and, consequently, calculating a more accurate non-linear forced response.
- obtaining an input for the subsequent static analysis, which will be discussed in detail in the next section.

All subsequent considerations regarding local contact forces will be made considering reference system 11, consistent with the blade deformation.

4.3 Step 2: static analysis performed without contact elements on snubber nodes

This section focuses on a detailed description of step 2, a static analysis performed by removing the contact elements on the snubber nodes. As mentioned above, ANSYS contact elements should not be included in the reduced model, because the Ansaldo's non-linear tool defines its contact elements on contact nodes. Having ANSYS contact elements in the reduced model could lead to incorrect natural frequencies computation and, consequently, to an inaccurate forced response analysis.
The easiest way to reduce the model without including ANSYS contact elements is to perform a preliminary static analysis on the free-standing blade model before the substructuring process. However, this solution is not optimal as it only considers the effect of centrifugal force, neglecting the effect of contact forces acting on the snubber, which significantly modify the blade displacement field and, consequently,

the stiffness matrix of the system. To consider both the effect of centrifugal force and the effect of contact forces, a static analysis was performed by imposing the following loads:

- Centrifugal load: this load represents the angular velocity of the turbine during its operation, 3000 *rpm*.
- Temperature load: this is a thermal load, simulating the effect of the temperature on the blade.
- Contact forces: this load simulates the interaction between the contact surfaces of the snubber. This point will be discussed in detail below.

Figure 20 shows all the steps necessary to perform the static analysis without the contact elements on the snubber, but still simulating the interaction between the contact surfaces:

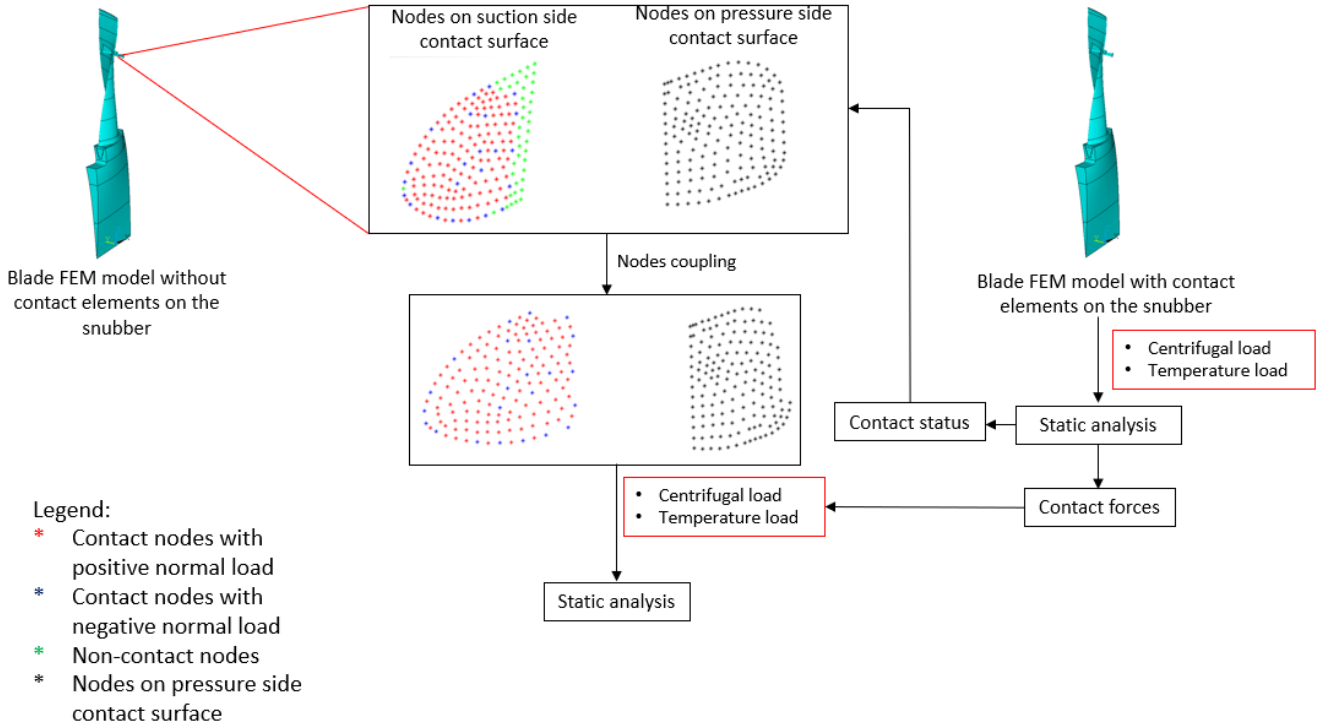

Figure 20: Static analysis without contact elements on the snubber

The following explains in detail what is shown in Figure 31. The starting point is to perform a static analysis by inserting the contact elements on the snubber, from which it is possible to obtain the following:

- The contact forces (in reference system 11).
- The contact status, necessary to identify which nodes on the suction side surface of the snubber ANSYS considers to be in contact.

As can be seen in Figure 20, different colours have been used to differentiate the nodes on the suction side surface of the snubber:

- The nodes highlighted in red are those that ANSYS considers to be in contact and on which the normal force is positive.
- The nodes highlighted in blue are those that ANSYS considers to be in contact and on which the normal force is negative.
- The nodes highlighted in green are those that ANSYS considers to be detached.

Once the nodes that ANSYS considers to be in contact have been identified, those highlighted in blue and red, they must be paired with the nodes located on the contact surface of the pressure side to obtain pairs of contact nodes.
The nodes are paired according to distance:

- The distance between each node on the suction side surface of the snubber that ANSYS considers to be in contact and all nodes on the pressure side surface of the snubber is calculated.
- The previous step produces a distance matrix, whose number of rows is equal to the number of nodes on the surface of the suction side of the snubber that ANSYS considers to be in contact, while the number of columns is equal to the number of nodes on the surface of the pressure side of the snubber.
- From the previous matrix, as many elements as the number of nodes on the suction side surface of the snubber that ANSYS sees in contact (nodes highlighted in blue and red in the previous figure) are taken in ascending order.

- For each element extracted in the previous step, the position within the distance matrix is evaluated and the node pair is thus defined.

For convenience of notation, for each contact pair, the nodes on the suction side surface of the snubber will be called SS node, while the nodes on the pressure side surface of the snubber will be called PS node. After generating the node pairs, the static analysis can be performed by applying the following loads:

- Centrifugal load: this load represents the angular velocity of the turbine during its operation, 3000 rpm.
- Temperature load: this is a thermal load, simulating the effect of the temperature on the blade.
- Contact forces: The contact forces resulting from the static analysis performed at step 1 are applied to each of the SS nodes. The same contact forces are applied to the PS node coupled to the single SS node, but with the opposite sign. This allows the interaction between the contact surfaces to be simulated without physically defining contact elements in the model.

Previously, it was highlighted that performing a static analysis on the free-standing blade was not sufficient, as this would neglect the effect of contact forces, which have a significant impact on the displacement field and, consequently, on the stiffness matrix of the system. Figure 21 shows the comparison between the displacements computed with the static analysis performed on step 2 and those computed on the free standing blade model:

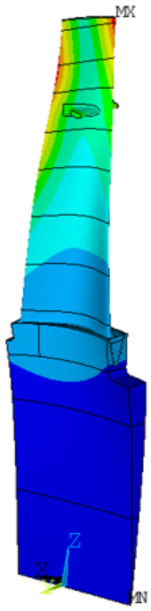

(a) Displacement field computed with the static analysis performed at step 2

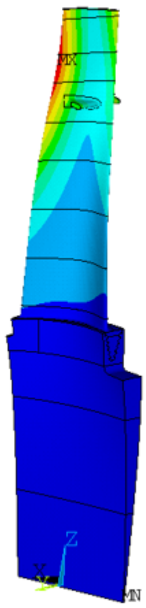

(b) Displacement field computed with the static analysis performed on the free-standing blade

Figure 21: Displacement field

Note: the displacement values cannot be displayed for confidentiality agreements with Ansaldo Energia.
Figure 21 shows that the displacements calculated considering the free-standing blade are very different from those calculated using the procedure discussed in this section. This is due to the fact that in the first case the contact forces are neglected, consequently the blade deforms more because it has fewer constraints. As can be seen from Figure 21, the difference between the displacements is not negligible, so not considering the effect of contact forces would lead to an incorrect calculation of the stiffness matrix of the reduced system and, consequently, of the natural frequencies, making the non-linear forced response analysis less accurate.
To ensure that the procedure is consistent, it is necessary to compare the displacements calculated with the static analysis performed in step 1 with the static analysis performed in step 2. The results obtained are shown in Figure 22:

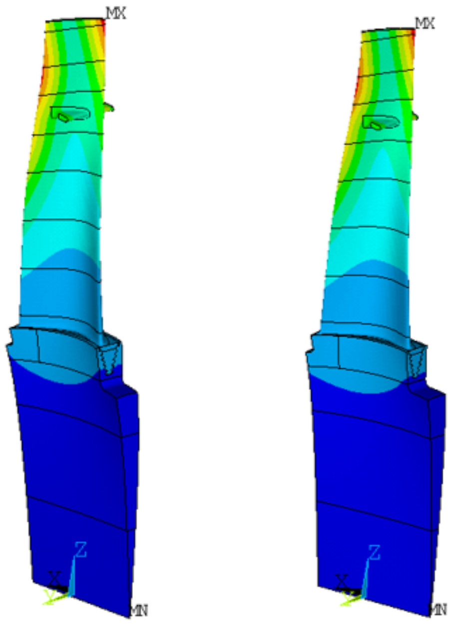

(a) Displacement field computed with the static analysis performed at step 1

(b) Displacement field computed with the static analysis performed at step 2

Figure 22: Displacement field

Looking at Figure 22, we can conclude that the procedure adopted in this section is robust. In fact, the difference between the displacements calculated in step 1 and those calculated in step 2 is negligible, with a maximum relative error of approximately 2 %. The result of the static analysis performed in this step constitutes the input for the model reduction, which will be discussed in the next section.

4.4 Step 3: Craig-Bampton reduction

This section focuses on the final step, which produces the reduced mass and stiffness matrices, that constitute the main input for the Ansaldo's non-linear tool. The starting point for the Craig-Bampton reduction process is the result obtained in the previous section, which allows the effects of static forces to be included in the reduced model. Figure 23 shows the model order reduction scheme:

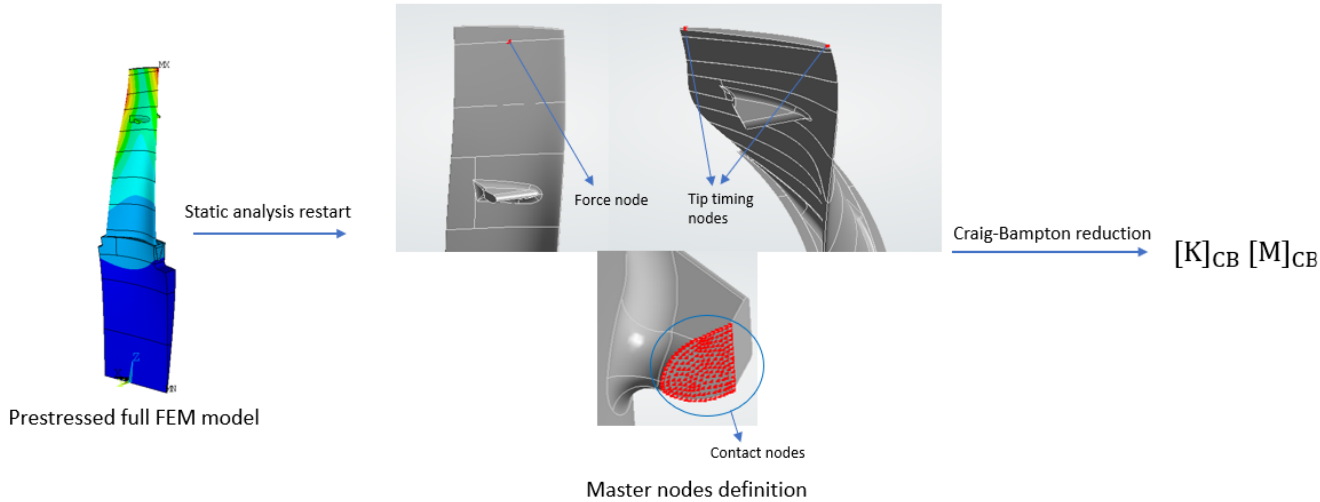

Figure 23: Craig-Bapmton reduction

In Figure 23 is shown the last part of the entire process for the generation of the Reduced Order Model (ROM) and the reduced matrices.
The previous section was focused on the static analysis performed without the contact elements on the snubber, that is the starting point for the Craig-Bampton reduction. The scheme shown in Figure 23 can be summarized as follows:

- The first thing to do is to restart the static analysis performed in step 2: this allows all the effects of static forces (centrifugal force and contact forces) to be taken into account in the generation of the reduced matrices.
- Next, the master nodes are defined: master nodes are the physical nodes that you decide to keep in the reduced model. It is important to remember that, in addition to the physical nodes, a certain number of modal degrees of freedom are retained in the reduced model.
- The final step in the process is the model reduction. For this doctoral thesis, the Craig-Bampton condensation technique, already implemented in the commercial ANSYS calculation software, was used.

The outputs of the three steps discussed in previous sections are:

- The static preloads on the contact elements that are defined in the Ansaldo's non-linear tool and the contact pairs. This input is obtained in step 2, where you need to extract the static preloads to perform the static analysis without the contact elements on the snubber.

- The reduced mass and stiffness matrices. In These matrices are condensed a certain number of physical and modal degrees of freedom. It is important to clarify something regarding contact pairs. Only contact pairs on which the normal force is greater than zero are condensed in the reduced matrices, because the pairs on which the normal force is negative are detached.

- The master nodes, that are used by the Ansaldo's non-linear tool for the definition of the excitation level, the contact elements and the non-linear response output.

These three items constitute the inputs for the Ansaldo's non-linear tool, and at this point it is possible to set up and perform a non-linear forced response calculation. Everything related to the Ansaldo's non-linear tool's output will be discussed in detail in the next chapter.
The three steps discussed in this chapter are of fundamental importance, as they allow us to obtain a reduced-order model that takes into account:

- Blade deformation.

- The effect of static contact forces.

As has been demonstrated, these effects are not negligible and influence the calculation of the non-linear forced response. Neglecting blade deflection leads to an incorrect calculation of the components of the static contact forces, which constitute one of the inputs for the non-linear solver. If this input is incorrect, it can lead to convergence problems in the non-linear calculation.
Neglecting the effect of static contact forces leads to an incorrect calculation of static displacements and consequently introduces an error in the reduction process. The output of the FEM model reduction is the reduced mass and stiffness matrices. The stiffness matrix is strongly influenced by static displacements. Therefore, reducing an FEM model with an incorrect displacement field results in an inconsistent stiffness matrix for the reduced model. If the stiffness matrix is inaccurate, this leads to an incorrect calculation of the natural frequencies of the reduced model and, consequently, of the non-linear forced response.

The outputs of the non-linear forced response analysis are the non-linear displacements, calculated at specific points in the system, and the friction forces, which act on the nodes at the contact interface. Since friction forces are the primary input for stress recovery, an inaccurate calculation of the non-linear forced response leads to an incorrect calculation of the dynamic stresses distribution. This is a major limitation for identifying the most critical areas of the blade and, consequently, for calculating its fatigue life.

These considerations highlight the importance of reducing the FEM model by following the procedure proposed in this research.

Chapter 5

Computation of dynamic stresses in presence of friction contacts

The previous chapter focused on a detailed description of the entire procedure for obtaining the input files for the Ansaldo's non-linear tool, which are:

- The reduced mass and stiffness matrices, $[K]_{CB}$ and $[M]_{CB}$.
- Static pre-loads on contact elements.
- Master nodes.

These files are necessary for calculating the non-linear forced response of the reduced system. As mentioned above, the Ansaldo's non-linear tool's output are the non-linear physical displacements of the reduced model, calculated taking into account the effect of friction contacts. However, the Ansaldo's non-linear tool is not able to calculate dynamic stresses because the reduced model is a lumped parameter model, in which the FEM model elements are not preserved. This is a major limitation in the mechanical design cycle of turbine blades, as knowledge of dynamic stresses is essential for predicting the fatigue life of the blades.
To overcome this problem, a procedure was developed during this PhD thesis that allows the Ansaldo's non-linear tool's output in terms of contact forces to be used to calculate the stress state of the blades in ANSYS. The steps of the procedure are shown in Figure 24. Each step will be discussed in detail in this chapter:

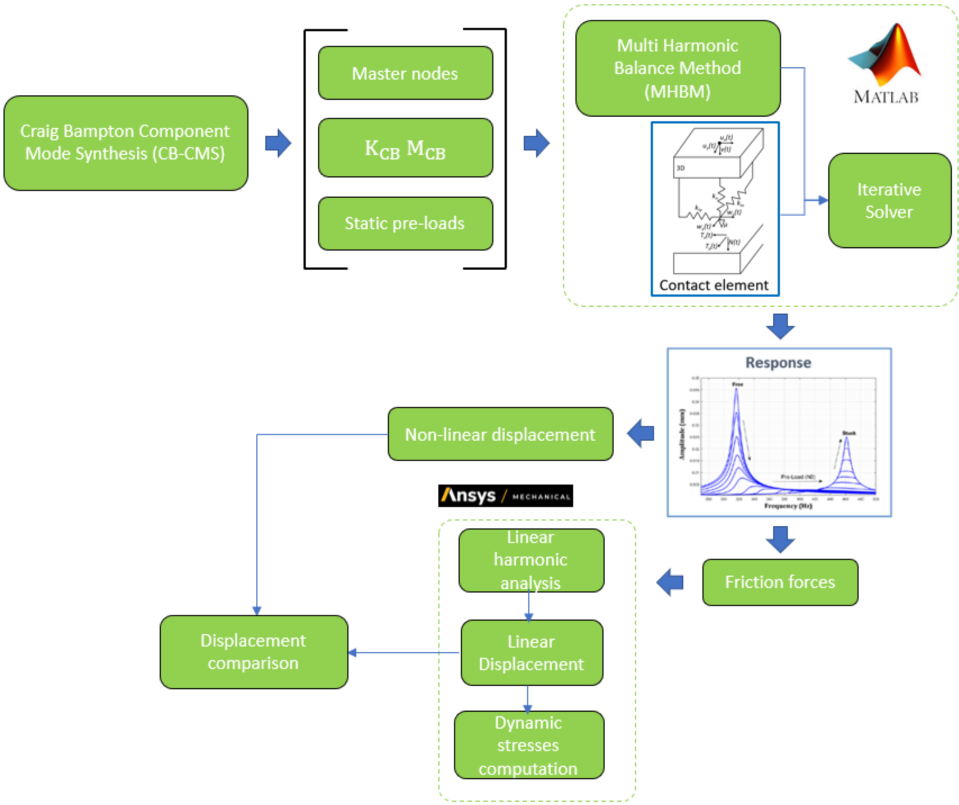

Figure 24: Dynamic stresses computation procedure

The procedure shown in previous figure can be summarized as follows:

- The first step is the Craig-Bampton reduction, that was widely discussed in previous chapter.
- The second step is to calculate the non-linear forced response with the Ansaldo's non-linear tool, which takes the files obtained from the reduction process as input: the reduced mass and stiffness matrices, the static pre-loads and the master nodes.
- the Ansaldo's non-linear tool gives two outputs from the non-linear forced response computation: the dynamic friction forces and the non-linear displacement of the reduced model.
- The previous steps were performed in Matlab, while this step will be performed in ANSYS Mechanical. In order to calculate the stresses in ANSYS, it is necessary to perform a forced response analysis, which, however, does not

take into account the effect of dynamic friction forces as the contacts are linearized during the analysis. In order to also consider friction forces in the forced response calculation, a forced response analysis was performed in which both the excitation and the friction forces calculated with the Ansaldo's non-linear tool were imported as external forces.

- The output of the linear forced response analysis performed in ANSYS are the nodal displacements of the blade. To ensure that the procedure being adopted is consistent and robust, it is necessary to verify that the displacements calculated with the Ansaldo's non-linear tool are the same as those calculated by ANSYS. Obviously, the comparison must be made on the same node. This verification is very important as it allows the calculation of dynamic stresses to be validated. In fact, if the displacements calculated by ANSYS were different from those calculated with the Ansaldo's non-linear tool, then the stress state would also be incorrect.

- Once the consistency between the displacements calculated with ANSYS and those calculated with the Ansaldo's non-linear tool has been verified, the dynamic stress state on the blades can be assessed.

All the steps involved in the procedure shown in Figure 24 will now be discussed in detail. The first step does not require further explanation as it has been described in detail in the previous chapter. In order to describe the procedure, a FEM model with a limited number of contact pairs will be considered. This choice was made to reduce the calculation time of the non-linear forced response. Using a limited number of contact pairs makes the calculation of the natural frequencies of the reduced system and the non-linear response less accurate, but at this point of the discussion, the focus is on showing the steps of the procedure in detail, which is independent of the accuracy of the calculation.
With this in mind, consider the model of the last stage blade of the Ansaldo Energia steam turbine, which has been reduced following the procedure discussed in previous chapter by retaining the following master nodes:

- Force node: the external harmonic excitation is applied to this node.

- Contact nodes: these nodes are those on which the friction forces act. They are located on the contact surfaces of the snubber. For this example, 10 contact pairs were considered, for a total of 20 contact nodes.

- Response nodes: these nodes are usually located on the tip of the blade, where the displacements are greatest. They are used to plot the non-linear response of the reduced model.

For this example, the parameters necessary for the non-linear forced response computation with the Ansaldo's non-linear tool are shown in Table 1:

Non-linear forced response input parameters	
Parameter	Unit
N	/
Nodal diameter	/
k_{tx}	$\frac{N}{mm}$
k_{ty}	$\frac{N}{mm}$
k_n	$\frac{N}{mm}$
μ	/
Start Frequency	Hz
End Frequency	Hz
ζ	/
F_{Rad}	N
F_{Circ}	N
F_{Axial}	N

Table 1: Input parameters for non-linear forced response calculation

In which:

- N is the number of the blades of the bladed disk.
- Nodal diameter is the parameter that defines the phase shift between the displacements of two adjacent sectors.
- k_{tx} is the tangential stiffness of the contact element that couples a single contact pair in X direction. This parameter is defined for the local reference system of the contact.
- k_{ty} is the tangential stiffness of the contact element that couples a single contact pair in Y direction. This parameter is defined for the local reference system of the contact.

- k_n is the normal stiffness of the contact element that couples a single contact pair.
- μ is the friction coefficient. It has been set at the same value defined in the full FEM model.
- The Start Frequency is the starting value of the explored frequency range.
- The End Frequency is the ending value of the explored frequency range.
- ζ is the modal damping. It is defined constant for all mode shapes.
- F_{Rad} is the radial component of the external excitation. This component is defined in a cylindrical reference system, in which the axial component is coincident with the axial direction of the turbine.
- F_{Circ} is the Circumferential component of the external excitation. This component is defined in a cylindrical reference system, in which the axial component is coincident with the axial direction of the turbine.
- F_{Axia} is the axial component of the external excitation. This component is defined in a cylindrical reference system, in which the axial component is coincident with the axial direction of the turbine.

Note: The parameter values cannot be disclosed due to confidentiality agreements with Ansaldo Energia.
Note that the tangential stiffness in X and Y direction is the same. This means that the 3D contact element is isotropic, so from now on the tangential stiffness will be simply called k_t. For this case study the first mode shape, computed for harmonic index 6, will be investigated. The displacement field of the selected mode shape is shown in Figure 25:

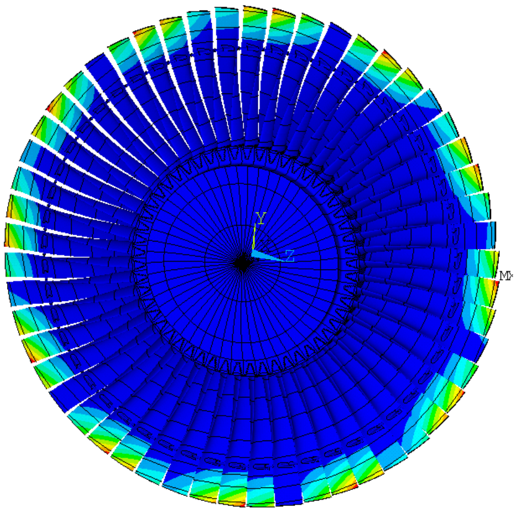

Figure 25: Displacement field of the 1^{st} mode shape computed for harmonic index 6

The analyzed mode shape is a bending mode. Therefore, a significant relative displacement between the snubber contact surfaces is expected, and consequently, a very pronounced damping effect. Before showing the result obtained from the non-linear forced response analysis, it is important to briefly discuss the parameters of the contact element. These parameters are not chosen arbitrarily, but are determined by following the procedure below:

- The first step is to define two arrays: one containing a set of tangential stiffness values and one containing a set of normal stiffness values.
- The second step is to calculate the stiffness matrix of the reduced system under full stick conditions. This is done by extracting submatrices from the stiffness matrix of the reduced system, whose elements correspond to the degrees of freedom of the contact nodes. Once the submatrices have been extracted, the stiffness matrix of the contact element is added to each of them.
- Once the full stick stiffness matrix has been calculated, a modal analysis of the system is performed and the frequency relating to the modal shape of interest is considered. This procedure is performed for all combinations of normal and tangential stiffness values. The output is a matrix containing all the frequencies calculated for each combination of k_t and k_n values.

- The final step consists of plotting all the frequency values contained in the matrix obtained in the previous step in the form of a surface. At this point, the combination of k_t and k_n values that reaches the frequency plateau must be identified.

The previous workflow generates a frequency surface, which is shown in Figure 26:

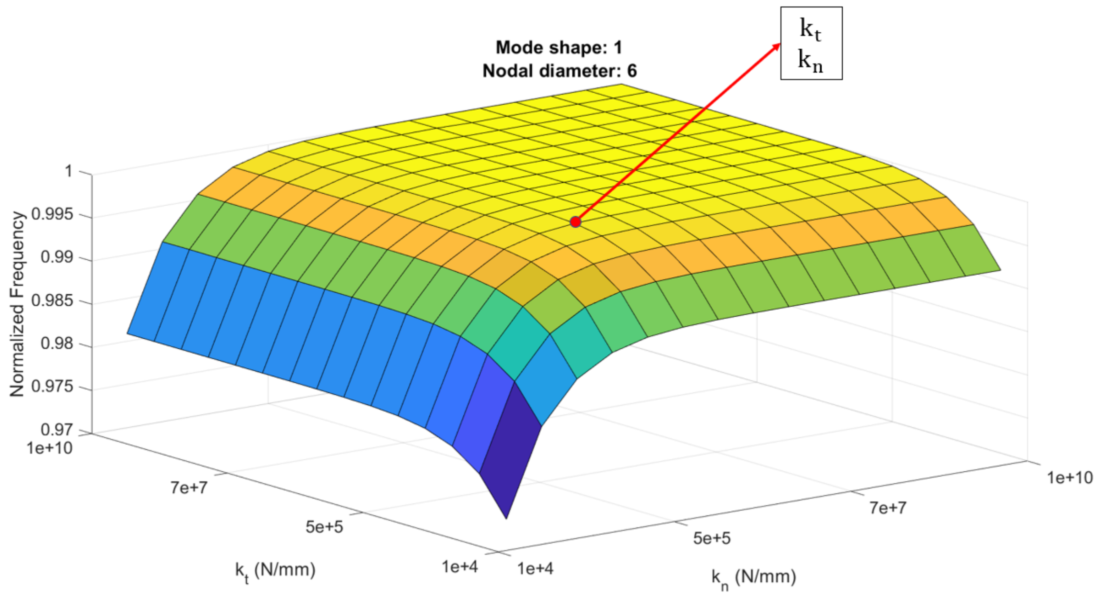

Figure 26: Frequency grid for 1 mode shape and harmonic index 6

Looking at Figure 26, each point on the grid represents the frequency calculated with a specific combination of k_t and k_n. For this specific example, 15 values of k_t and 15 values of k_n were used, so the frequency grid has 225 points. The point highlighted in red in the figure is the combination of contact parameters values at which the frequency plateau was reached; in fact, further increasing the values of k_t and k_n does not result in an increase in frequency. The selected values of k_t and k_n were chosen considering that:

- The values of the contact parameters must be high enough to reach the frequency plateau, but on the plateau it is advisable to consider lower values in order to avoid convergence problems of the non-linear solver, as explained in detail by.

- k_n must be greater than k_t. This is due to the fact that physically, for the same displacement, the normal forces are greater than the tangential forces, so the normal stiffness must take on a higher value.

Just a clarification: the frequency value reached on the plateau must match the frequency calculated with ANSYS on the full FEM model. In this case, the frequency is slightly different because a limited number of contact pairs were used, but using an adequate number of contact pairs will yield the same frequency value. This aspect will be discussed in more detail in the next chapter.
At this point, the entire procedure for obtaining all the input parameters for the Ansaldo's non-linear tool was described. Considering the input parameters shown in Table 1, the non-linear forced response was computed. The result is shown in Figure 27:

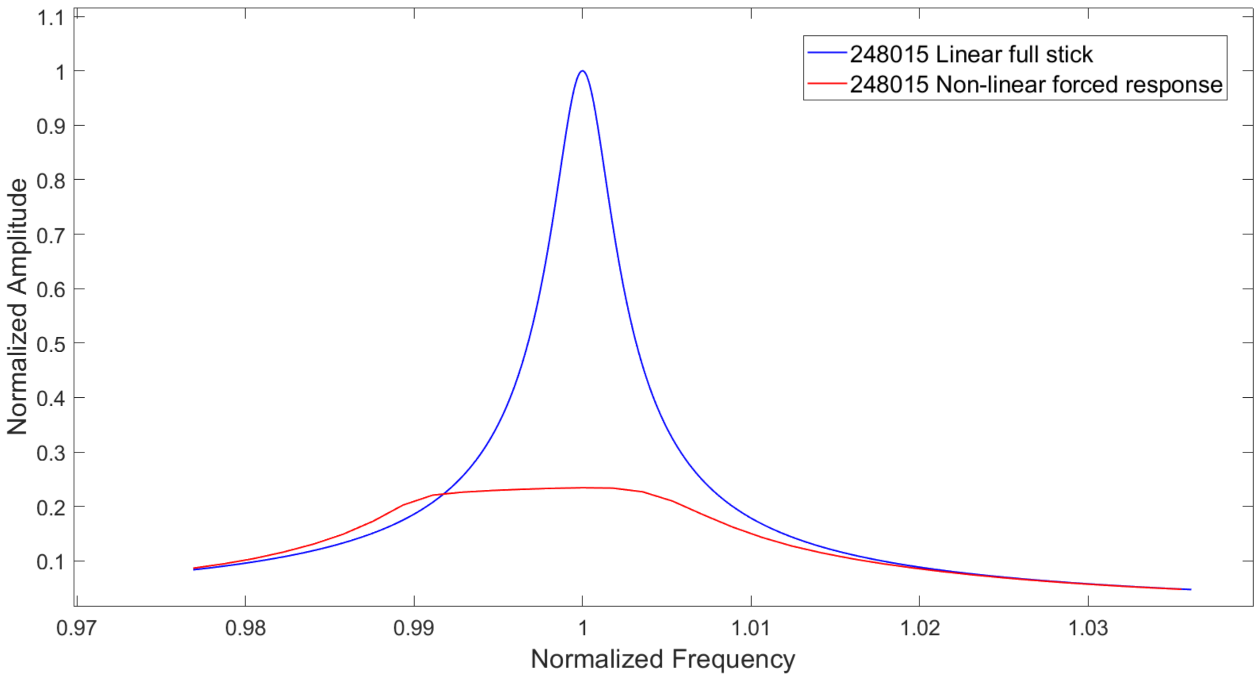

Figure 27: Non-linear forced response computed with the Ansaldo's non-linear tool:circumferential displacement

Note: the physical displacement is represented in a cylindrical reference system that has the axial coordinate coincident with the turbine axis. Figure 27 shows the result of the non-linear forced response calculated with the Ansaldo's non-linear tool. To highlight the damping effect of friction forces, the linear full-stick response is

also shown. The plot in Figure 27 is the non-linear displacement calculated by the Ansaldo's non-linear tool on node 248015, which is one of the two response nodes retained in the reduced model. What is immediately apparent is that at resonance peak, where the displacements are maximum, the friction forces acting on the contact surfaces of the snubber come into play, dissipating part of the kinetic energy and thus reducing the vibration amplitudes. The non-linear forced response computation yields the system's non-linear displacements and the friction forces acting on the contact nodes. For stress recovery, additional steps are required because the reduced model does not contain the elements of the FEM model; consequently, it is not possible to directly calculate the dynamic stresses.
The workflow for stress recovery is structured as follows:

- Extract the non-linear friction forces derived from the non-linear forced response calculation performed on the reduced model.
- Generate a series of text files, one for each frequency, each containing the APDL commands necessary to apply the friction forces and the external excitation to the nodes of the FEM model.
- A linear harmonic analysis is performed on the FEM model within the same frequency range explored in the non-linear forced response analysis. For each frequency, the text file generated in the previous step is imported. Importing the text file allows the friction forces to be applied to the contact nodes and the external excitation to the force node.
- The displacements obtained from the linear harmonic analysis in ANSYS are compared with the displacements of the reduced model. As mentioned earlier, two response nodes have been retained in the reduced model. The displacement of the reduced model is evaluated at one of these two nodes; therefore, the same node is obviously used for the comparison. This step allows for an assessment of the consistency between the two models.
- The dynamic stresses at the frequency of interest are evaluated. Typically, the most critical case, the resonance frequency, is considered.

The stress recovery workflow just discussed allows you to calculate the distribution of dynamic stresses across the entire blade geometry. However, this workflow remains valid only if the material behavior is assumed to be linearly elastic. This is because

stresses within ANSYS are calculated using a material matrix, which defines a direct relationship between stresses and strains. If this assumption no longer holds, more complex stress recovery models must be used.
The key step of the workflow involves applying non-linear friction forces to the contact nodes of the FEM model. This step accounts for the non-linear behavior of frictional contacts even when performing a linear harmonic analysis, since the friction forces imported as external forces are derived from a non-linear calculation. The information regarding the non-linear behavior is therefore contained within the friction forces. The workflow is now applied to the case study in question.
Figure 28 shows an example of output in terms of friction forces computed with the non-linear forced response. For simplicity of representation, the example shown refers to a single node, 251363, and to the first frequency of the explored frequency range, but the reasoning is extended to all contact nodes and to all frequencies:

Node	Real part	Imaginary part	
251363	$\Re(\bar{T}_x)$	$\Im(\bar{T}_x)$	X component of the friction force
251363	$\Re(\bar{T}_y)$	$\Im(\bar{T}_y)$	Y component of the friction force
251363	$\Re(\bar{N})$	$\Im(\bar{N})$	Z component of the friction force

Figure 28: the Ansaldo's non-linear tool friction forces output

The first column shows the node number, while the second and third columns show the real and imaginary parts of the contact forces, respectively. As can be seen, the same node is repeated three times along the rows.
The output shown in Figure 28 is given as input to a Matlab routine, which is able to generate text files for each frequency value, containing APDL commands to import the contact forces calculated by the Ansaldo's non-linear tool as external forces in ANSYS, on the contact nodes. Figure 29 shows the APDL commands for importing the contact forces calculated by the Ansaldo's non-linear tool as external forces in ANSYS. Again, the example shown refers to node 251363 and the first frequency of the explored frequency range, but the reasoning can be extended to all contact nodes and to all frequencies:

APDL force command	Node	Force label	Real part	Imaginary part
f	251363	f_x	$\Re(\bar{T}_x)$	$\Im(\bar{T}_x)$
f	251363	f_y	$\Re(\bar{T}_y)$	$\Im(\bar{T}_y)$
f	251363	f_z	$\Re(\bar{N})$	$\Im(\bar{N})$

Figure 29: ANSYS APDL commands for harmonic analysis

For the symbols used in Figure 28 and Figure 29, refer to Chapter 3.
The APDL commands shown in Figure 32, when executed for each contact node, cause the friction forces calculated with the Ansaldo's non-linear tool to be imported as external forces into ANSYS. The result of this import is shown in Figure 30:

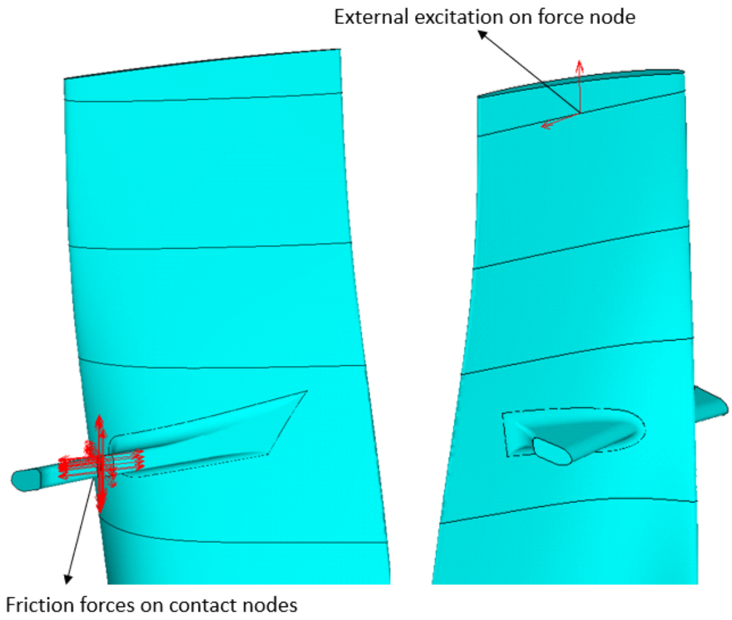

Figure 30: Import of friction forces and external excitation on the full FEM model

Now that the procedure for extracting the friction forces calculated by the Ansaldo's non-linear tool and importing them as external forces into ANSYS is clear, the result obtained from the linear harmonic analysis performed in ANSYS is shown. The forced response analysis performed on the full FEM model obviously covers the same frequency range explored in the Ansaldo's non-linear tool, and for each frequency the relative friction forces on the contact nodes are imported, as shown in Figure 30. The external exciting force is independent of frequency, so for each frequency the force is imported from the same text file. The result of the linear harmonic analysis performed in ANSYS mechanical is shown in Figure 31:

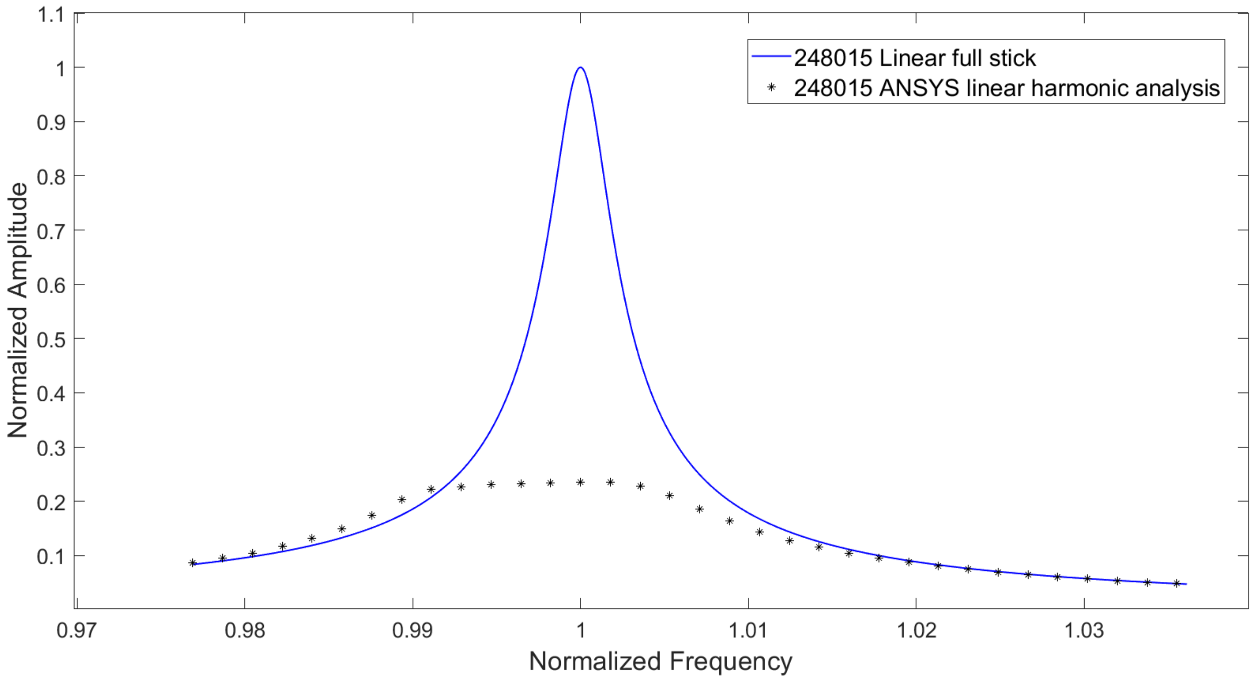

Figure 31: Linear forced response computed in ANSYS mechanical:circumferential displacement

As can be seen, Figure 31 shows the result obtained from the linear forced response analysis performed in ANSYS Mechanical. To verify that the procedure described so far is consistent, it is necessary to compare the displacements calculated with the Ansaldo's non-linear tool and those calculated with ANSYS for the same node. This check is very important because if the displacements calculated by ANSYS were different, then the stress calculation would not be consistent. Figure 32 shows both the displacements calculated by ANSYS and those calculated by the Ansaldo's non-linear tool:

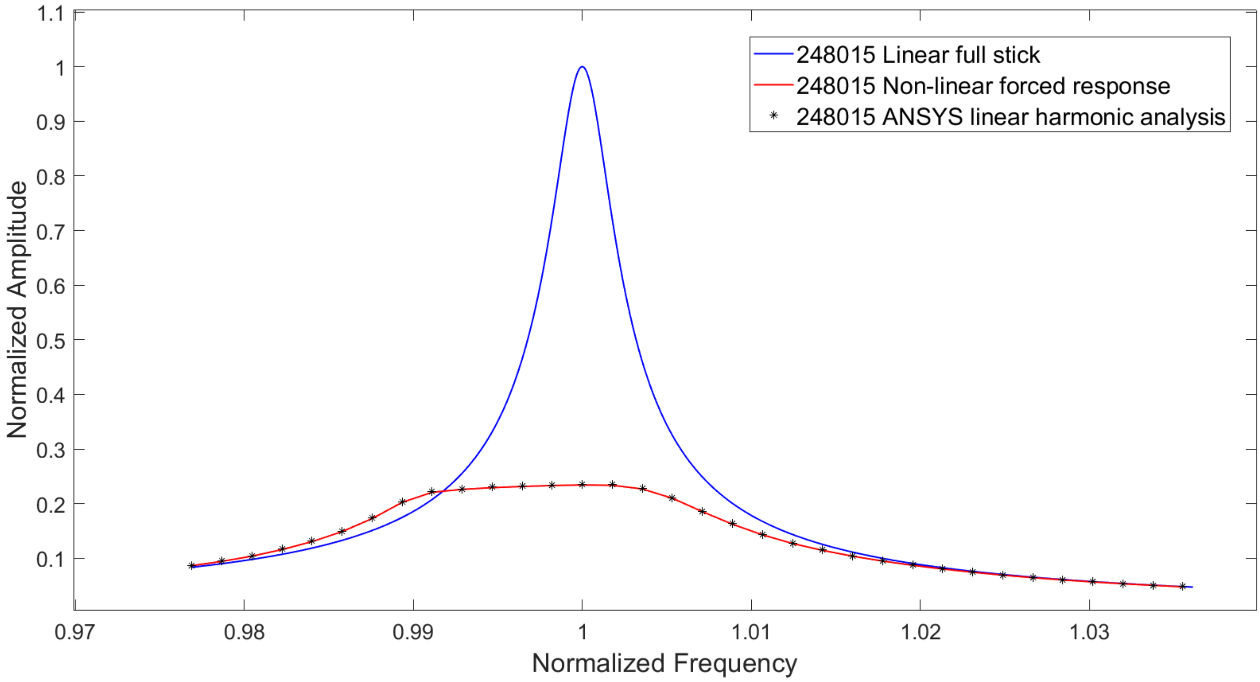

Figure 32: Comparison between the displacements computed with the Ansaldo's non-linear tool and the displacements computed with ANSYS:circumferential displacement

As can be seen in Figure 32, the displacements calculated with the Ansaldo's non-linear tool and those calculated with ANSYS are practically identical, with the error calculated on the maximum displacement being less than 0.5%, which is acceptable. This ensure the consistency between the reduced order model and the full FEM model.

At this point, it is possible to proceed with the evaluation of the stresses, which have already been calculated by ANSYS during the linear forced response analysis. Suppose we want to evaluate the worst-case scenario, the condition under which the maximum amplitude of vibration occurs. Figure 33 shows the dynamic stress field calculated for the above-mentioned frequency:

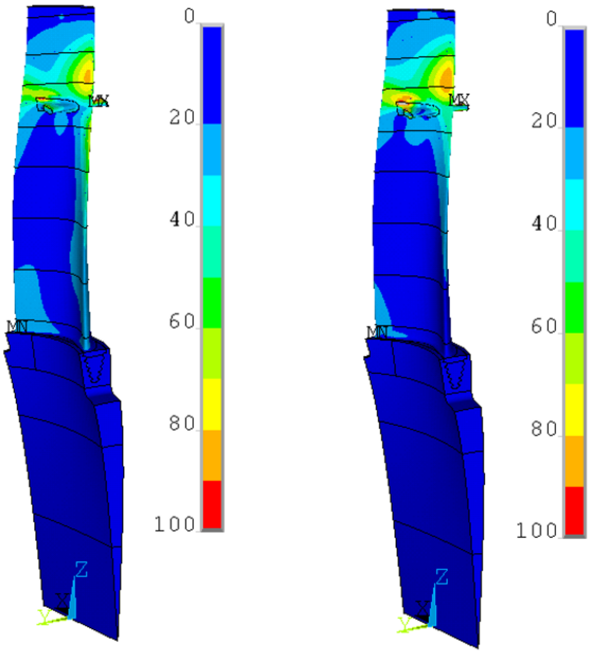

(a) Real component of stress distribution

(b) Imaginary component of stress distribution

Figure 33: Dynamic stresses computed considering the effect of friction contacts

Note: The stress scale shown in Figure 33 is fictitious in order to comply with confidentiality agreements with Ansaldo Energia.
What can be observed in Figure 33 is that the stresses are concentrated around the snubber. This can be explained by considering that when the blades come into contact, the snubber becomes a constraint and the tip displacements are very high. The stress values are not very high, due to the fact that in this example a small external forcing value was used compared to the forces that actually act on the blades.
To conclude this chapter, it is important to make a few considerations. First of all, it is important to emphasise that the entire procedure discussed so far has been carried out considering only the first harmonic of the non-linear displacement and, consequently, of the friction forces. In most cases, using only the first harmonic allows for a very good approximation of the non-linear dynamic response. However, this is not true in cases where, for example, there is intermittent contact, in which a greater number of harmonics is required.
Another aspect to emphasise is the number of contact pairs used. For this example, 10 contact pairs were considered to speed up the calculations. In real applications, it may be necessary to use more contact pairs in order to make the simulation more

accurate. It is important to use a sufficient number of contact pairs to make the calculation accurate, but not too many, in order to find the best compromise between accuracy and calculation time. This aspect will be discussed in the next chapter. The last point I want to discuss concerns the external force. In this example, an external force was applied to a single node. This situation does not reflect reality, in which the aerodynamic force acts on the entire surface of the blade. The appendix B discusses in detail the possibility of using a force vector obtained by reducing the pressure field derived from CFD calculations. This aspect represents an opportunity for future software improvement, which would lead to a further increase in the accuracy of calculating the non-linear forced response of the reduced-order model, and consequently of the dynamic stresses.

Chapter 6

Case study: critical resonance for ventilation conditions

The previous chapter discussed in detail the entire procedure for calculating dynamic stresses on turbine blades, taking into account the effect of friction contacts. This chapter will show an example of the application of the procedure explained in Chapter 5, considering a possible resonance of the Ansaldo Energia steam turbine last stage blades, caused by ventilation conditions. The introductory section discussed the future application of the steam turbine produced by Ansaldo Energia. In the future, this turbine will be powered by the DEMO nuclear fusion reactor. Due to plant requirements, the steam flow will not be continuous, so the turbine will operate under transient conditions in which the steam flow rate will be extremely low. These conditions, as mentioned initially, are known as ventilation conditions, and cause:

- Significant increase in temperature in the blade. This happens because, under ventilation conditions, the blades of the last stage work in compressor mode, centrifuging the residual steam and thus undergoing an increase in temperature due to friction with the fluid.
- Rotating stall cells.
- Asynchronous external excitation.

The combination of increased temperature on the blade and asynchronous excitations, with frequencies that are not multiples of the turbine rotational velocity, causes the turbine to operate outside its design conditions, resulting in unexpected resonances. This chapter will show an example of a possible resonance condition caused by ventilation conditions. To calculate the dynamic stresses on the blade and thus predict its fatigue life, the procedure explained in detail in the previous chapter will be applied. Before showing the results obtained, it is very important to make a small digression on the choice of the number of contact pairs to be condensed in the reduced model.

6.1 Choice of the number of contact pairs: a sensitivity analysis

In the previous chapter, 10 contact pairs were used to calculate the non-linear forced response with the Ansaldo's non-linear tool. This choice was made to speed up the calculation, as the purpose of the previous chapter was not to show a realistic calculation but to illustrate a procedure. However, when approaching a realistic calculation, it is important to choose the optimal number of contact pairs, which has two advantages:

- It makes the calculation more accurate, as increasing the number of contact pairs brings the natural frequencies of the reduced model closer and closer to those of the full FEM model.
- It optimizes calculation times, as increasing the number of contact pairs beyond a certain limit increases the computational effort without increasing the accuracy of the results. This is valid if the contact pairs are well distributed on the contact surfaces.

To choose the optimal number of contact pairs, a sensitivity analysis was performed, varying the number of contact pairs and comparing the natural frequencies calculated on the reduced model with those calculated on the full FEM model in ANSYS. The sensitivity analysis was performed considering the following cases:

- Case 1: 10 contact pairs are condensed in the reduced model.
- Case 2: 30 contact pairs are condensed in the reduced model.

- Case 3: 50 contact pairs are condensed in the reduced model.
- Case 4: 70 contact pairs are condensed in the reduced model.

Let's consider Case 1, the reduction process was performed as explained in detail in chapter 4. For this case, the following master nodes were condensed in the reduced model:

- Force node: node on which the external excitation is applied.
- Response nodes: nodes on which the non-linear response calculated with the Ansaldo's non-linear tool is plotted.
- Contact nodes: nodes on which friction forces act. In this case, there are 20 contact nodes, as 10 contact pairs have been condensed.

Figure 34 shows the interference diagram calculated for the reduced model of Case 1 and that calculated for the full FEM model overlapped. The interference diagram shows the natural frequencies of a bladed disk as a function of the harmonic index. For this sensitivity analysis, the first five modal families, computed for the first six harmonic indexes are shown. The interference diagram generated for Case 1 is shown in Figure 34

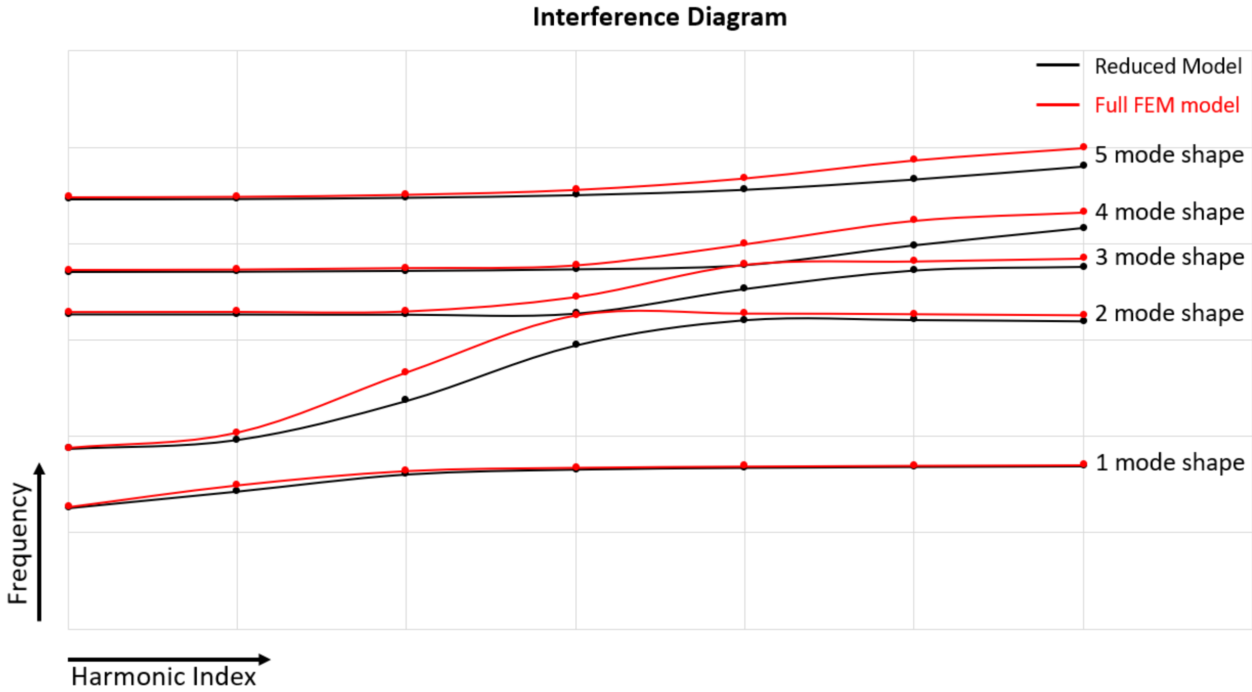

Figure 34: Interference diagram calculated for 10 contact pairs and for ANSYS full FEM model overlapped

In Figure 34, and in the next figures, the lines marked in black refer to the natural frequencies calculated on the reduced model, while those marked in red are the reference frequencies, calculated on the full FEM model with ANSYS mechanical. As can be seen from Figure 34, using 10 contact pairs, some natural frequencies are calculated correctly, while others differ from those calculated on the full FEM model. For example, the natural frequency of the second modal family calculated for harmonic index 3 and for harmonic index 2 are very different from the reference frequencies, with an error of about 10 %. This indicates that 10 contact pairs are not sufficient to generate a reduced model that accurately describes the dynamic behavior of the full model.

Let's now consider the interference diagram generated for Case 2, which is shown in Figure 35:

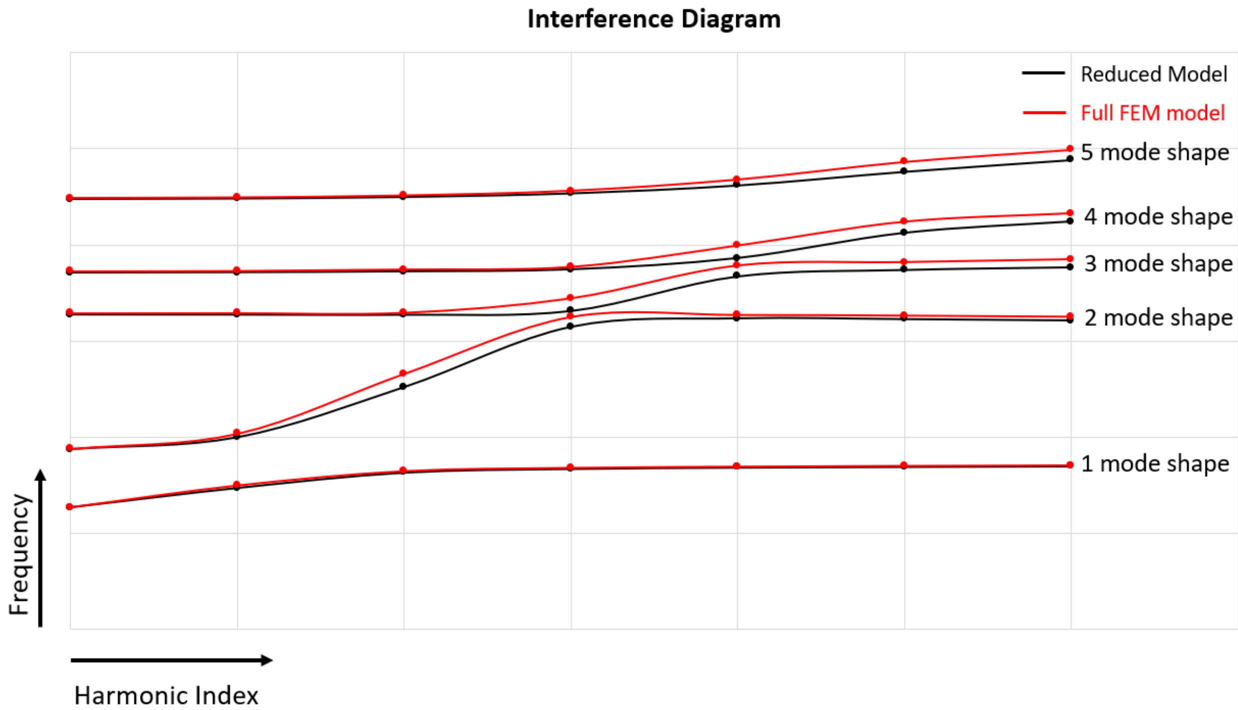

Figure 35: Interference diagram calculated for 30 contact pairs and for ANSYS full FEM model overlapped

In this second case, it can be seen that all the natural frequencies of the reduced system are very close to those calculated on the full model. In the previous case, the frequency calculated for the second modal family and the third and second harmonic indices had an error of 10 % compared to the reference value, while in this case the error was reduced around to 4 %.

Now consider Case 3 and Case 4. Figure 36 shows the interference diagram generated for Case 3:

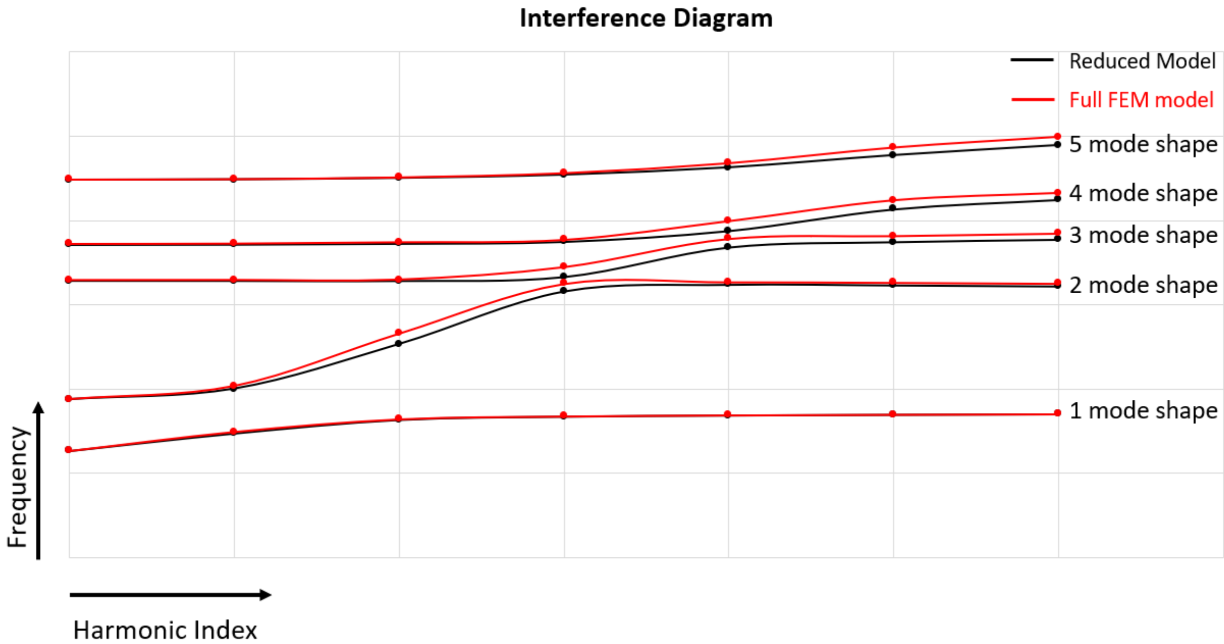

Figure 36: Interference diagram calculated for 50 contact pairs and for ANSYS full FEM model overlapped

As can be seen from Figure 36, even in this case, the natural frequencies calculated on the reduced model are very close to those of the full model, and in particular, the error on the second mode and third and second harmonic indices remains around 4 %.

Let's now analyze the last case. Figure 37 shows the interference diagram generated for the Case 4:

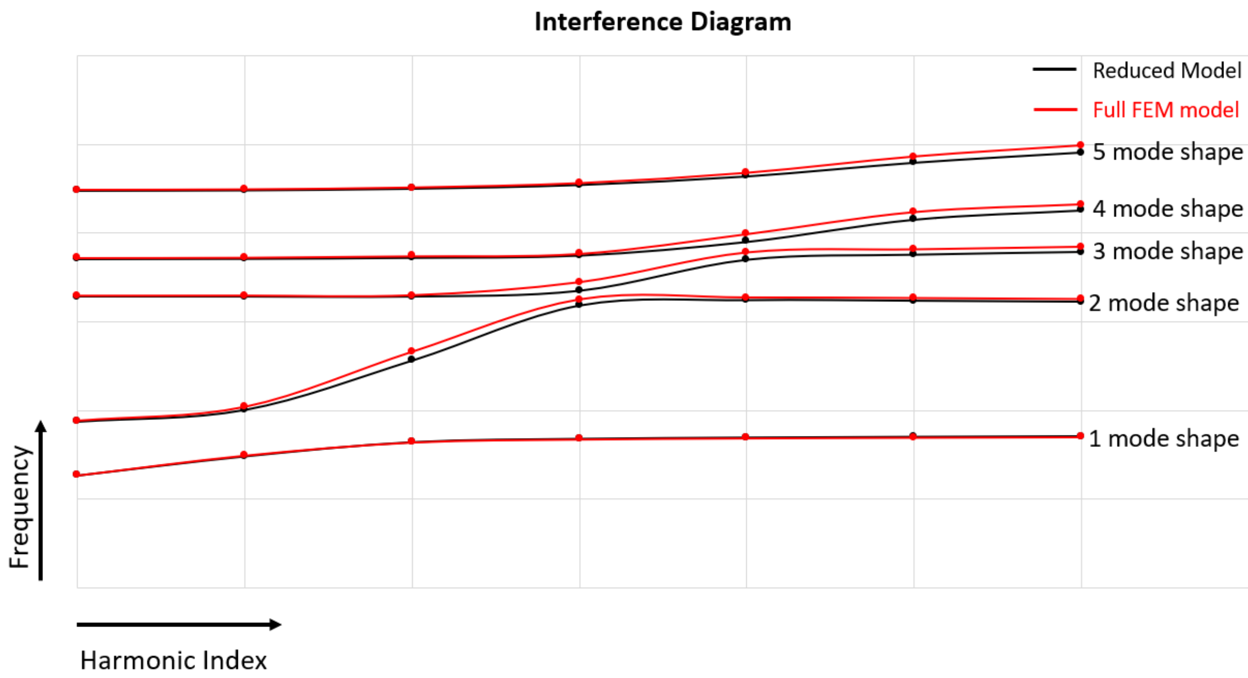

Figure 37: Interference diagram calculated for 70 contact pairs and for ANSYS full FEM model overlapped

Looking at Figure 37, what immediately stands out is that the variation in natural frequencies is minimal, and in particular the error for the frequency calculated for the second mode and harmonic indices 2 and 3 is about 3 %, compared to 4 % in the previous case.
The results obtained for the four cases analyzed are summarized in Table 2, which shows the relative errors of the two modes that exhibit the greatest variation as function of the number of contact pairs condensed in the reduced order model.

Mode shape	Harmonic index	Contact pairs	% relative error
2	$2-3$	10	$\approx 10\%$
2	$2-3$	30	$\approx 4\ \%$
2	$2-3$	50	$\approx 4\ \%$
2	$2-3$	70	$\approx 3\ \%$

Table 2: Relative percentage error as function of the contact pairs number

Looking at the results obtained for the four cases analyzed, it can be seen that condensing more than 30 contact pairs in the reduced model results in a minimal

change in terms of relative percentage error, as evaluated against the natural frequencies calculated with ANSYS. This means that increasing the number of contact pairs beyond 30 increases the computational cost without providing any benefits in terms of the reduced model's accuracy.
In addition to the variation in the relative percentage error, it is also interesting to observe the variation in the frequencies associated with the two mode shapes shown in Table 2 as the number of contact pairs changes. Figure 38 shows the normalized frequencies as function of the contact pairs number:

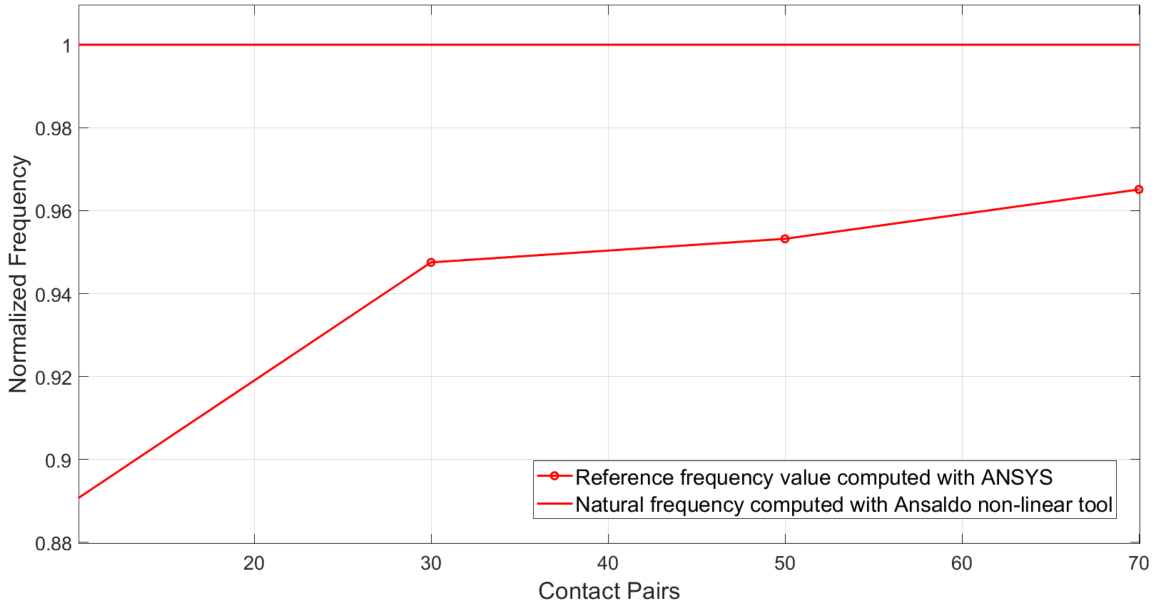

(a) Frequency trend for the second mode shape and harmonic index 2

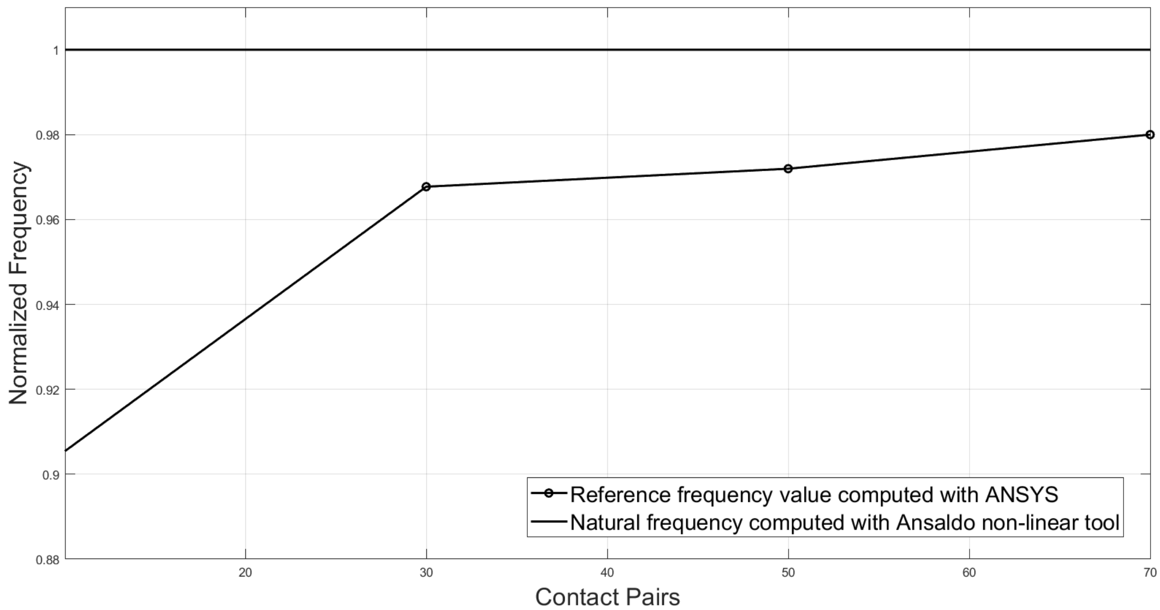

(b) Frequency trend for the second mode shape and harmonic index 3

Figure 38: Frequency trend

In Figure 38 the constant value 1 represents the normalized frequency computed with ANSYS on the full FEM model, that is here used as reference value. Looking at Figure 38, it is clear that the greatest change in frequency occurs when the number of contact pairs increases from 10 to 30. Increasing the number of contact pairs further

results in a negligible change in frequency. In conclusion, it can be said that in this case, condensing more than 30 contact pairs into the reduced model increases the computational cost without improving the accuracy of the calculation.
The last point that i want to touch is about the distribution of the contact nodes. In fact, what has been said so far remains valid if the contact pairs are distributed over the contact area. If the contact nodes were all concentrated in a single area, it would not be possible to correctly simulate the physics of the system. The distribution of the 30 contact pairs is shown in Figure 39:

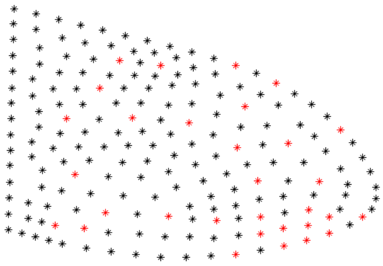

(a) Contact nodes on snubber suction side contact surface

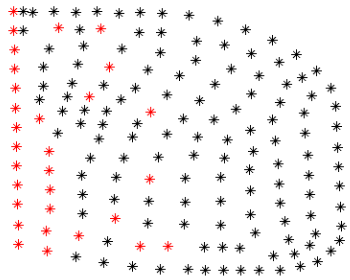

(b) Contact nodes on snubber pressure side contact surface

Figure 39: Contact pairs

Considering the previous figure:

- The nodes plotted with the red '*' marker represent the chosen contact nodes.
- The nodes plotted with the black '*' marker represent non-contact nodes.

What can be concluded from observing Figure 39 is that the contact pairs are distributed over the contact area, so the reduced model can well simulate the physics of the full model. The next section will show the result of the non-linear calculation performed with the Ansaldo's non-linear tool.

6.2 Non-linear forced response computation

Considering what was said in the previous section, the calculation of the non-linear forced response was performed by condensing 30 contact pairs into the reduced model. As a case study, consider the first mode shape calculated for harmonic index 3. If we consider the Campbell diagram for an external excitation that excites modes with harmonic index 3, the exciting pulsation can be expressed as a multiple of the turbine rotation speed. Considering that in a real case the turbine rotation speed is not exactly 3000 *rpm*, but there is a certain tolerance, the Campbell diagram for this example can be plotted as shown in Figure 40:

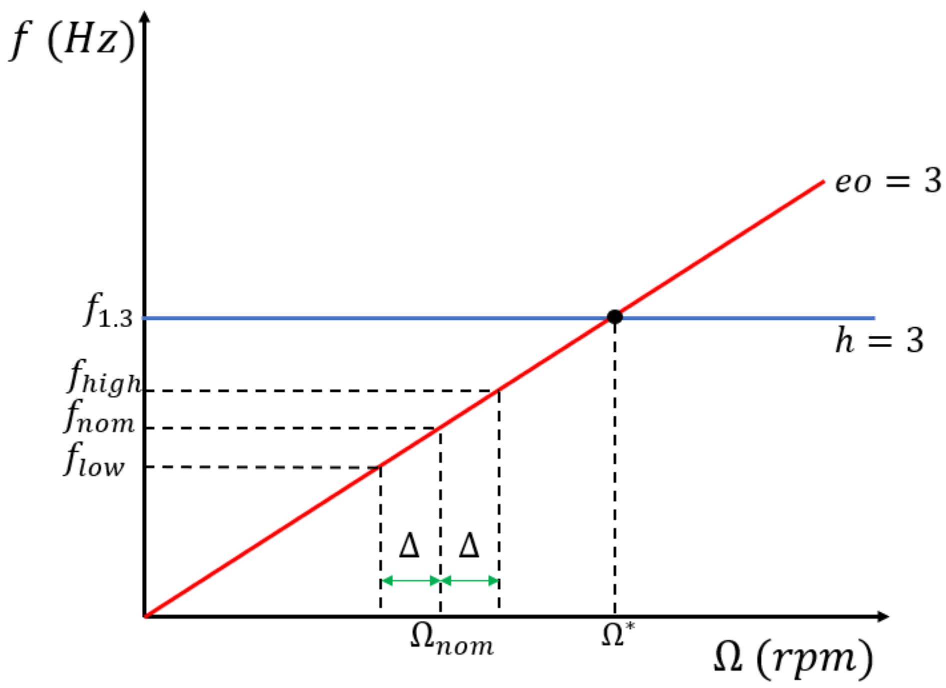

Figure 40: Campbell diagram for first modal family and engine order 3

In which:

- eo is the external excitation engine order.
- Δ is the tolerance on the rotation speed.
- f is the exciting frequency.
- Ω_n is the turbine nominal rotation speed.
- Ω^* is the rotation speed corresponding to the intersection between the exciting frequency and the natural frequency of the system.
- h is the harmonic index.

- $f_{1.3}$ is the natural frequency for the first mode shape and harmonic index 3.
- f_{nom} is the nominal exciting frequency.
- f_{high} is the upper limit of the exciting frequency range.
- f_{low} is the lower limit of the exciting frequency range.
- The red line is the exciting frequency versus the turbine rotation speed.

The Campbell diagram shown in previous figure represents the exciting frequency versus the rotational velocity of the turbine.
Considering that:

- The external excitation has an engine order $eo = 3$.
- The nominal rotation speed is $\Omega_n = 3000\ rpm$
- The turbine rotation speed is not a single value, but is defined within an operating range, defined by a tolerance of about 5 % on the nominal rotation speed.

The exciting frequency range can be expressed as follows:

$$\begin{aligned} f_{nom} &= eo\frac{\Omega}{60} = 150\ Hz \\ f_{low} &= eo(\frac{\Omega+\Delta}{60}) = 157.5\ Hz \\ f_{high} &= eo(\frac{\Omega-\Delta}{60}) = 142.5\ Hz \end{aligned} \tag{25}$$

Taking into account the above, the nominal excitation frequency, calculated for $\Omega = 3000\ rpm$, is $150\ Hz$, but since the rotation speed is defined within a range, the excitation frequency may be slightly lower or higher than this value. During the turbine design phase, this aspect is evaluated and the bladed disk is designed so that the natural frequencies of the system do not fall within the frequency range of the external exciting frequency. This can be seen in Figure 40, in fact the rotation speed corresponding to the intersection between the exciting frequency and the natural frequency,Ω^*, is out of the turbine operating range.
However, as mentioned above, if the turbine operates in ventilated conditions, the

blades of the last stage are subject to a significant increase in temperature and external asynchronous excitation. In these conditions:

- The natural frequencies of the bladed disk decrease.
- The frequency of the external excitation is not a multiple of the turbine rotation speed.

Let us assume that we ignore the temperature increase on the blades and consider only an asynchronous external excitation due to rotating stall cells caused by steam flow separation.
This can lead to a resonance condition, so it is important to be able to predict the stresses on the blades, taking into account friction contacts.
The Campbell diagram referred to the asynchronous excitation is shown in Figure 41:

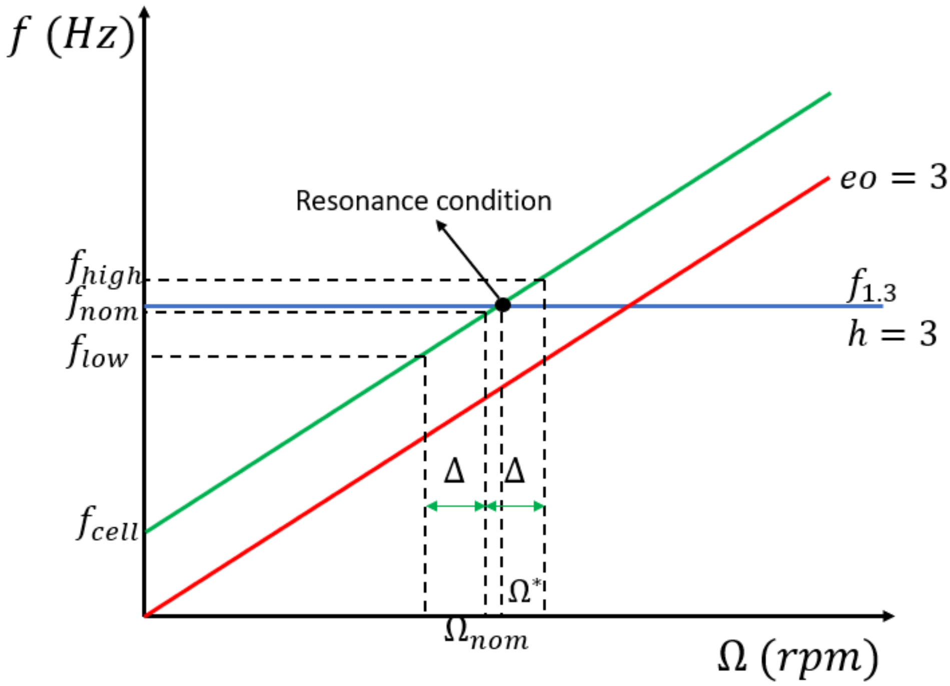

Figure 41: Campbell diagram with asynchronous excitation

In which:

- *eo* is the external excitation engine order.

- Δ is the tolerance on the rotation speed.
- f is the exciting frequency.
- Ω_n is the turbine nominal rotation speed.
- Ω^* is the rotation speed corresponding to the intersection between the exciting frequency and the natural frequency of the system.
- h is the harmonic index.
- $f_{1.3}$ is the natural frequency for the first mode shape and harmonic index 3.
- f_{nom} is the nominal exciting frequency.
- f_{high} is the upper limit of the exciting frequency range.
- f_{low} is the lower limit of the exciting frequency range.
- The red line is the exciting frequency versus the turbine rotation speed for standard conditions.
- The green line is the exciting frequency versus the turbine rotation speed with rotating stall cells external excitation.

If the asynchronous excitation is caused by rotating stall cells, the excitation frequency can no longer be calculated as a multiple of the rotational speed, but is defined by the following equation, as discussed by [44]:

$$f = eoN_{sc}\left(\frac{\Omega}{60} \pm f_{cell}\right) \tag{26}$$

In which:

- f is the exciting frequency.
- eo is the external excitation engine order.
- N_{sc} is the number of rotating stall cells.
- Ω is the rotation speed.
- f_{cell} is the frequency of the rotating stall cells.

Consider a simple case where there is a single stall cell rotating in the opposite direction to the turbine rotation speed, with a cell frequency of 4 Hz. These values are reasonable, as reported by [44], for these particular conditions. With the above in mind, the range of exciting frequencies for the ventilation conditions can be calculated as follows:

$$\begin{aligned} f_{nom} &= eoN_{sc}\left(\frac{\Omega}{60} + f_{cell}\right) = 162\ Hz \\ f_{low} &= eoN_{sc}\left(\frac{\Omega-\Delta}{60} + f_{cell}\right) = 154.5\ Hz \\ f_{high} &= eoN_{sc}\left(\frac{\Omega+\Delta}{60} + f_{cell}\right) = 169.5\ Hz \end{aligned} \tag{27}$$

Looking at Equation 27 and Figure 41, what immediately stands out is that the natural frequency associated with the first modal shape and harmonic index 3 falls within the range of exciting frequencies, in fact Ω^* falls within the turbine operating range. This can lead to unexpected resonance, so it is necessary to be able to calculate the dynamic stresses on the blade in order to predict its fatigue life.
The first mode shape computed for harmonic index 3 is shown in Figure 42:

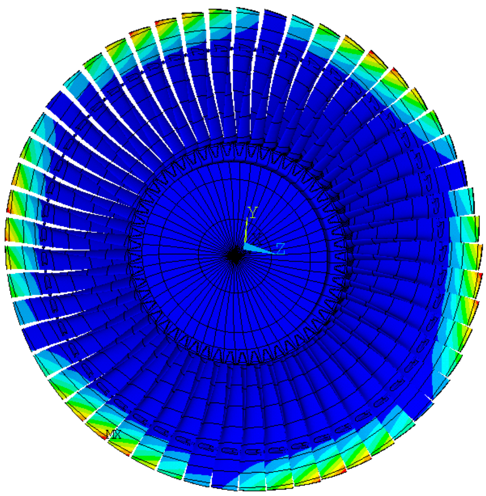

Figure 42: 1 mode shape for harmonic index 3

The parameters shown in Table 3 were used to calculate the non-linear forced response in the Ansaldo's non-linear tool:

Non-linear forced response input parameters	
Parameter	Unit
N	/
Nodal diameter	/
k_{tx}	$\frac{N}{mm}$
k_{ty}	$\frac{N}{mm}$
k_n	$\frac{N}{mm}$
μ	/
Start Frequency	Hz
End Frequency	Hz
ζ	/
F_{Rad}	N
F_{Circ}	N
F_{Axial}	N

Table 3: Input parameters for the case study non-linear forced response calculation

Note: The parameter values cannot be disclosed due to confidentiality agreements with Ansaldo Energia.
The result obtained from the non-linear forced response performed with the Ansaldo's non-linear tool is shown in Figure 43.
Note: the physical displacement is represented in a cylindrical reference system that has the axial coordinate coincident with the turbine axis.

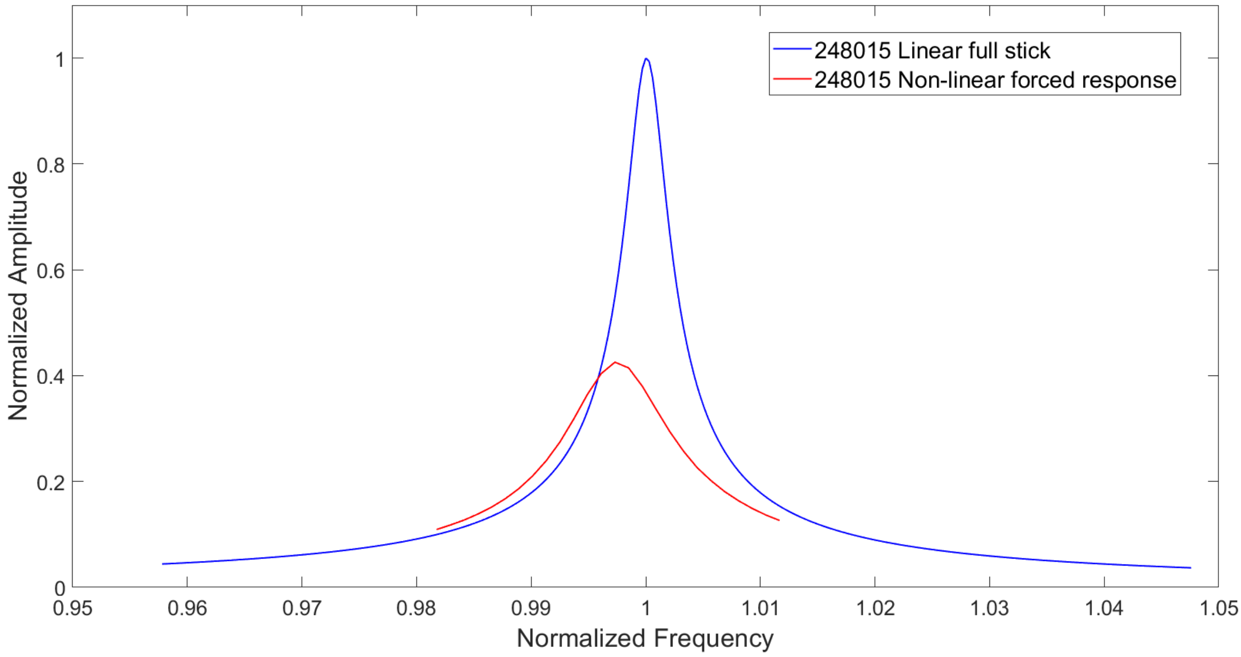

Figure 43: Non-linear forced response computed for the first mode shape and harmonic index 3: axial displacement

Once the non-linear response of the reduced system has been calculated, the final step is to extract the contact forces and perform a linear forced response analysis in ANSYS, as discussed in detail in Chapter 5.

6.3 Dynamic stresses computation

This section focuses on the calculation of dynamic stresses. As explained in Chapter 5, before evaluating the stresses on the blade, it is important to compare the displacement calculated with the Ansaldo's non-linear tool with the displacement calculated with ANSYS, in order to ensure the consistency between the reduced order model and the full FEM model. Figure 43 shows the displacements calculated with ANSYS and those calculated with the Ansaldo's non-linear tool:

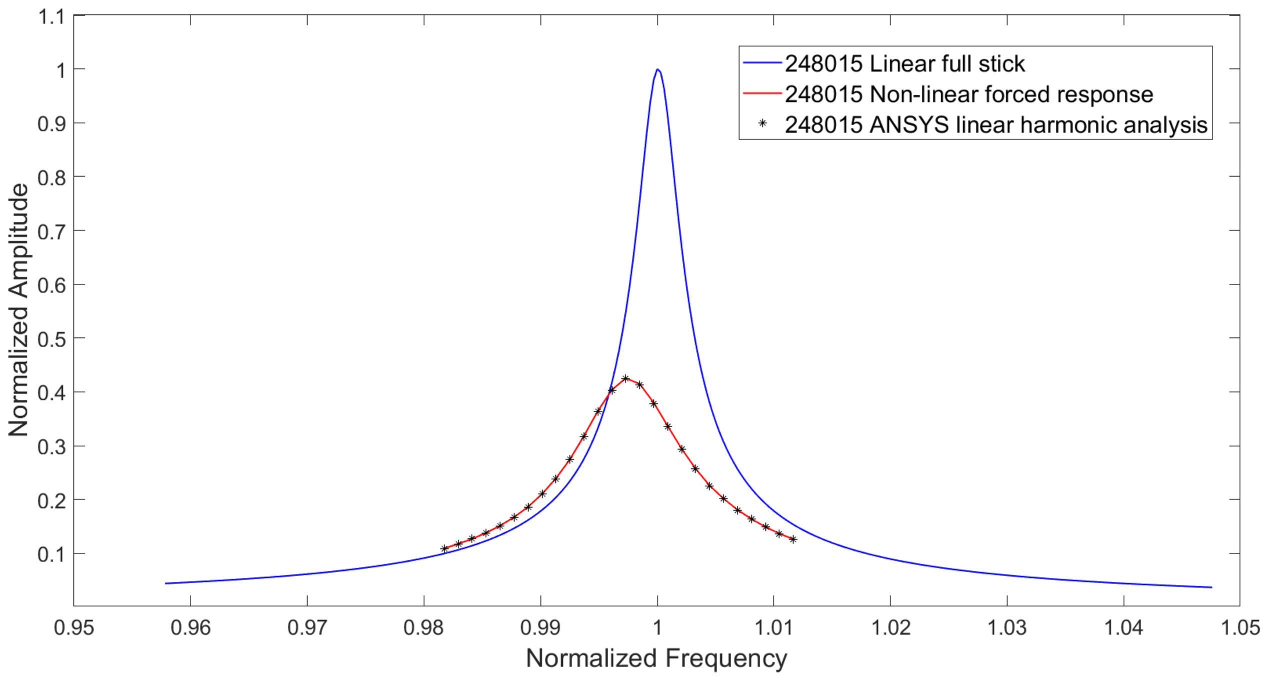

Figure 44: Comparison between the displacements computed with the Ansaldo's non-linear tool and those computed with ANSYS

As can be seen in Figure 44, the displacements calculated with ANSYS and the Ansaldo's non-linear tool overlap, so it is possible to proceed with the stress calculation for the most critical condition, where the maximum displacement occurs. The distribution of dynamic stresses in resonance condition is shown in Figure 45:

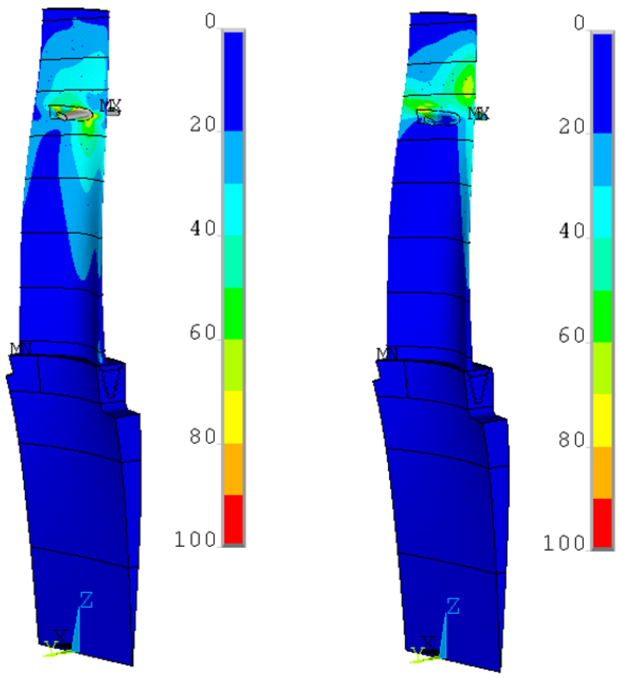

(a) Real component of the dynamic stresses

(b) Imaginary component of the dynamic stresses

Figure 45: Dynamic stresses

The results presented in this chapter demonstrate that the stress-recovery procedure developed during this research project is a robust and reliable tool for calculating dynamic stresses on turbine blades in the presence of frictional contacts, while reducing computational cost.

As previously emphasized in Chapter 4, the convergence of the non-linear forced response calculation is strictly dependent on the input files, in particular on the static pre-loads on the contact elements. Consequently, it is very important to follow the steps of the entire procedure precisely and, above all, to always take the following guidelines into account:

- Static pre-loads must be calculated in a reference system that takes into account the geometry of the blade, thus avoiding software convergence problems.
- It is important to evaluate the number of contact pairs to be condensed in the reduced model in order to optimize calculation times.
- Before performing the forced response calculation with the Ansaldo's non-linear tool, it is important to evaluate the distribution of contact pairs in order

to correctly simulate the physics of the system. If the selected contact pairs are not well distributed in the contact area, it is advisable to increase the number of contact pairs to achieve greater calculation accuracy.

With the above guidelines in mind, the Ansaldo's non-linear tool is a valuable and robust tool that Ansaldo Energia can adopt during the mechanical design cycle of turbine blades, improving the accuracy of the fatigue life prediction of the component.

Chapter 7

Conclusions

As mentioned at the beginning of this thesis, the energy landscape is increasingly shifting towards the use of renewable sources. In particular, among renewable sources, nuclear fusion could become the only technology that allows electricity to be produced with zero emissions.
The use of nuclear fusion would shift the focus to the use of steam turbines for energy production.
A European project is currently underway to build a working nuclear fusion demonstration plant (DEMO). Many European companies have joined this project, including Ansaldo Energia, which is supplying the turbine. For reasons related to the structural integrity of the plant, periodic shutdowns and restarts will be necessary.
This causes the turbine to go through transients in which the steam flow rate is very low compared to the nominal values. Extremely low steam flow rates are sufficient to drive the first stages, while the last stage is driven by the previous ones and thus operates in compressor mode, centrifuging the residual steam. These conditions are known as ventilation conditions and cause:

- A significant increase in blade temperature.
- Rotating stall cells.
- Asynchronous external excitations.

Under standard operating conditions, the steam turbine operates with a continuous steam flow rate, which means that:

- The temperature on the blade remains constant once operating conditions are reached.
- The external excitations are synchronous, so they are multiples of the rotation speed.

Since the external excitations are multiples of the rotational speed, during the design phase it is possible to prevent the natural frequencies of the blade from falling within the range of exciting frequencies.
As mentioned above, the turbine supplied by Ansaldo Energia will be powered by steam produced by a nuclear fusion plant, so it will operate under ventilation conditions. The increase in blade temperature, which reduces the natural frequencies of the system, combined with asynchronous external excitations, could lead to unexpected resonance.
The blades of the last stage are very long, so when resonance occurs, they vibrate with very high amplitudes. Very high vibration amplitudes, if not properly damped, can lead to catastrophic failure due to high cycle fatigue (HCF).
To avoid this, the blades of the last stage are equipped with mechanical friction damping systems. In this specific case, the blades of the last stage of the steam turbine supplied by Ansaldo Energia are equipped with a snubber, which allows part of the kinetic energy to be dissipated during vibrations. The non-linear friction forces acting on the system significantly influence the dynamic response of the system, and consequently the dynamic stresses also depend on these forces.
In order to accurately predict the fatigue life of the blades and avoid catastrophic failures, it is important to be able to calculate the dynamic stresses taking into account the effect of friction contacts.
As mentioned above, the blades of the last stage of the turbine in question are characterized by very large dimensions in terms of length. This means that, in addition to vibrating with very high amplitudes, they are subject to large static deformations. This aspect cannot be overlooked in the calculation of dynamic stresses, as it would lead to an incorrect assessment of the stresses and, consequently, of the fatigue life of the component.
This additional challenge required the development of a specific procedure that was able to include all of the following aspects in the calculation of dynamic stresses:

- The high static deformation of the blades.

- The presence of friction contacts.
- The effect of the static contact forces.

The work carried out during this PhD programme and presented in this thesis has proven to be valid for this purpose. The procedure developed has been successfully applied to the blades of the last stage of the Ansaldo Energia steam turbine, allowing the calculation of dynamic stresses taking into account all the previously cited aspects.

7.1 Future work

The procedure developed during this PhD programme constitutes a robust and reliable tool for predicting the fatigue life of blades. It is important to note that the calculation of dynamic stresses is closely linked to the calculation of the non-linear forced response of the system. In this thesis, Ansaldo non-linear tool was used to calculate the non-linear forced response.
Currently, Ansaldo non-linear tool allows the external excitation to be applied as a concentrated load on a single node. As discussed in Chapter 5, this is an approximation; in reality, the external excitation derives from the interaction between the fluid and the structure and is distributed over the entire surface of the blade.
In Appendix B is successfully demonstrated that ANSYS allows the static pressure field to be reduced in order to obtain a reduced load vector, which can be directly imported into Ansaldo non-linear tool. Currently, this additional step has been performed on a simple system, a cantilever beam.
Future work involves applying the reduction to a field of real static pressures, derived from CFD calculations, and performing a non-linear forced response calculation to evaluate the effectiveness of the method. This further step would allow for a more realistic external excitation to be considered and would improve the robustness and reliability of the procedure for calculating dynamic stresses in presence of friction contacts.

References

[1] A R Laksana, A M Kokong, P Agus Sigit, T Widjajanto, H Setiawan, and I Djunaedi. Flutter Analysis of Last Stage Steam Turbine Power Plant Blade Through Transient Blade Row Simulation. *IOP Conference Series: Materials Science and Engineering*, 1096(1):012093, March 2021.

[2] Christian Frey, Graham Ashcroft, Hans-Peter Kersken, and Daniel Schlüß. Flutter Analysis of a Transonic Steam Turbine Blade with Frequency and Time-Domain Solvers. *International Journal of Turbomachinery, Propulsion and Power*, 4(2):15, June 2019.

[3] Chandra Shekhar Prasad and Luděk Pešek. Analysis of classical flutter in steam turbine blades using reduced order aeroelastic model. *MATEC Web of Conferences*, 211:15001, 2018.

[4] Dalila Dimaggio, Andrea Riva, Caterina Bardetta, Andrea Sanguineti, Klaus Störzel, and Sven Käfer. Fatigue assessment of a notched member under combined LCF and HCF loading. *Procedia Structural Integrity*, 7:198–205, 2017.

[5] Shilun Sheng, Johan Flegler, Balazs Janos Becs, and Michael Dankert. HCF Component Tests on Full-Scale Low Pressure Steam Turbine End Stage Blades. In *Volume 8: Microturbines, Turbochargers and Small Turbomachines; Steam Turbines*, page V008T26A022, Seoul, South Korea, June 2016. American Society of Mechanical Engineers.

[6] Z. Mazur, R. García-Illescas, and J. Porcayo-Calderón. Last stage blades failure analysis of a 28MW geothermal turbine. *Engineering Failure Analysis*, 16(4):1020–1032, June 2009.

[7] Naoki Shibukawa, Tomohiro Tejima, Yoshifumi Iwasaki, Itaru Murakami, and Ikuo Saito. A Correlation Between Vibration Stresses and Flow Features of Steam Turbine Long Blades in Low Load Conditions. In *Volume 7: Turbomachinery, Parts A, B, and C*, pages 2437–2446, Vancouver, British Columbia, Canada, January 2011. ASMEDC.

[8] L. Y. Zhang, L. He, and H. Stüer. A Numerical Investigation of Rotating Instability in Steam Turbine Last Stage. *Journal of Turbomachinery*, 135(1):011009, January 2013.

[9] B. R. Haller, T. S. Rice, and R. Sigg. Alleviation of Rotating Pressure Oscillations in the Last LP Turbine Stage During Low-Load Conditions. In *Volume 8: Microturbines, Turbochargers and Small Turbomachines; Steam Turbines*, page V008T26A004, Seoul, South Korea, June 2016. American Society of Mechanical Engineers.

[10] W Gerschütz, M Casey, and F Truckenmüller. Experimental investigations of rotating flow instabilities in the last stage of a low-pressure model steam turbine during windage. *Proceedings of the Institution of Mechanical Engineers, Part A: Journal of Power and Energy*, 219(6):499–510, January 2005.

[11] Roland Sigg and Timothy Rice. The Characteristics of Rotating Instabilities in Low Pressure Steam Turbines at Low Volume Flow Operation. In *Volume 8: Microturbines, Turbochargers and Small Turbomachines; Steam Turbines*, page V008T26A028, Montreal, Quebec, Canada, June 2015. American Society of Mechanical Engineers.

[12] Jan Ph. Heners, Christoph Müller-Schindewolffs, Frederik Blum, and Damian M. Vogt. Prediction of the Unsteady Transition Behavior in Low Pressure Turbine Flows Using Time and Frequency Domain Methods. In *Volume 2E: Turbomachinery*, page V02ET41A007, Virtual, Online, September 2020. American Society of Mechanical Engineers.

[13] R Sigg, C Heinz, M V Casey, and N Sürken. Numerical and experimental investigation of a low-pressure steam turbine during windage. *Proceedings of the Institution of Mechanical Engineers, Part A: Journal of Power and Energy*, 223(6):697–708, September 2009.

[14] Benjamin Megerle, Ivan McBean, Timothy Stephen Rice, and Peter Ott. Unsteady Aerodynamics of Low-Pressure Steam Turbines Operating Under Low Volume Flow.

[15] Lihua Cao, Wenlong Wang, Huanhuan Luo, Pengfei Hu, Zhengwen Li, Yanjun Zhang, and Tingshan Ma. Analysis on flow separation characteristics of last stage blade in steam turbine under small volume flow condition. *Thermal Science*, 23(5 Part B):3239–3250, 2019.

[16] Victor Filippenko, Boris Frolov, Andrey Chernobrovkin, Bin Zhou, Amir Mujezinovic ́, and Jon Slepski. Analyses of Temperature Distribution on Steam Turbine Last Stage Low Pressure Buckets at Low Flow Operations. In *Volume 7: Turbomachinery, Parts A, B, and C*, pages 2463–2469, Vancouver, British Columbia, Canada, January 2011. ASMEDC.

[17] Antonio Mambro, Francesco Congiu, Enzo Galloni, and Laura Canale. Experimental study and modelling of the ventilation power and maximum temperature of low-pressure steam turbine last stages at low load. *Applied Energy*, 241:59–72, May 2019.

[18] Adam Beevers, Said Havakechian, and Benjamin Megerle. On the Prediction and Theory of the Temperature Increase of Low Pressure Last Stage Moving Blades During Low Volume Flow Conditions, and Limiting it Through Steam Extraction Methods. *Journal of Turbomachinery*, 137(10):101002, October 2015.

[19] Meichao Xu, Lihua Cao, and Linsen Song. Structure and modal analysis of the last stage blade in steam turbine under low volume flow conditions. *Engineering Failure Analysis*, 131:105820, January 2022.

[20] Erhan Ferhatoglu, Chiara Gastaldi, Daniele Botto, and Stefano Zucca. An experimental and computational comparison of the dynamic response variability in a turbine blade with under-platform dampers. *Mechanical Systems and Signal Processing*, 172:108987, June 2022.

[21] E. P. Petrov. Explicit Finite Element Models of Friction Dampers in Forced Response Analysis of Bladed Disks. *Journal of Engineering for Gas Turbines and Power*, 130(2):022502, March 2008.

[22] J. H. Griffin. Friction Damping of Resonant Stresses in Gas Turbines Airfoils. *J. Eng. Power*, 102:329–333, 1980.

[23] W. Gu, Z. Xu, and Y. Liu. A method to predict the nonlinear vibratory response of bladed disc system with shrouded dampers. *Proc. Inst. Mech. Eng. Part C J.Mech.*, 226:1620–1632, 2011.

[24] Shi Yajie, Hong Jie, Shan Yingchun, and Zhu Zigen. Forced Response Analysis of Shrouded Blades by an Alternating Frequency/Time Domain Method. In *Volume 5: Marine; Microturbines and Small Turbomachinery; Oil and Gas Applications; Structures and Dynamics, Parts A and B*, pages 865–872, Barcelona, Spain, January 2006. ASMEDC.

[25] J. Szwedowicz, R. Visser, W. Sextro, and P. A. Masserey. On Nonlinear Forced Vibration of Shrouded Turbine Blades. *Journal of Turbomachinery*, 130(1):011002, January 2008.

[26] B. D. Yang, J. J. Chen, and C. H. Menq. Prediction of Resonant Response of Shrouded Blades With Three-Dimensional Shroud Constraint. *Journal of Engineering for Gas Turbines and Power*, 121(3):523–529, July 1999.

[27] Jie Yuan, Chiara Gastaldi, Enora Denimal Goy, and Benjamin Chouvion. Friction damping for turbomachinery: A comprehensive review of modelling, design strategies, and testing capabilities. *Progress in Aerospace Sciences*, 147:101018, May 2024.

[28] Alessandro Sommariva and Stefano Zucca. A Comparison between Two Reduction Strategies for Shrouded Bladed Disks. *Applied Sciences*, 8(10):1736, September 2018.

[29] Lakshminarayana Reddy Tamatam, Daniele Botto, and Stefano Zucca. A coupled approach to model the effect of wear on the dynamics of the shrouded bladed disk.

[30] S Mehrdad Pourkiaee and Stefano Zucca. NONLINEAR FORCED RESPONSE ANALYSIS OF BLADED DISKS USING A RELATIVE CYCLIC COMPONENT MODE SYNTHESIS APPROACH. 2019.

[31] F. Mashayekhi, A.S. Nobari, and S. Zucca. Hybrid reduction of mistuned bladed disks for nonlinear forced response analysis with dry friction. *International Journal of Non-Linear Mechanics*, 116:73–84, November 2019.

[32] Samuel Quaegebeur, Benjamin Chouvion, and Fabrice Thouverez. Nonlinear dynamic analysis of three-dimensional bladed-disks with frictional contact interfaces based on cyclic reduction strategies. *International Journal of Solids and Structures*, 236-237:111277, February 2022.

[33] R. Drozdowski, L. Völker, M. Häfele, and D. M. Vogt. Experimental and Numerical Investigation of the Nonlinear Vibrational Behavior of Steam Turbine Last Stage Blades With Friction Bolt Damping Elements. In *Volume 8: Microturbines, Turbochargers and Small Turbomachines; Steam Turbines*, page V008T26A007, Montreal, Quebec, Canada, June 2015. American Society of Mechanical Engineers.

[34] Christian Siewert, Frank Sieverding, William J. McDonald, Manish Kumar, and James R. McCracken. Development of a Last Stage Blade Row Coupled by Damping Elements: Numerical Assessment of its Vibrational Behavior and its Experimental Validation During Spin Pit Measurements. In *Volume 8: Microturbines, Turbochargers and Small Turbomachines; Steam Turbines*, page V008T29A018, Charlotte, North Carolina, USA, June 2017. American Society of Mechanical Engineers.

[35] Erhan Ferhatoglu, Stefano Zucca, Daniele Botto, Jury Auciello, and Lorenzo Arcangeli. Nonlinear Vibration Analysis of Turbine Bladed Disks With Midspan Dampers. *Journal of Engineering for Gas Turbines and Power*, 144(4):041021, April 2022.

[36] Stefano Zucca, Muzio M. Gola, and Francesco Piraccini. Non-Linear Dynamics of Steam Turbine Blades With Shroud: Numerical Analysis and Experiments. In *Volume 6: Oil and Gas Applications; Concentrating Solar Power Plants; Steam Turbines; Wind Energy*, pages 665–674, Copenhagen, Denmark, June 2012. American Society of Mechanical Engineers.

[37] N.S. Vyas, Sidharth, and J.S. Rao. Dynamic stress analysis and a fracture mechanics approach to life prediction of turbine blades. *Mechanism and Machine Theory*, 32(4):511–527, May 1997.

[38] Tie Chen, John Rogerson, Fang Yang, Gurnam Singh, and Phil Hemsley. Development of State of the Art Dynamic Stress Prediction Methodology for

Steam Turbines. In *Volume 6: Structures and Dynamics, Parts A and B*, pages 113–120, Vancouver, British Columbia, Canada, January 2011. ASMEDC.

[39] Giuseppe Battiato and Christian M. Firrone. Stress recovery algorithm for reduced order models of mechanical systems in nonlinear dynamic operative conditions. *Nonlinear Dynamics*, 108(2):1463–1478, April 2022.

[40] A. Cardona, T. Coune, and A. Lerusse. A multi-harmonic method for nonlinear vibration analysis. *J. Numer. Methods.*, 217:1593–1608, 1998.

[41] Enio Colonna, Teresa Berruti, Daniele Botto, and Andrea Bessone. Non-Linear Forced Response of Vibrating Mechanical Systems: The Impact of Computational Parameters. *Applied Sciences*, 15(16):9112, August 2025.

[42] T. M. Cameron and J. H. Griffin. An Alternating Frequency/Time Domain Method for Calculating the Steady-State Response of Nonlinear Dynamic Systems. *Journal of Applied Mechanics*, 56(1):149–154, March 1989.

[43] Tony F. C. Chan and H. B. Keller. Arc-Length Continuation and Multigrid Techniques for Nonlinear Elliptic Eigenvalue Problems. *SIAM Journal on Scientific and Statistical Computing*, 3(2):173–194, June 1982.

[44] Xinwei Zhao, Hongkun Li, Shuhua Yang, and Zhenfang Fan. Experimental Research on Rotating Stall Induced Blade Vibration in an Unshrouded Centrifugal Compressor.

Appendix A

Analytical Jacobian matrix for non-linear forced response computation

Necessity of analytical Jacobian matrix

Chapter 5 discussed in detail the procedure for calculating dynamic stresses on blades, taking into account the behavior of friction contacts. To achieve this, the importance of calculating the non-linear forced response of the reduced system was highlighted. Calculating the non-linear forced response of the reduced system allows the dynamic friction forces to be computed, which are necessary for calculating the dynamic stresses in ANSYS. To ensure the correct calculation of dynamic stresses, it is important that Ansaldo non-linear tool achieves convergence for all frequencies in the analyzed range. It is also important to minimize calculation times. The time required to calculate the non-linear forced response depends mainly on three factors:

- The number of contact pairs condensed in the reduced model.
- The method used to calculate the derivatives of the contact forces required for the iterative solver.
- The number of points at which the time domain is discretized in the AFT scheme.

Here, we will not consider the last point, but instead evaluate the first two. By increasing the number of contact pairs, the degrees of freedom on which the friction forces act increase, consequently increasing the number of non-linear terms that the solver must minimize.
In order to calculate the next point during iterations, the non-linear solver requires the matrix of residual derivatives, which can be calculated in two ways:

- Numerically, using finite differences.
- Analytically.

The first method is very computationally expensive and significantly increases calculation times.
The second method is entirely analytical and allows for an exponential reduction in computation time, while at the same time increasing the software's robustness. For this reason, the tool developed by the Aermec group of the Polytechnic University of Turin for Ansaldo Energia uses the analytical Jacobian to compute the non-linear forced response of the reduced-order model.
Considering what has been said so far, it is easy to understand the importance of being able to calculate the Jacobian matrix in a completely analytical manner.
The following section explains in detail, from mathematical point of view, how the derivatives of the contact forces, which are necessary for constructing the Jacobian matrix, are calculated using a fully analytical approach.

Analytical Jacobian matrix computation

The previous section highlighted the importance of including the calculation of the analytical Jacobian in the iterative solution scheme of the reduced system's equation of motion. This increases the robustness of the solver and at the same time exponentially reduces calculation times.
In this section, the problem of calculating the analytical Jacobian will be addressed from a mathematical point of view.

Equation of motion of the reduced blade model

Consider a bladed disk in the last stage of a steam turbine, for which we want to calculate the non-linear forced response in a certain frequency range. The first step is to reduce the full FEM model, as discussed in detail in Chapter 4. Once the reduction process is complete, all the input files required by Ansaldo non-linear tool to perform the non-linear calculation are obtained:

- The reduced mass and stiffness matrices, $[K]_{CB}$ and $[M]_{CB}$.
- The master nodes.
- The contact pairs.

For this example, a simplified case will be considered, in which only the first harmonic of the displacements is considered and the following degrees of freedom are condensed in the reduced model:

- The force node.
- 2 tip timing nodes.
- One contact pair, so two contact nodes.
- 100 modal degrees of freedom.

Note that this is an extremely simplified case, constructed to streamline the mathematical discussion. In real applications, more harmonics can be used, and the contact nodes condensed in the reduced model are usually much more numerous.
The non-linear equation of motion of the fundamental sector reduced system can be written as follows:

$$\Big[M\Big]_{CB}\Big\{\ddot{U}\Big\}+\Big[C\Big]_{CB}\Big\{\dot{U}\Big\}+\Big[K\Big]_{CB}\Big\{U\Big\}=\Big\{F\Big\}-\Big\{F\Big\}_{nl}\Big(\Big\{U\Big\},\Big\{\dot{U}\Big\},t\Big) \quad (28)$$

In which:

- $[M]_{CB}$,$[K]_{CB}$ and $[C]_{CB}$ are the reduced matrices. The damping matrices can be easily obtained as a linear combination of the stiffness and mass matrices: $[C]_{CB}=\alpha[M]_{CB}+\beta[K]_{CB}$

- $\left\{F\right\}$ is the external forcing vector.
- $\left\{F\right\}_{nl}\left(\left\{U\right\},\left\{\dot{U}\right\},t\right)$ is the non-linear friction force vector.
- $\left\{U\right\}$ is the displacements vector, that is the unknown of the problem.

We are interested in the frequency response of the reduced model, so Equation 28 must be solved in the frequency domain.
Considering what was explained in detail in Chapter 3, and assuming that we are only interested in the first harmonic of the MHBM calculation, the previous equation in the frequency domain can be written as:

$$\left(-\omega^2\left[M\right]_{CB}+i\omega\left[C\right]_{CB}+\left[K\right]_{CB}\right)\left\{\bar{U}\right\}-\left\{\bar{F}\right\}+\left\{\bar{F}\right\}_{nl}\left(\bar{U}\right)=\left\{R\right\} \tag{29}$$

The term $-\omega^2[M]_{CB}+i\omega[C]_{CB}+[K]_{CB}$ is the dynamic stiffness of the system and it will be called $[D]$.
Equation 27 can be rewritten as follows:

$$\left[D\right]\left\{\bar{U}\right\}-\left\{\bar{F}\right\}+\left\{\bar{F}\right\}_{nl}\left(\left\{\bar{U}\right\}\right)=\left\{R\right\} \tag{30}$$

As can be seen in the previous equation, the second member of Equation 30 is not equal to zero, because the equation cannot be solved exactly; consequently, it is necessary to find an approximate solution.
The friction force vector depends on the displacement vector, which is the unknown quantity in the problem. For this reason, Equation 27 must be solved iteratively, and the solver needs a starting vector to begin iterating and minimizing the residual vector.
Suppose we want to solve Equation 30 for a frequency $\omega=\omega_n$, and that the solution in terms of displacement for the frequency $\omega=\omega_{n-1}$ has already been calculated. For the j-th iteration, we can then write a Newton like iterative scheme as follows:

$$\left\{\bar{U}\right\}_{j+1}=\left\{\bar{U}\right\}_{j}-\left[J\right]^{-1}\left(\left\{\bar{U}\right\}_{j}\right)\left\{R\right\}\left(\left\{\bar{U}\right\}_{j}\right) \tag{31}$$

in whuch:

- $\left\{\bar{U}\right\}_{j+1}$ is the displacements vector at $j+1$ iteration, that is unknown.

- $\left\{\bar{U}\right\}_j$ is the displacements vector obtained for the j-th iteration.
- $\left[J\right]^{-1}\left(\left\{\bar{U}\right\}_j\right)$ is the inverse of the Jacobian matrix, evaluated for the current displacements vector.
- $\left\{R\right\}\left(\left\{\bar{U}\right\}_j\right)$ is the residual function evaluated for the current displacements vector.

Equation 31 clearly shows how, in the Newton-type iterative scheme, the Jacobian matrix is essential in allowing the solver to determine the next point and thus continue the scheme until the residual falls below a set tolerance.
As mentioned above, the Jacobian matrix can be calculated either with finite differences or completely analytically. Finite differences make the calculation of the Jacobian very costly and prone to numerical errors, which is why it is preferable to use the analytical approach.
Referring to Equation 31, the Jacobian matrix is defined as:

$$\left[J\right] = \frac{\partial\left\{R\right\}}{\partial\left\{\bar{U}\right\}} = \left[D\right] - \frac{\partial\left\{\bar{F}\right\}}{\partial\left\{\bar{U}\right\}} + \frac{\partial\left\{\bar{F}\right\}_{nl}}{\partial\left\{\bar{U}\right\}} \tag{32}$$

In Equation 30:

- $\left[D\right]$ is the dynamic stiffness, which can be computed very easily.
- $\frac{\partial\left\{\bar{F}\right\}}{\partial\left\{\bar{U}\right\}}$ is equal to zero, since the external excitation does not depend on the displacements vector.

The only term that need to be computed in previous equation is $\frac{\partial\left\{\bar{F}\right\}_{nl}}{\partial\left\{\bar{U}\right\}}$.
The only displacement vector terms that must be calculated iteratively are those relating to the contact nodes, on which the friction forces act. The displacements on the other nodes of the reduced model can be calculated using the linear model. Therefore, in Equation 29 and Equation 30, only the degrees of freedom relating to the contact nodes are isolated.
For this example, only one contact pair has been condensed in the reduced model. Consider that the blades of the last stage of the bladed disk under consideration are

coupled together by means of the snubber. Consequently, a contact node is taken on the contact surface of the snubber on the suction side and a contact node on the contact surface of the snubber on the pressure side.
What has been said so far is shown in Figure 48:

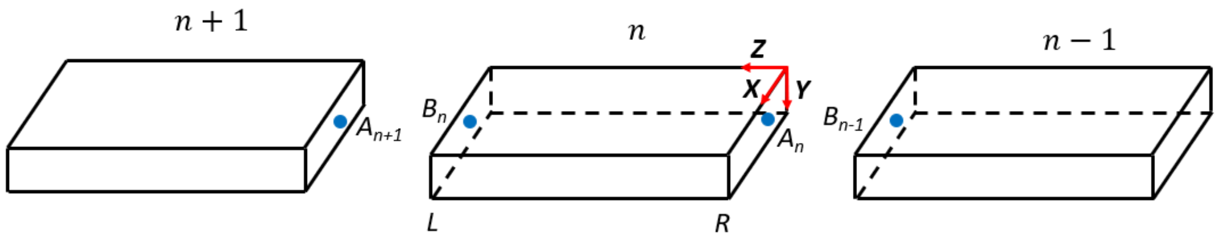

Figure 46: Contact configuration

in which:

- $n, n+1$ and $n-1$ represent respectively the fundamental sector, the $n+1$ sector and the $n-1$ sector.
- L and R are respectively the contact surface of the snubber on the pressure side and the contact surface of the snubber on the suction side, for the fundamental sector.
- X, Y and Z are the three axis of the local reference system consistent with the contact.
- A_n and B_n are the contact nodes condensed in the reduced model of the fundamental sector.
- A_{n+1} and B_{n-1} are respectively the contact node A on the $n+1$ sector and the node B on the $n-1$ sector.

In order to calculate the derivatives of the contact forces with respect to displacement, it is first necessary to compute the contact forces.
The contact forces, as discussed extensively in Chapter 3, are calculated within the contact model, which takes displacement as input. In this case, the input displacement is a relative displacement, as there is a phase difference between the displacements

of the n-th sector and those of sectors n+1 and n-1, due to the nature of the external excitation.
Each node has three degrees of freedom, so the relative displacement field is three-dimensional and the 3D contact model analyzed in Chapter 3 must be used.
The reduced model contains the degrees of freedom of the fundamental sector, so in order to compute the relative displacements, the cyclic symmetry boundary conditions must be used, Appendix C.
At this point, all the elements needed to calculate the friction forces acting on the contact nodes are available. Assuming that the physical displacements of the contact nodes of the fundamental sector have been calculated for the j-th iteration, we can then write:

$$\begin{aligned} \left\{\bar{U}\right\}_{n+1}^{A} &= \left\{\bar{U}\right\}_{n}^{A} e^{i\varphi} \\ \left\{\bar{U}\right\}_{n-1}^{B} &= \left\{\bar{U}\right\}_{n}^{B} e^{-i\varphi} \end{aligned} \tag{33}$$

To calculate the contact forces on the A_n and B_n, the relative displacement must be input into the contact model, which is calculated as:

- $\left\{\bar{U}\right\}_{rel}^{L} = \left\{\bar{U}\right\}_{n}^{B} - \left\{\bar{U}\right\}_{n}^{A} e^{i\varphi}$ is the relative displacment on the *PS* contact surface.
-
- $\left\{\bar{U}\right\}_{rel}^{R} = \left\{\bar{U}\right\}_{n}^{A} - \left\{\bar{U}\right\}_{n}^{B} e^{-i\varphi}$ is the relative displacement on the *SS* contact surface.

in which:

- $\left\{\bar{U}\right\}_{rel}^{L} = \begin{Bmatrix} \bar{X}_{rel} \\ \bar{Y}_{rel} \\ \bar{Z}_{rel} \end{Bmatrix}^{L}$
- $\left\{\bar{U}\right\}_{rel}^{R} = \begin{Bmatrix} \bar{X}_{rel} \\ \bar{Y}_{rel} \\ \bar{Z}_{rel} \end{Bmatrix}^{R}$

- $\left\{\bar{U}\right\}_n^A = \begin{Bmatrix} \bar{X}_A \\ \bar{Y}_A \\ \bar{Z}_A \end{Bmatrix}_n$
- $\left\{\bar{U}\right\}_n^B = \begin{Bmatrix} \bar{X}_B \\ \bar{Y}_B \\ \bar{Z}_B \end{Bmatrix}_n$
- $\varphi = h\frac{2\pi}{N}$. For the notation refer to Appendix C

The relative displacements, both on the pressure side and on the suction side, are given as input to the contact model, within which the contact forces are calculated in the time domain using the predictor-corrector model explained in Chapter 3, which we recall here:

$$T_{xPredicted}(t) = k_x(u_x(t) - w_x(t)) \tag{34}$$

$$T_{yPredicted}(t) = k_y(u_y(t) - w_x(t)) \tag{35}$$

$$N(t) = max(k_n v(t), 0) \tag{36}$$

$$T_x(t) = \begin{cases} T_{xPredicted}(t) & stick \\ \mu n(t) sign(T_x(t)) & slip \\ 0 & separation \end{cases} \tag{37}$$

$$T_y(t) = \begin{cases} T_{yPredicted}(t) & stick \\ \mu n(t) sign(T_y(t)) & slip \\ 0 & separation \end{cases} \tag{38}$$

For information on the symbols used, please refer to Chapter 3.
The Equations relating to the calculation of the predicted tangential force can be rewritten as follows:

$$\begin{aligned} T_{xPredicted}(t) &= k_x(u_x(t) - u_x(t-1)) + T_{xPredicted}(t-1) \\ T_{yPredicted}(t) &= k_y(u_y(t) - u_y(t-1)) + T_{yPredicted}(t-1) \end{aligned} \tag{39}$$

We are interested in solving the motion equation of the reduced model in the frequency domain, therefore the derivatives of the contact forces must also be expressed as Fourier coefficients, whose analytical expressions are as follows:

$$
\begin{aligned}
\Re\left(\frac{\partial \bar{T_X}}{\partial \bar{X}}\right) &= \frac{1}{\pi}\int_0^{2\pi}\frac{\partial T_x(t)}{\partial u_x(t)}cos(\omega t)dt \\
\Im\left(\frac{\partial \bar{T_X}}{\partial \bar{X}}\right) &= -\frac{1}{\pi}\int_0^{2\pi}\frac{\partial T_x(t)}{\partial u_x(t)}sin(\omega t)dt \\
\Re\left(\frac{\partial \bar{N}}{\partial \bar{Z}}\right) &= \frac{1}{\pi}\int_0^{2\pi}\frac{\partial N(t)}{\partial v(t)}cos(\omega t)dt \\
\Im\left(\frac{\partial \bar{N}}{\partial \bar{Z}}\right) &= -\frac{1}{\pi}\int_0^{2\pi}\frac{\partial N(t)}{\partial v(t)}sin(\omega t)dt
\end{aligned}
\tag{40}
$$

The analytical expressions of the Fourier coefficients of the tangential force along Y direction can be computed with the same equations used for the tangential force along X direction.

Equation 40 shows the analytical expressions that allow the real and imaginary parts of the Fourier coefficients of the contact force derivatives to be calculated. However, as explained in Chapter 3, in real applications the shape of the hysteresis cycle is not known a priori, so it is preferable to use the FFT algorithm, already implemented in Matlab.

The FFT algorithm takes a signal in the time domain as input and returns the Fourier coefficients. In order to obtain the Fourier coefficients of the contact forces, it is therefore necessary to first calculate the derivatives in the time domain. Considering Equations 37 and 38, the derivatives in the time domain are expressed as follows:

$$
\begin{aligned}
\frac{\partial T_x(t)}{\partial \Re\left(\bar{X}\right)} &= \begin{cases} k_t\left(cos\left(kt\frac{2\pi}{N_{teta}}\right) - cos\left(k(t-1)\frac{2\pi}{N_{teta}}\right)\right) + \frac{\partial T_x(t-1)}{\partial u_x(t-1)} & stick \\ 0 & slip \\ 0 & separation \end{cases} \\
\frac{\partial T_x(t)}{\partial \Re\left(\bar{Z}\right)} &= \begin{cases} \frac{\partial T_x(t-1)}{\partial u_x(t-1)} & stick \\ \mu k_n sign(T_{xPredicted}) cos\left(kt\frac{2\pi}{N_{teta}}\right) & slip \\ 0 & separation \end{cases} \\
\frac{\partial N(t)}{\partial \Re\left(\bar{Z}\right)} &= \begin{cases} k_n cos\left(kt\frac{2\pi}{N_{teta}}\right) & contact \\ 0 & separation \end{cases}
\end{aligned}
\tag{41}
$$

in which:

- k is the harmonic.
- t is the time instant.
- N_{teta} is the number of points used to discretize the time domain.

Note that in Equation 41, the expressions relating to the Y component of the tangential force have not been reported, as they are analogous to those written for the X component of the tangential force.
To summarize what has been said so far, in order to calculate the derivatives of the contact forces with respect to the displacements, it is first necessary to calculate the contact forces in the time domain. At this point, it is possible to calculate the derivatives analytically by evaluating the expressions of Equation 41 at each instant of the time domain.
As mentioned above, the equation of motion of the reduced system must be solved in the frequency domain, so it is necessary to determine the Fourier coefficients. If only the first harmonic is considered, the first coefficient is sufficient. The Fourier coefficients are calculated by applying the FFT algorithm to the derivative signal in the time domain. Equation 41 is applied for each contact pair, therefore the size of the Jacobian matrix is $l*l$, with $l = nc*2*3$. The parameter nc is the number of contact nodes condensed in the reduced model, while 2 and 3 are respectively the number of contact surfaces and the number of degrees of freedom for each contact node.
Considering that for this example only one contact pair is included in the reduced model, the dimension of the Jacobian matrix will be $12*12$.
Before showing the structure of the Jacobian matrix, it is important to define the matrices that impose cyclic symmetry conditions on the derivatives, which allow the

cross derivatives to be calculated.The rotation matrices are defined as follows:

$$
\Phi_P = \begin{bmatrix} cos(\varphi) & -sin(\varphi) & 0 & 0 & 0 & 0 \\ sin(\varphi) & cos(\varphi) & 0 & 0 & 0 & 0 \\ 0 & 0 & cos(\varphi) & -sin(\varphi) & 0 & 0 \\ 0 & 0 & sin(\varphi) & cos(\varphi) & 0 & 0 \\ 0 & 0 & 0 & 0 & cos(\varphi) & -sin(\varphi) \\ 0 & 0 & 0 & 0 & sin(\varphi) & cos(\varphi) \end{bmatrix}
$$
$$
\Phi_M = \begin{bmatrix} cos(\varphi) & sin(\varphi) & 0 & 0 & 0 & 0 \\ -sin(\varphi) & cos(\varphi) & 0 & 0 & 0 & 0 \\ 0 & 0 & cos(\varphi) & sin(\varphi) & 0 & 0 \\ 0 & 0 & -sin(\varphi) & cos(\varphi) & 0 & 0 \\ 0 & 0 & 0 & 0 & cos(\varphi) & sin(\varphi) \\ 0 & 0 & 0 & 0 & -sin(\varphi) & cos(\varphi) \end{bmatrix} \tag{42}
$$

in which:

- Φ_P is the matrix for imposing a rotation of $e^{i\varphi}$ to the $6*6$ derivatives block.
- Φ_M is the matrix for imposing a rotation of $e^{-i\varphi}$ to the $6*6$ derivatives block.

At this point, the Jacobian matrix can be assembled as follows:

$$
\begin{bmatrix}
\frac{\partial\Re(\bar{T}_X)^L}{\partial\Re(\bar{X}_{rel})^L} & \frac{\partial\Re(\bar{T}_X)^L}{\partial\Im(\bar{X}_{rel})^L} & \frac{\partial\Re(\bar{T}_X)^L}{\partial\Re(\bar{Y}_{rel})^L} & \frac{\partial\Re(\bar{T}_X)^L}{\partial\Im(\bar{Y}_{rel})^L} & \frac{\partial\Re(\bar{T}_X)^L}{\partial\Re(\bar{Z}_{rel})^L} & \frac{\partial\Re(\bar{T}_X)^L}{\partial\Im(\bar{Z}_{rel})^L} & \frac{\partial\Re(\bar{T}_X)^L}{\partial\Re(\bar{X}_{rel})^R} & \frac{\partial\Re(\bar{T}_X)^L}{\partial\Im(\bar{X}_{rel})^R} & \frac{\partial\Re(\bar{T}_X)^L}{\partial\Re(\bar{Y}_{rel})^R} & \frac{\partial\Re(\bar{T}_X)^L}{\partial\Im(\bar{Y}_{rel})^R} & \frac{\partial\Re(\bar{T}_X)^L}{\partial\Re(\bar{Z}_{rel})^R} & \frac{\partial\Re(\bar{T}_X)^L}{\partial\Im(\bar{Z}_{rel})^R} \\
\frac{\partial\Im(\bar{T}_X)^L}{\partial\Re(\bar{X}_{rel})^L} & \frac{\partial\Im(\bar{T}_X)^L}{\partial\Im(X\bar{rel})^L} & \frac{\partial\Im(\bar{T}_X)^L}{\partial\Re(\bar{Y}_{rel})^L} & \frac{\partial\Im(\bar{T}_X)^L}{\partial\Im(\bar{Y}_{rel})^L} & \frac{\partial\Im(\bar{T}_X)^L}{\partial\Re(\bar{Z}_{rel})^L} & \frac{\partial\Im(\bar{T}_X)^L}{\partial\Im(\bar{Z}_{rel})^L} & \frac{\partial\Im(\bar{T}_X)^L}{\partial\Re(\bar{X}_{rel})^R} & \frac{\partial\Im(\bar{T}_X)^L}{\partial\Im(\bar{X}_{rel})^R} & \frac{\partial\Im(\bar{T}_X)^L}{\partial\Re(\bar{Y}_{rel})^R} & \frac{\partial\Im(\bar{T}_X)^L}{\partial\Im(\bar{Y}_{rel})^R} & \frac{\partial\Im(\bar{T}_X)^L}{\partial\Re(\bar{Z}_{rel})^R} & \frac{\partial\Im(\bar{T}_X)^L}{\partial\Im(\bar{Z}_{rel})^R} \\
\frac{\partial\Re(\bar{T}_Y)^L}{\partial\Re(\bar{X}_{rel})^L} & \frac{\partial\Re(\bar{T}_Y)^L}{\partial\Im(\bar{X}_{rel})^L} & \frac{\partial\Re(\bar{T}_Y)^L}{\partial\Re(\bar{Y}_{rel})^L} & \frac{\partial\Re(\bar{T}_Y)^L}{\partial\Im(\bar{Y}_{rel})^L} & \frac{\partial\Re(\bar{T}_Y)^L}{\partial\Re(\bar{Z}_{rel})^L} & \frac{\partial\Re(\bar{T}_Y)^L}{\partial\Im(\bar{Z}_{rel})^L} & \frac{\partial\Re(\bar{T}_Y)^L}{\partial\Re(\bar{X}_{rel})^R} & \frac{\partial\Re(\bar{T}_Y)^L}{\partial\Im(\bar{X}_{rel})^R} & \frac{\partial\Re(\bar{T}_Y)^L}{\partial\Re(\bar{Y}_{rel})^R} & \frac{\partial\Re(\bar{T}_Y)^L}{\partial\Im(\bar{Y}_{rel})^R} & \frac{\partial\Re(\bar{T}_Y)^L}{\partial\Re(\bar{Z}_{rel})^R} & \frac{\partial\Re(\bar{T}_Y)^L}{\partial\Im(\bar{Z}_{rel})^R} \\
\frac{\partial\Im(\bar{T}_Y)^L}{\partial\Re(\bar{X}_{rel})^L} & \frac{\partial\Im(\bar{T}_Y)^L}{\partial\Im(\bar{X}_{rel})^L} & \frac{\partial\Im(\bar{T}_Y)^L}{\partial\Re(\bar{Y}_{rel})^L} & \frac{\partial\Im(\bar{T}_Y)^L}{\partial\Im(\bar{Y}_{rel})^L} & \frac{\partial\Im(\bar{T}_Y)^L}{\partial\Re(\bar{Z}_{rel})^L} & \frac{\partial\Im(\bar{T}_Y)^L}{\partial\Im(\bar{Z}_{rel})^L} & \frac{\partial\Im(\bar{T}_Y)^L}{\partial\Re(\bar{X}_{rel})^R} & \frac{\partial\Im(\bar{T}_Y)^L}{\partial\Im(\bar{X}_{rel})^R} & \frac{\partial\Im(\bar{T}_Y)^L}{\partial\Re(\bar{Y}_{rel})^R} & \frac{\partial\Im(\bar{T}_Y)^L}{\partial\Im(\bar{Y}_{rel})^R} & \frac{\partial\Im(\bar{T}_Y)^L}{\partial\Re(\bar{Z}_{rel})^R} & \frac{\partial\Im(\bar{T}_Y)^L}{\partial\Im(\bar{Z}_{rel})^R} \\
\frac{\partial\Re(\bar{N})^L}{\partial\Re(\bar{X}_{rel})^L} & \frac{\partial\Re(\bar{N})^L}{\partial\Im(\bar{X}_{rel})^L} & \frac{\partial\Re(\bar{N})^L}{\partial\Re(\bar{Y}_{rel})^L} & \frac{\partial\Re(\bar{N})^L}{\partial\Im(\bar{Y}_{rel})^L} & \frac{\partial\Re(\bar{N})^L}{\partial\Re(\bar{Z}_{rel})^L} & \frac{\partial\Re(\bar{N})^L}{\partial\Im(\bar{Z}_{rel})^L} & \frac{\partial\Re(\bar{N})^L}{\partial\Re(\bar{X}_{rel})^R} & \frac{\partial\Re(\bar{N})^L}{\partial\Im(\bar{X}_{rel})^R} & \frac{\partial\Re(\bar{N})^L}{\partial\Re(\bar{Y}_{rel})^R} & \frac{\partial\Re(\bar{N})^L}{\partial\Im(\bar{Y}_{rel})^R} & \frac{\partial\Re(\bar{N})^L}{\partial\Re(\bar{Z}_{rel})^R} & \frac{\partial\Re(\bar{N})^L}{\partial\Im(\bar{Z}_{rel})^R} \\
\frac{\partial\Im(\bar{N})^L}{\partial\Re(\bar{X}_{rel})^L} & \frac{\partial\Im(\bar{N})^L}{\partial\Im(\bar{X}_{rel})^L} & \frac{\partial\Im(\bar{N})^L}{\partial\Re(\bar{Y}_{rel})^L} & \frac{\partial\Im(\bar{N})^L}{\partial\Im(\bar{Y}_{rel})^L} & \frac{\partial\Im(\bar{N})^L}{\partial\Re(\bar{Z}_{rel})^L} & \frac{\partial\Im(\bar{N})^L}{\partial\Im(\bar{Z}_{rel})^L} & \frac{\partial\Im(\bar{N})^L}{\partial\Re(\bar{X}_{rel})^R} & \frac{\partial\Im(\bar{N})^L}{\partial\Im(\bar{X}_{rel})^R} & \frac{\partial\Im(\bar{N})^L}{\partial\Re(\bar{Y}_{rel})^R} & \frac{\partial\Im(\bar{N})^L}{\partial\Im(\bar{Y}_{rel})^R} & \frac{\partial\Im(\bar{N})^L}{\partial\Re(\bar{Z}_{rel})^R} & \frac{\partial\Im(\bar{N})^L}{\partial\Im(\bar{Z}_{rel})^R} \\
\frac{\partial\Re(\bar{T}_X)^R}{\partial\Re(\bar{X}_{rel})^L} & \frac{\partial\Re(\bar{T}_X)^R}{\partial\Im(\bar{X}_{rel})^L} & \frac{\partial\Re(\bar{T}_X)^R}{\partial\Re(\bar{Y}_{rel})^L} & \frac{\partial\Re(\bar{T}_X)^R}{\partial\Im(\bar{Y}_{rel})^L} & \frac{\partial\Re(\bar{T}_X)^R}{\partial\Re(\bar{Z}_{rel})^L} & \frac{\partial\Re(\bar{T}_X)^R}{\partial\Im(\bar{Z}_{rel})^L} & \frac{\partial\Re(\bar{T}_X)^R}{\partial\Re(\bar{X}_{rel})^R} & \frac{\partial\Re(\bar{T}_X)^R}{\partial\Im(\bar{X}_{rel})^R} & \frac{\partial\Re(\bar{T}_X)^R}{\partial\Re(\bar{Y}_{rel})^R} & \frac{\partial\Re(\bar{T}_X)^R}{\partial\Im(\bar{Y}_{rel})^R} & \frac{\partial\Re(\bar{T}_X)^R}{\partial\Re(\bar{Z}_{rel})^R} & \frac{\partial\Re(\bar{T}_X)^R}{\partial\Im(\bar{Z}_{rel})^R} \\
\frac{\partial\Im(\bar{T}_X)^R}{\partial\Re(\bar{X}_{rel})^L} & \frac{\partial\Im(\bar{T}_X)^R}{\partial\Im(\bar{X}_{rel})^L} & \frac{\partial\Im(\bar{T}_X)^R}{\partial\Re(\bar{Y}_{rel})^L} & \frac{\partial\Im(\bar{T}_X)^R}{\partial\Im(\bar{Y}_{rel})^L} & \frac{\partial\Im(\bar{T}_X)^R}{\partial\Re(\bar{Z}_{rel})^L} & \frac{\partial\Im(\bar{T}_X)^R}{\partial\Im(\bar{Z}_{rel})^L} & \frac{\partial\Im(\bar{T}_X)^R}{\partial\Re(\bar{X}_{rel})^R} & \frac{\partial\Im(\bar{T}_X)^R}{\partial\Im(\bar{X}_{rel})^R} & \frac{\partial\Im(\bar{T}_X)^R}{\partial\Re(\bar{Y}_{rel})^R} & \frac{\partial\Im(\bar{T}_X)^R}{\partial\Im(\bar{Y}_{rel})^R} & \frac{\partial\Im(\bar{T}_X)^R}{\partial\Re(\bar{Z}_{rel})^R} & \frac{\partial\Im(\bar{T}_X)^R}{\partial\Im(\bar{Z}_{rel})^R} \\
\frac{\partial\Re(\bar{T}_Y)^R}{\partial\Re(\bar{X}_{rel})^L} & \frac{\partial\Re(\bar{T}_Y)^R}{\partial\Im(\bar{X}_{rel})^L} & \frac{\partial\Re(\bar{T}_Y)^R}{\partial\Re(\bar{Y}_{rel})^L} & \frac{\partial\Re(\bar{T}_Y)^R}{\partial\Im(\bar{Y}_{rel})^L} & \frac{\partial\Re(\bar{T}_Y)^R}{\partial\Re(\bar{Z}_{rel})^L} & \frac{\partial\Re(\bar{T}_Y)^R}{\partial\Im(\bar{Z}_{rel})^L} & \frac{\partial\Re(\bar{T}_Y)^R}{\partial\Re(\bar{X}_{rel})^R} & \frac{\partial\Re(\bar{T}_Y)^R}{\partial\Im(\bar{X}_{rel})^R} & \frac{\partial\Re(\bar{T}_Y)^R}{\partial\Re(\bar{Y}_{rel})^R} & \frac{\partial\Re(\bar{T}_Y)^R}{\partial\Im(\bar{Y}_{rel})^R} & \frac{\partial\Re(\bar{T}_Y)^R}{\partial\Re(\bar{Z}_{rel})^R} & \frac{\partial\Re(\bar{T}_Y)^R}{\partial\Im(\bar{Z}_{rel})^R} \\
\frac{\partial\Im(\bar{T}_Y)^R}{\partial\Re(\bar{X}_{rel})^L} & \frac{\partial\Im(\bar{T}_Y)^R}{\partial\Im(\bar{X}_{rel})^L} & \frac{\partial\Im(\bar{T}_Y)^R}{\partial\Re(\bar{Y}_{rel})^L} & \frac{\partial\Im(\bar{T}_Y)^R}{\partial\Im(\bar{Y}_{rel})^L} & \frac{\partial\Im(\bar{T}_Y)^R}{\partial\Re(\bar{Z}_{rel})^L} & \frac{\partial\Im(\bar{T}_Y)^R}{\partial\Im(\bar{Z}_{rel})^L} & \frac{\partial\Im(\bar{T}_Y)^R}{\partial\Re(\bar{X}_{rel})^R} & \frac{\partial\Im(\bar{T}_Y)^R}{\partial\Im(\bar{X}_{rel})^R} & \frac{\partial\Im(\bar{T}_Y)^R}{\partial\Re(\bar{Y}_{rel})^R} & \frac{\partial\Im(\bar{T}_Y)^R}{\partial\Im(\bar{Y}_{rel})^R} & \frac{\partial\Im(\bar{T}_Y)^R}{\partial\Re(\bar{Z}_{rel})^R} & \frac{\partial\Im(\bar{T}_Y)^R}{\partial\Im(\bar{Z}_{rel})^R} \\
\frac{\partial\Re(\bar{N})^R}{\partial\Re(\bar{X}_{rel})^L} & \frac{\partial\Re(\bar{N})^R}{\partial\Im(\bar{X}_{rel})^L} & \frac{\partial\Re(\bar{N})^R}{\partial\Re(\bar{Y}_{rel})^L} & \frac{\partial\Re(\bar{N})^R}{\partial\Im(\bar{Y}_{rel})^L} & \frac{\partial\Re(\bar{N})^R}{\partial\Re(\bar{Z}_{rel})^L} & \frac{\partial\Re(\bar{N})^R}{\partial\Im(\bar{Z}_{rel})^L} & \frac{\partial\Re(\bar{N})^R}{\partial\Re(\bar{X}_{rel})^R} & \frac{\partial\Re(\bar{N})^R}{\partial\Im(\bar{X}_{rel})^R} & \frac{\partial\Re(\bar{N})^R}{\partial\Re(\bar{Y}_{rel})^R} & \frac{\partial\Re(\bar{N})^R}{\partial\Im(\bar{Y}_{rel})^R} & \frac{\partial\Re(\bar{N})^R}{\partial\Re(\bar{Z}_{rel})^R} & \frac{\partial\Re(\bar{N})^R}{\partial\Im(\bar{Z}_{rel})^R} \\
\frac{\partial\Im(\bar{N})^R}{\partial\Re(\bar{X}_{rel})^L} & \frac{\partial\Im(\bar{N})^R}{\partial\Im(\bar{X}_{rel})^L} & \frac{\partial\Im(\bar{N})^R}{\partial\Re(\bar{Y}_{rel})^L} & \frac{\partial\Im(\bar{N})^R}{\partial\Im(\bar{Y}_{rel})^L} & \frac{\partial\Im(\bar{N})^R}{\partial\Re(\bar{Z}_{rel})^L} & \frac{\partial\Im(\bar{N})^R}{\partial\Im(\bar{Z}_{rel})^L} & \frac{\partial\Im(\bar{N})^R}{\partial\Re(\bar{X}_{rel})^R} & \frac{\partial\Im(\bar{N})^R}{\partial\Im(\bar{X}_{rel})^R} & \frac{\partial\Im(\bar{N})^R}{\partial\Re(\bar{Y}_{rel})^R} & \frac{\partial\Im(\bar{N})^R}{\partial\Im(\bar{Y}_{rel})^R} & \frac{\partial\Im(\bar{N})^R}{\partial\Re(\bar{Z}_{rel})^R} & \frac{\partial\Im(\bar{N})^R}{\partial\Im(\bar{Z}_{rel})^R}
\end{bmatrix}
\tag{43}
$$

in which:

- The elements of rows $1-6$ and columns $1-6$ are the partial derivatives of the contact forces respect to the displacements, computed for the pressure side contact surface.

- The elements of rows $7-12$ and columns $7-12$ are the partial derivatives of the contact forces respect to the displacements, computed for the suction side contact surface.

- The elements of rows $1-6$ and columns $7-12$ are the partial derivatives of the contact forces on the pressure side contact surface respect to the displacements of the suction side contact surfaces. These elements are obtained multiplying the elements of rows $1-6$ and columns $1-6$ by the matrix Φ_P.

- The elements of rows $7-12$ and columns $1-6$ are the partial derivatives of the contact forces on the suction side contact surface respect to the displacements of the pressure side side contact surfaces. These elements are obtained multiplying the elements of rows $7-12$ and columns $7-12$ by the matrix Φ_M.

Chapter 3 discussed at length the possibility of using pseudo arc length continuation as a solution method. This technique, as discussed at length in Chapter 3, is used if there are turning points in the frequency response curve.
As shown in the dedicated chapter, when using pseudo arc length continuation, a constraint is added to the residual, which depends on both the displacements and the frequency. As a result, the Jacobian matrix does not remain the same, but it is necessary to add the derivatives of the constraint.
Let's recall the pseudo arc length continuation constraint, Chapter 3:

$$R_1 = \left(\begin{pmatrix} \bar{X}_{L\ rel} \\ \bar{Y}_{L\ rel} \\ \bar{Z}_{L\ rel} \\ \bar{X}_{R\ rel} \\ \bar{Y}_{R\ rel} \\ \bar{Z}_{R\ rel} \\ \omega \end{pmatrix} - \begin{pmatrix} \bar{X}_{LP\ rel} \\ \bar{Y}_{LP\ rel} \\ \bar{Z}_{LP\ rel} \\ \bar{X}_{RP\ rel} \\ \bar{Y}_{RP\ rel} \\ \bar{Z}_{RP\ rel} \\ \omega_P \end{pmatrix} \right)^T \begin{pmatrix} z_1 \\ z_2 \\ z_3 \\ z_4 \\ z_5 \\ z_6 \\ z_7 \end{pmatrix} \tag{44}$$

The notation is adapted to the example discussed in this section, but the mathematical treatment remains as discussed in Chapter 3.
Considering Equation 30 and Equation 44, the Jacobian matrix can be expressed as follows:

$$\begin{bmatrix} \frac{\partial \{R\}}{\partial \{\bar{U}_{rel}\}} & \frac{\partial \{R\}}{\partial \omega} \\ \frac{\partial R_1}{\partial \{\bar{U}_{rel}\}} & \frac{\partial R_1}{\partial \omega} \end{bmatrix} \tag{45}$$

The term 1-1 of the matrix in Equation 43 is exactly the entire matrix shown in Equation 43.
The other terms can be expressed as follows:

- Considering Equation 30: $\frac{\partial\left\{R\right\}}{\partial\omega} = \left(-2\omega\left[M\right]_{CB} + i\left[C\right]_{CB}\right)\left\{\bar{U}_{rel}\right\}$

- Considering Equation 44: $\frac{\partial R_1}{\partial\left\{\bar{U}_{rel}\right\}} = \begin{pmatrix} z_1 \\ z_2 \\ z_3 \\ z_4 \\ z_5 \\ z_6 \end{pmatrix}^T$

- Considering Equation 44: $\frac{\partial R_1}{\partial\omega} = z_7$

In conclusion, considering the pseudo arc length continuation constraint, the Jacobian matrix contains an extra row, which is the tangent vector, as discussed in Chapter 3, and an extra column, which can be easily calculated as discussed above.
This concludes the mathematical discussion on the calculation of the analytical Jacobian, both without the pseudo arc length continuation constraint and with this constraint. The implementation of the analytical Jacobian within the Ansaldo non-linear tool code makes the tool very robust, as analytical derivatives are not subject to numerical errors, and exponentially reduces calculation times, making the calculation of the non-linear forced response faster and more efficient.

Appendix B

Pressure field reduction for non-linear forced response computation

This appendix aims to discuss a possible improvement to the procedure that is the subject of this doctoral thesis.
In its current version, the Ansaldo's non-linear tool allows the external excitation to be applied as a concentrated force on one or more condensed nodes in the reduced model.
However, applying the external excitation as a concentrated force is an approximation; in reality, the blades undergo aerodynamic excitation through fluid-structure interaction. In the final stage of this PhD programme, an alternative was devised that allows for a more realistic simulation of the non-linear forced response. The alternative consists of reducing the static pressure field calculated using CFD with Craig-Bampton, thus obtaining a reduced load vector that can be directly used by the Ansaldo's non-linear tool to calculate the forced response.
This approach would allow the non-linear forced response to be calculated more accurately, simulating more realistically the external excitation that the blades undergo during vibrations.
Below is an example in which the effectiveness of this approach has been evaluated on a very simple model of a cantilever beam. Consider the Figure 47:

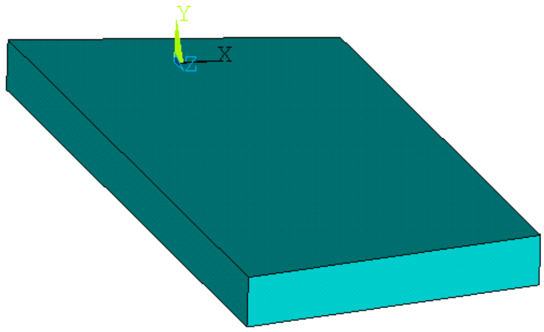

Figure 47: Cantilever beam

Figure 47 shows a cantilever beam model. A constant pressure field has been applied to the left surface of this beam, as now shown in Figure 48:

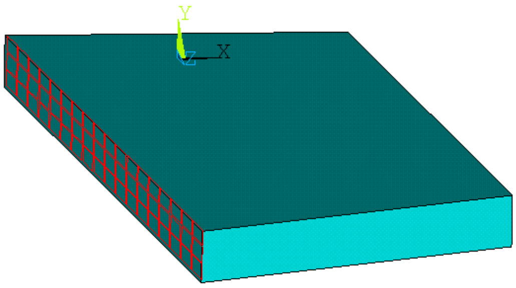

Figure 48: Cantilever beam with constant pressure field

The applied pressure field was reduced using the Craig-Bampton algorithm, already implemented in ANSYS, thus obtaining a reduced load vector. At this point, two analyses were performed:

- A linear harmonic analysis in ANSYS on the full FEM model of the beam, using the applied pressure field as an external excitation.
- A linear harmonic analysis in Matlab on the reduced model of the beam, using the reduced load vector obtained from the Craig-Bampton reduction as the external excitation.

The reduction of the beam model was performed in the same way as explained above (in this example, there are no centrifugal and contact forces involved, but the code used for the model reduction is the same), condensing 3 physical nodes and a certain number of modal degrees of freedom into the reduced matrices. The two analyses mentioned above, if the pressure field reduction has been performed correctly, should provide two overlapping FRFs. The result obtained is shown in the Figure 49:

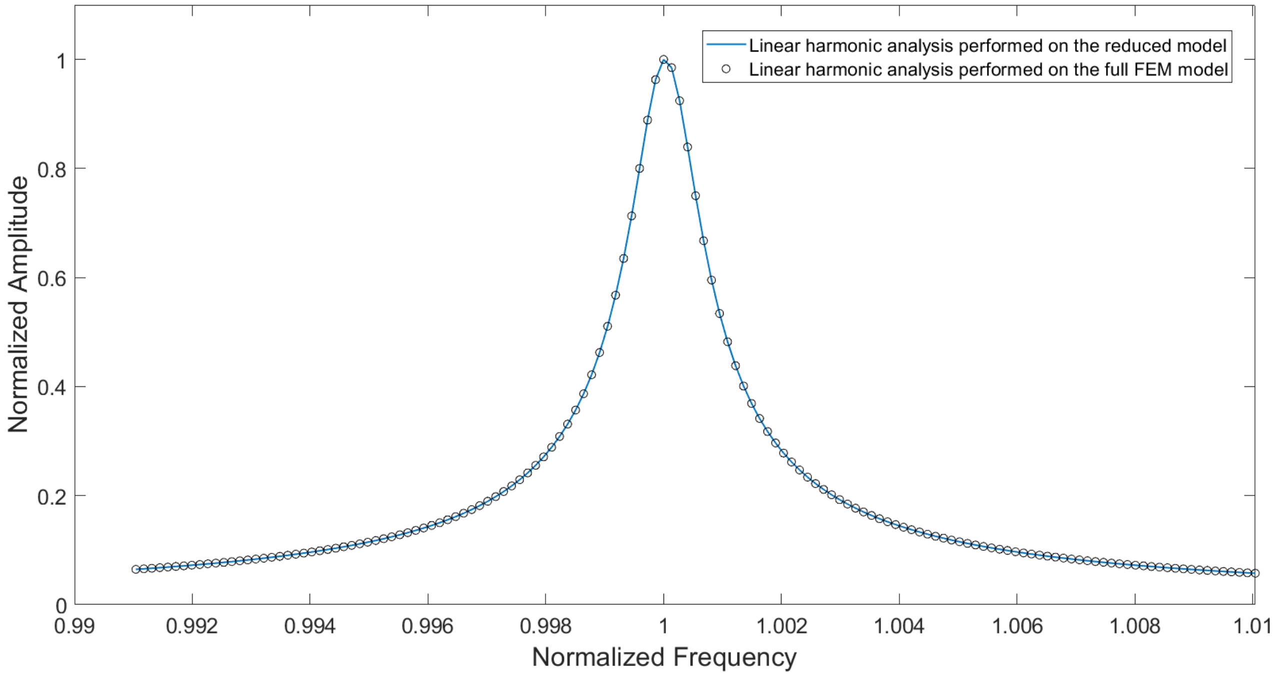

Figure 49: Comparison between the linear harmonic analysis performed on the reduced model and the linear harmonic analysis performed on the full FEM model

As can be seen from Figure 49, the displacement calculated, obviously on the same node, with linear harmonic analysis on the reduced model and that calculated with linear harmonic analysis on the full FEM model is identical. This indicates that the pressure field reduction was performed correctly, thus allowing the simulation of an external excitation that is not necessarily a concentrated load. This result can then be extended to the calculation of the forced response of turbine blades, ensuring a better approximation of the actual external excitations that cause vibrations.

Appendix C

Cyclic symmetry structures

This appendix is devoted to a recall on structures with cyclic symmetry properties, their modal properties and the computation of the forced response. A structure, in order to be defined and analyzed with cyclic symmetry properties, must be able to be divided into sectors that are all identical to each other. Bladed disks, fundamental components in the field of turbomachinery, are assemblies consisting of a disk, usually inflexible, and blades, the number of which may vary according to the type of turbine. Assuming that the blades have no manufacturing defects and that they have identical structural properties, these assemblies can be described from a modal and forced-response point of view as structures in cyclic symmetry, since they can be divided into identical sectors, each with a certain γ angle, until they form a 360-degree angle.
The fact that bladed disks can be analyzed as structures in cyclic symmetry is crucial, as this allows the modal information of the entire structure to be obtained simply by rotating the field of displacements of an n-th sector, called the fundamental sector.
To better understand the concept of a structure with cyclic symmetry properties, the last stage of the Ansaldo steam turbine is shown in Figure 50:

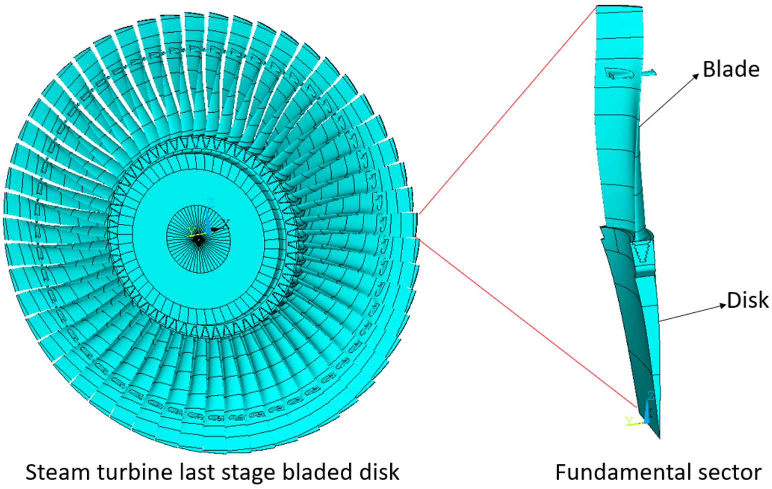

Figure 50: Steam turbine last stage bladed disk and fundamental sector

The last steam turbine stage shown in Figure 50 is a structure that can be described from the modal point of view using the boundary conditions of cyclic symmetry, in fact it can be divided into N identical sectors. The angle amplitude occupied by each sector can be calculated as $\gamma = \frac{2\pi}{N}$

C.1 Modal properties of cyclic symmetry structures

This subchapter is devoted to describing the modal properties of structures in cyclic symmetry and understanding what is involved in using these boundary conditions in the equations of motion of the structure itself. Considering the fundamental sector depicted in Figure 50, suppose to discretize it with two degrees of freedom, one modeling the disk and one modeling the blade. The resulting lumped parameter model is shown in Figure 51:

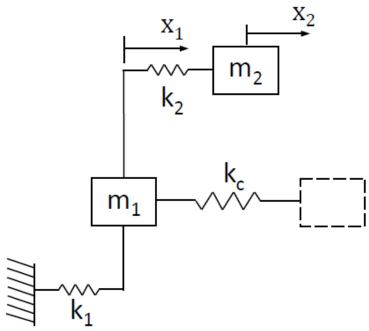

Figure 51: Lumped parameters model of the fundamental sector

By considering adjacent sectors, the entire structure can be obtained, simply by repeating N times the fundamental sector model. Figure 52 shows the fundamental sector coupled with the two adjacent sectors:

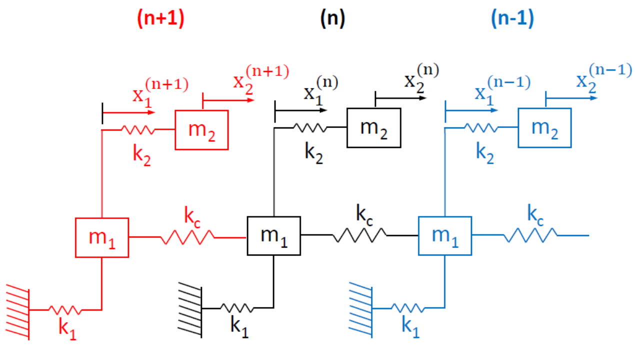

Figure 52: Fundamental sector coupled with adjacent sectors

Considering the lumped parameters model shown in previous figure, the equation of motion of the fundamental sector n can be written as follow:

$$\begin{cases} m_1\ddot{x_1}^{(n)} + k_1 x_1^{(n)} + k_2(x_2^{(n)} - x_1^{(n)}) + k_c(x_1^{(n)} - x_1^{(n-1)}) + k_c(x_1^{(n)} - x_1^{(n+1)}) = 0 \\ m_2\ddot{x_2}^{(n)} + k_2(x_2^{(n)} - x_1^{(n)}) = 0 \end{cases} \tag{46}$$

Writing the previous set of equations in matrix formulation we obtain:

$$
\begin{bmatrix} m_1 & 0 \\ 0 & m_2 \end{bmatrix} \begin{Bmatrix} \ddot{x}_1{}^{(n)} \\ \ddot{x}_2{}^{(n)} \end{Bmatrix} + \begin{bmatrix} k_1 + k_2 + 2k_c & -k_2 \\ -k_2 & k_2 \end{bmatrix} \begin{Bmatrix} x_1^{(n)} \\ x_2^{(n)} \end{Bmatrix} + \\
+ \begin{bmatrix} -k_c & 0 \\ 0 & 0 \end{bmatrix} \begin{Bmatrix} x_1^{(n-1)} \\ x_2^{(n-1)} \end{Bmatrix} + \begin{bmatrix} -k_c & 0 \\ 0 & 0 \end{bmatrix} \begin{Bmatrix} x_1^{(n+1)} \\ x_2^{(n+1)} \end{Bmatrix} = \begin{Bmatrix} 0 \\ 0 \end{Bmatrix} \tag{47}
$$

Equation 47 can be written in more compact form as follow:

$$
\left[m^{(n)}\right]\left\{\ddot{x}^{(n)}\right\} + \left[k^{(n)}\right]\left\{x^{(n)}\right\} + \left[k_c^{(n)}\right]\left\{x^{(n-1)}\right\} + \left[k_c^{(n)}\right]\left\{x^{(n+1)}\right\} = 0 \tag{48}
$$

Equation 48 was obtained for the n-th sector, but it can be written for all sectors of the bladed disk since they are all identical to each other. It is interesting to dwell on the equation for the first sector, $n = 1$, and the last, $n = N$. Consider the diagram in Figure 53 :

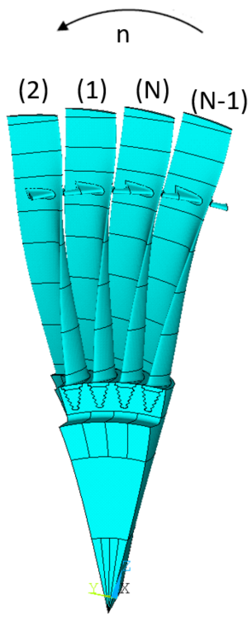

Figure 53: Portion of bladed disk

Writing the equilibrium equations for $n = 1$ and $n = N$ the following expressions are obtained:

$$
\left[m^{(1)}\right]\left\{\ddot{x}^{(1)}\right\} + \left[k^{(1)}\right]\left\{x^{(1)}\right\} + \left[k_c^{(1)}\right]\left\{x^{(N)}\right\} + \left[k_c^{(1)}\right]\left\{x^{(2)}\right\} = 0 \tag{49}
$$

$$\left[m^{(N)}\right]\left\{\ddot{x}^{(N)}\right\}+\left[k^{(N)}\right]\left\{x^{(N)}\right\}+\left[k_c^{(N)}\right]\left\{x^{(N-1)}\right\}+\left[k_c^{(N)}\right]\left\{x^{(1)}\right\}=0 \tag{50}$$

Looking at Equation 49 and Equation 50, the same argument can be applied to all the sectors of the bladed disk, obtaining a set of coupled equations:

$$\left[m^{(1)}\right]\left\{\ddot{x}^{(1)}\right\}+\left[k^{(1)}\right]\left\{x^{(1)}\right\}+\left[k_c^{(1)}\right]\left\{x^{(N)}\right\}+\left[k_c^{(1)}\right]\left\{x^{(2)}\right\}=0 \tag{51}$$

$$\left[m^{(2)}\right]\left\{\ddot{x}^{(2)}\right\}+\left[k^{(2)}\right]\left\{x^{(2)}\right\}+\left[k_c^{(2)}\right]\left\{x^{(1)}\right\}+\left[k_c^{(2)}\right]\left\{x^{(3)}\right\}=0 \tag{52}$$

$$\vdots$$

$$\left[m^{(n)}\right]\left\{\ddot{x}^{(n)}\right\}+\left[k^{(n)}\right]\left\{x^{(n)}\right\}+\left[k_c^{(n)}\right]\left\{x^{(n-1)}\right\}+\left[k_c^{(n)}\right]\left\{x^{(n+1)}\right\}=0 \tag{53}$$

$$\vdots$$

$$\left[m^{(N-1)}\right]\left\{\ddot{x}^{(N-1)}\right\}+\left[k^{(N-1)}\right]\left\{x^{(N-1)}\right\}+\left[k_c^{(N-1)}\right]\left\{x^{(N-2)}\right\}+\left[k_c^{(N-1)}\right]\left\{x^{(N)}\right\}=0 \tag{54}$$

$$\left[m^{(N)}\right]\left\{\ddot{x}^{(N)}\right\}+\left[k^{(N)}\right]\left\{x^{(N)}\right\}+\left[k_c^{(N)}\right]\left\{x^{(N-1)}\right\}+\left[k_c^{(N)}\right]\left\{x^{(1)}\right\}=0 \tag{55}$$

The equilibrium equations written for all sectors of the bladed disk is a set of coupled equations because in each one the displacements of adjacent sectors are involved. This set of equations can be assembled in matrix formulation, resulting in the equation of motion of the entire structure:

$$\left[M\right]\left\{\ddot{X}\right\}+\left[K\right]\left\{X\right\}=0 \tag{56}$$

From Equation 56 modal informations of the bladed disk, in terms of natural frequencies and eigenvectors, can be obtained. The main drawback of this procedure is the computational effort, in fact the mass and the stiffness matrices are obtained for the full structure, so all DOFs for all sectors must me considered for the modal analysis.

In next subchapter the cyclic symmetry boundary conditions will be applied to the fundamental sector, this make possible to compute the eigenvectors of the entire structure by simply rotating the fundamental sector ones.

C.1.1 Cyclic symmetry boundary conditions

To better understand how cyclic symmetry conditions modify the equilibrium equations, consider that a structure in cyclic symmetry admits different mode shapes, but with a common characteristic: the considered eigenvector must be the same also after a $\frac{2\pi}{N}$(angle of a single sector) rotation.
Let's consider an eigenvector Φ associated to a natural frequency ω_n of the bladed disk:

$$\left\{\Phi\right\} = \begin{Bmatrix} \Phi^{(1)} \\ \Phi^{(2)} \\ \vdots \\ \Phi^{(n)} \\ \vdots \\ \Phi^{(N-1)} \\ \Phi^{(N)} \end{Bmatrix} \tag{57}$$

Rotating the eigenvector Φ by an angle equal to single sector angle, $\frac{2\pi}{N}$, another vector, that will be called $\Phi^{'}$, is obtained:

$$\left\{\Phi^{'}\right\} = \begin{Bmatrix} \Phi^{(N)} \\ \Phi^{(1)} \\ \vdots \\ \Phi^{(n-1)} \\ \vdots \\ \Phi^{(N-2)} \\ \Phi^{(N-1)} \end{Bmatrix} \tag{58}$$

The two eigenvectors $\left\{\Phi\right\}$ and $\left\{\Phi^{'}\right\}$ are not necessarily orthogonal, but if $\left\{\Phi^{'}\right\}$ is an eigenvector associated to the same natural frequency, must exist another eigenvector, $\left\{\hat{\Phi}\right\}$, orthogonal to $\left\{\Phi\right\}$, such that:

$$\left\{\Phi'\right\} = c\left\{\Phi\right\} + s\left\{\hat{\Phi}\right\} \tag{59}$$

If $\left\{\Phi'\right\}$ is an eigenvector of the system, the following equation must be verified:

$$\left(-\omega_n^2\left[M\right] + \left[K\right]\right)\left\{\Phi'\right\} = 0 \tag{60}$$

Substituting Equation 59 in Equation 60 we obtain:

$$\left(-\omega_n^2\left[M\right] + \left[K\right]\right)\left(c\left\{\Phi\right\} + s\left\{\hat{\Phi}\right\}\right) = 0 \tag{61}$$

$\left\{\Phi\right\}$ is an eigenvector of the system, thus looking at Equation 61 is clear that also $\left\{\hat{\Phi}\right\}$ is an eigenvector.
Assuming that the three eigenvectors are normalized, it can be written:

$$\left\{\Phi'\right\}^T\left\{\Phi'\right\} = \left(c\left\{\Phi\right\} + s\left\{\hat{\Phi}\right\}\right)^T\left(c\left\{\Phi\right\} + s\left\{\hat{\Phi}\right\}\right) = 1 \tag{62}$$

$$c^2\left\{\Phi\right\}^T\left\{\Phi\right\} + cs\left\{\Phi\right\}^T\left\{\hat{\Phi}\right\} + sc\left\{\hat{\Phi}\right\}^T\left\{\Phi\right\} + s^2\left\{\hat{\Phi}\right\}^T\left\{\hat{\Phi}\right\} = 1 \tag{63}$$

From Equation 63, simplifying the identical terms and considering that the eigenvectors are assumed normalized can be obtained:

$$c^2 + s^2 = 1 \tag{64}$$

Equation 64 shows that the coefficients c and s are the trigonometric functions $cos(\varphi)$ and $sin(\varphi)$. This result suggests that exist another eigenvector $\left\{\hat{\Phi}'\right\}$, orthogonal to $\left\{\Phi'\right\}$, such that this couple of eigenvectors can be obtained starting from $\left\{\Phi\right\}$ and $\left\{\hat{\Phi}\right\}$ by rigid rotation of an angle φ. The relationship between these two couples of eigenvectors can be written as follow:

$$\begin{Bmatrix} \Phi' \\ \hat{\Phi}' \end{Bmatrix} = \begin{bmatrix} I_J cos\left(\varphi\right) & I_J sin\left(\varphi\right) \\ -I_J sin\left(\varphi\right) & I_J cos\left(\varphi\right) \end{bmatrix} \begin{Bmatrix} \Phi \\ \hat{\Phi} \end{Bmatrix} \tag{65}$$

In Equation 65 The term I_J is the identity matrix that have the dimensions equal to the number of the DOFs of the full system.
Equation 65 provides an important result, in fact starting from the displacements of the fundamental sector, the field of displacements of each sector can be obtained by rotating the eigenvector through the rotation matrix, that can be defined as $\left[R_{\varphi}\right]$.
Summarizing what was discussed previously, considering an eigenvector computed for the n-th sector, starting from this result the displacements of the other sectors can be obtained with its own rigid rotation.
From mathematical point of view this means that given two orthogonal and normalized eigenvectors, their own linear combination provides another eigenvector of the structure, so the general following equation can be written:

$$\left\{\Phi'\right\} = a\left\{\Phi\right\} + b\left\{\hat{\Phi}\right\} \tag{66}$$

In Equation 66, the coefficients a and b can be real or complex, leading to two different cases:

1. If the coefficients are real the resulting eigenvector is real. From the physical point of view all sectors are vibrating with the same in phase mode shape, this means that all the blades reach the maximum amplitude, the zero and the minimum Amplitude at the same time instant.

2. If a and b are complex numbers, then the resulting eigenvector will be complex. The physical meaning of this result is that all the blades are vibrating with the same mode shape, but between two adjacent sectors there is a phase shift in terms of amplitude, in fact they do not reach the maximum amplitude, the zero and the minimum amplitude at the same time instant.

Let's focus on the second case, assuming that $\left\{\bar{\Theta}\right\}$ is an eigenvector of the structure:

$$\left\{\bar{\Theta}\right\} = \begin{Bmatrix} \bar{\Theta}^{(1)} \\ \bar{\Theta}^{(2)} \\ \vdots \\ \bar{\Theta}^{(n)} \\ \vdots \\ \bar{\Theta}^{(N-1)} \\ \bar{\Theta}^{(N)} \end{Bmatrix} \tag{67}$$

Rotating $\left\{\bar{\Theta}\right\}$ by an angle equal to the sector amplitude, another eigenvector, that will be called $\left\{\bar{\Theta}'\right\}$, is obtained:

$$\left\{\bar{\Theta}'\right\} = \begin{Bmatrix} \bar{\Theta}^{(N)} \\ \bar{\Theta}^{(1)} \\ \vdots \\ \bar{\Theta}^{(n-1)} \\ \vdots \\ \bar{\Theta}^{(N-2)} \\ \bar{\Theta}^{(N-1)} \end{Bmatrix} \tag{68}$$

Observing Equation 67 and Equation 68 the following relationship can be written:

$$\left\{\bar{\Theta}'\right\} = \left\{\bar{\Theta}\right\} e^{-i\varphi} \tag{69}$$

For the single sector:

$$\left\{\bar{\Theta}^{(n-1)}\right\} = \left\{\bar{\Theta}^{(n)}\right\} e^{-i\varphi} \tag{70}$$

Equation 70 defines an important relationship between the displacements of the n-th sector and the adjacent ones. It is important to make another step on the φ angle, in fact it cannot assume any value because after N rotations the displacements of the first sector must be obtained. Considering this, the following expressions can be written:

$$N\varphi = h2\pi \tag{71}$$

$$\varphi = h\frac{2\pi}{N} \tag{72}$$

In Equation 72:

- φ is the Interphase Blade Angle (IPBA), it defines the displacement phase shift between two adjacent sectors.
- h is the harmonic index.
- N is the number of sectors of the cyclic structure.

Varying the φ angle there are different modes:

a. When $\varphi = 0$ there is no phase shift, thus all sectors are vibrating in phase, reaching at the same time the same displacement value.

b. When φ=π adjacent sectors vibrate completely out of phase. In this case adjacent sectors reach the maximum amplitude and the zero at the same time.

c. For all the other values of φ there is a phase shift between adjacent sectors, this means that they reach the same displacement value with different times. This physically describes a rotating exciting wave.

The first two mode types are real modes, while the type c modes are complex modes. The next step is to use the cyclic symmetry boundary conditions for writing the equation of motion of the fundamental sector as function of the harmonic index. This allow to compute the modal analysis of the entire structure expanding the results obtained for the fundamental sector.
Before being able to accomplish this step, a further consideration about the harmonic index is necessary. The harmonic index values that have a real physical meaning are ranged between 0 and $\frac{N}{2}$. Let's make it clear with a simple example: suppose to have a bladed disk with 4 blades, all possible values of the harmonic index are:

1. $h = 0$: $\varphi = 0$
2. $h = 1$: $\varphi = \frac{\pi}{2}$
3. $h = 2$: $\varphi = \pi$
4. $h = 3$: $\varphi = \frac{3\pi}{2}$
5. $h = 4$: $\varphi = 2\pi$

Analyzing the previous relationships can be observed that for $h = 4$ the phase shift is 2π, which means that the eigenvector computed for the n-th sector return itself. This, from physical point of view, implies that the case 5 is equivalent to the case 1. Let's now look at case 4: for this case the phase shift is equal to the phase shift of the case 2, but with the opposite sign. The shift function is:

$$e^{i\varphi} \tag{73}$$

Considering that the shift function is periodic, can be written:

$$e^{ih\frac{2\pi}{N}} = e^{i\left(h\frac{2\pi}{N} - 2\pi\right)} = e^{i\left(h - N\right)\frac{2\pi}{N}} \tag{74}$$

Let's now consider Equation 74 applied to the previous example: with $h = 3$, that for the given example correspond to $N-1$, the phase shift is $e^{-i\frac{2\pi}{N}}$, that is the same phase shift obtained with $h = 1$, but with the opposite sign. From physical point of view this situation represent a traveling excitation wave that is rotating in the opposite direction, but with the same phase shift. The main outcome of these considerations is that values of harmonic index between $\frac{N}{2}$ and N do not give additional informations, in fact they give back the same phase shift of harmonic indexes ranged between 0 and $\frac{N}{2}$, but considering a traveling excitation wave in the opposite direction.

C.1.2 Equation of motion of the fundamental sector with cyclic symmetry boundary conditions

In previous subchapter the cyclic symmetry boundary conditions were widely discussed. In this susbsection these boundary conditions will be applied to the equation of motion of the fundamental sector. Let's consider Equation 46 and let's rewrite it in frequency domain:

$$\begin{cases} -\omega^2 m_1 \bar{X_1}^{(n)} + k_1 \bar{X_1}^{(n)} + k_c\left(\bar{X_1}^{(n)} - \bar{X_1}^{(n-1)}\right) + k_c\left(\bar{X_1}^{(n)} - \bar{X_1}^{(n+1)}\right) + k_2\left(\bar{X_2}^{(n)} - \bar{X_1}^{(n)}\right) = 0 \\ -\omega^2 m_2 \bar{X_2}^{(n)} + k_2\left(\bar{X_2}^{(n)} - \bar{X_1}^{(n)}\right) = 0 \end{cases} \tag{75}$$

Now, considering what was obtained in previous subchapter in Equation 70, the displacements of the (n-1)-th sector can be expressed as function of the displacements of the n-th sector. This result can be expanded also to the (n+1)-th sector. Considering this result, Equation 75 can be rewritten as follow:

$$\begin{cases} -\omega^2 m_1 \bar{X_1}^{(n)} + k_1 \bar{X_1}^{(n)} + k_c\left(\bar{X_1}^{(n)} - \bar{X_1}^{(n)} e^{-ih\frac{2\pi}{N}}\right) + k_c\left(\bar{X_1}^{(n)} - \bar{X_1}^{(n)} e^{ih\frac{2\pi}{N}}\right) + k_2\left(\bar{X_2}^{(n)} - \bar{X_1}^{(n)}\right) = 0 \\ -\omega^2 m_2 \bar{X_2}^{(n)} + k_2\left(\bar{X_2}^{(n)} - \bar{X_1}^{(n)}\right) = 0 \end{cases} \tag{76}$$

Writing all in matrix formulation:

$$\left(-\omega^2\begin{bmatrix} m_1 & 0 \\ 0 & m_2 \end{bmatrix} + \begin{bmatrix} k_1+2k_c-k_c e^{-ih\frac{2\pi}{N}}-k_c e^{ih\frac{2\pi}{N}} & -k_2 \\ -k_2 & k_2 \end{bmatrix}\right)\begin{Bmatrix} \bar{X_1}^{(n)} \\ \bar{X_2}^{(n)} \end{Bmatrix} = 0 \tag{77}$$

Equation 77 represent the equation of motion of the fundamental sector with cyclic symmetry boundary conditions. Using this formulation is possible to compute the displacement for all sectors just varying the harmonic index, leading to less computational effort respect to the formulation obtained in Equation 56, in which the full matrices of the system must be computed.
This subsection concludes the modal properties of structures with cyclic symmetry boubdary conditions, the next step is to discuss about the forced response of cyclic structures, that is a necessary step to compute the vibration amplitudes.

C.2 Forced response of cyclic structures

The starting point for calculating the forced response of bladed disks is to understand the forcings that can act on the rotor blades. The fluid pressure field is not axisymmetric due to the fact that before and after the rotor stage there are stator stages. Considering a point on a rotor sector, during the rotation it feels a time-variant pressure, which returns to initial value after a complete rotor revolution.
Taking these considerations into account, the trend of the aerodynamic forcing acting on the rotor blades has a periodic pattern with a number of peaks equal to the number of stator sectors. An example of aerodynamic force acting on bladed disk sectors is shown in Figure 54:

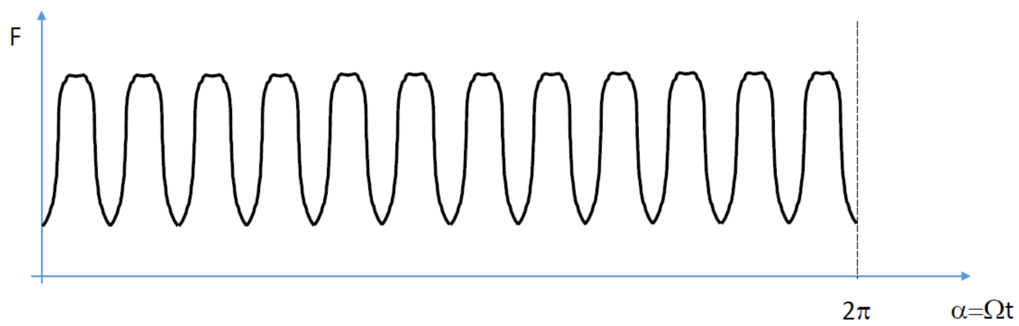

Figure 54: Aerodynamic force

The force shown in Figure 54 is periodic, so it can be written as Fourier series:

$$F\left(\alpha\right) = F_0 + \sum_{eo} F_c^{(eo)} cos\left(eo\alpha\right) + F_s^{(eo)} sin\left(eo * \alpha\right) = F_o + \sum_{eo} F^{(eo)} cos\left(eo\alpha + \delta\right) \tag{78}$$

$$F^{(eo)} = \sqrt{F_c^{(eo)^2} + F_s^{(eo)^2}} \tag{79}$$

As an example, consider an aerodynamic force with one engine order component, for this case let's take $eo = 3$. The trend over time of the considered component is shown in Figure 55:

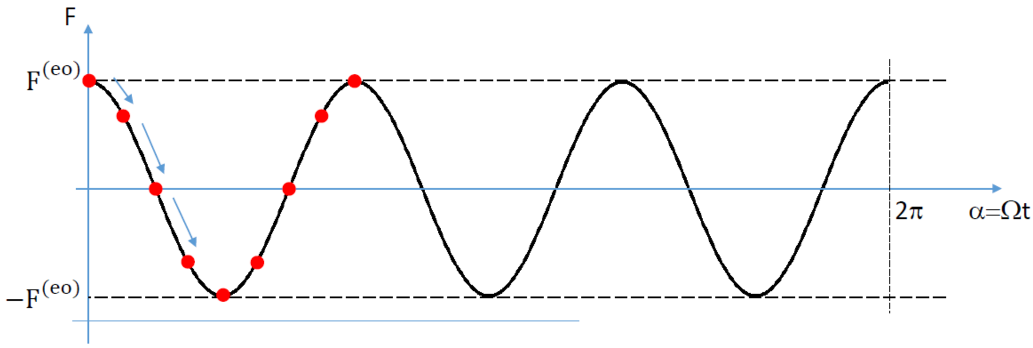

Figure 55: Aerodynamic force whith $eo = 3$ acting on n-th sector

In Figure 55 the red dot indicates the force that feels the $n - th$ sector at a certain time instant, which can be expressed as follows:

$$F^{(n)} = F^{(eo)} cos\left(eo\Omega t + \delta\right) \tag{80}$$

in which $eo\Omega = \omega$ is the pulsation of the forcing term.
Let's now consider two adjacent sectors, n and $n+1$, that are moving on the previous forcing curve:

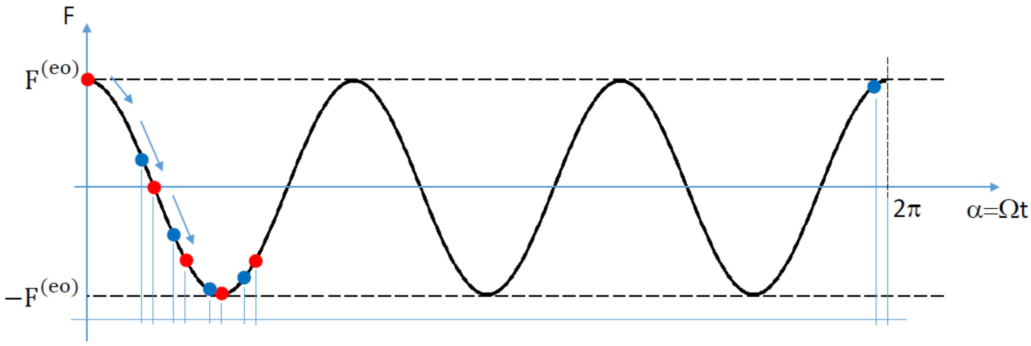

Figure 56: Aerodynamic force with $eo = 3$ acting on the $n-th$ sector and $n+1$ sector

In Figure 56 the red dot represents the n-th sector, while the blue one is the n+1 sector. The $n+1$ sector is shifted in space relative to the n sector by an angle equal to that of the fundamental sector, $\frac{2\pi}{N}$, this causes the force that feels the $n-th$ sector at a certain instant to be felt by the $n+1$ sector with a certain time delay Δt, which can be obtained by considering that the angular space traveled in time Δt by the $n+1$ sector at angular velocity Ω is:

$$\Omega \Delta t = \frac{2\pi}{N} \tag{81}$$

so:

$$\Delta t = \frac{2\pi}{N\Omega} \tag{82}$$

Considering what was obtained in Equation 80 and Equation 82 the force felt by $n+1$ sector can be written as follow:

$$F^{(n+1)} = F^{(eo)} cos\Big(\omega(t-\Delta t)+\delta\Big) \tag{83}$$

Substituting Equation 82 in Equation 83 the following expression is obtained:

$$F^{(n+1)} = F^{(eo)} cos\Big(\omega(t-\tfrac{2\pi}{N\Omega})+\delta\Big) = F^{(eo)} cos\Big(\omega t-\Psi+\delta\Big) \tag{84}$$

in which $\Psi = eo\frac{2\pi}{N}$. From Equation 84 it can be observed that, for a fixed engine order value, two adjacent sectors feel an aerodynamic force with a time phase shift equal to Ψ.

The expression of force acting on the $n-th$ sector and on the $n+1$ sector can be written in complex notation as follows:

$$F^{(n)} = F^{(eo)} e^{i\omega t} e^{i\delta} = \bar{F}^{(eo)} e^{i\omega t} \tag{85}$$

$$F^{(n+1)} = F^{(eo)} e^{i\omega t} e^{i\delta} e^{-i\Psi} = F^{(n)} e^{-i\Psi} \tag{86}$$

In order to evaluate the potential resonances of a bladed disk, in addition to mathematically defining the aerodynamic forcing acting on the blades, it is important to have a graphical tool to directly visualize the potential resonances of the machine. This graphical tool is the Campbell diagram and is constructed as shown in Figure 57:

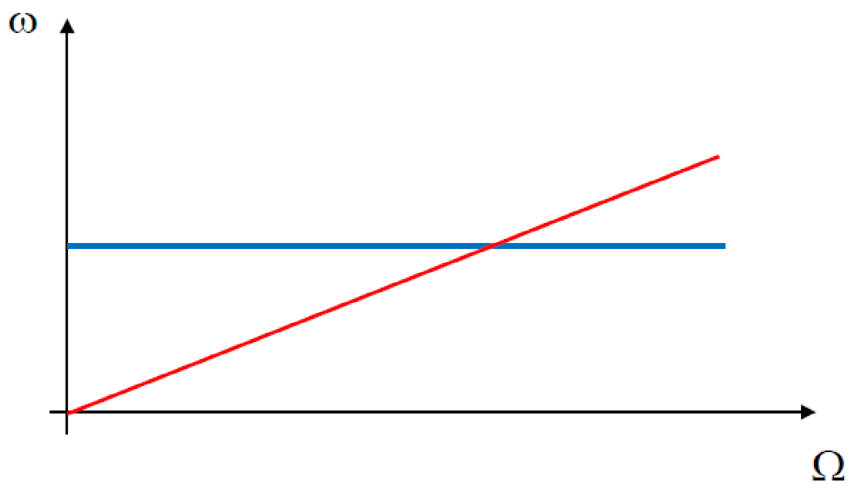

Figure 57: Campbell diagram

The Campbell diagram represents the forcing pulsation as function of the angular velocity of the bladed disk. In Figure 57 the red line is the forcing pulsation, that is defined as $\omega = eo\Omega$, while the blue one is a potential natural frequency of the bladed disk. In this simplified representation the stiffening effect due to the centrifugal force is neglected, in fact the natural frequency has the same value for all angular velocities.
Figure 57 shows an example of a Campbell diagram and its usefulness, consider now a more realistic example to better understand the use of this graphical tool. Let's consider a bladed disk with six blades and let's take only the first modal family. The harmonic index in this example can assume values from 0 to 3, according to what was discussed in previous subsection, so on the Campbell diagram there are four blue lines, each natural frequency associated to each harmonic index. Considering an aerodynamic force composed by three engine orders components, the resulting diagram is shown in Figure 58:

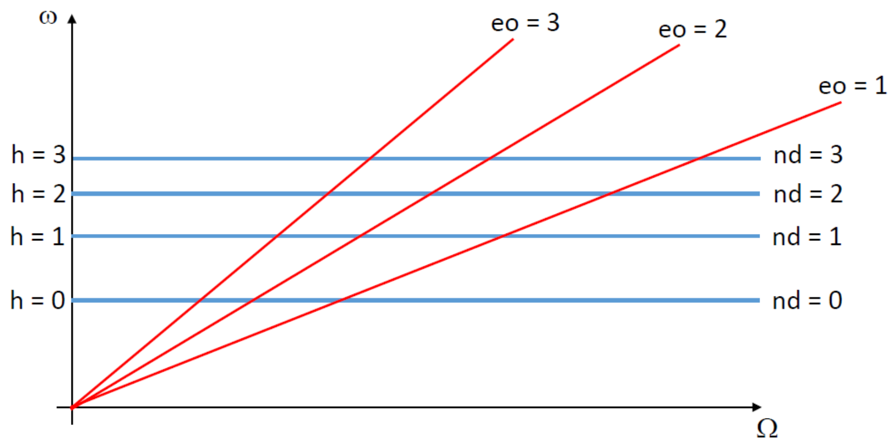

Figure 58: Campbell diagram for a bladed disk with six blades

Observing Figure 58 several crossings between the pulsation of the exciting force and the natural frequencies of the system can be identified. However, it is important to understand whether all the crossings are actually potential resonances. In order to understand this, consider the generic equation of motion of a system with N degrees of freedom, written in m-normalized coordinates:

$$\left[\Phi\right]^T\left(-\omega^2\left[M\right]+i\omega\left[C\right]+\left[K\right]\right)\left[\Phi\right]\left\{\bar{q}\right\}=\left[\Phi\right]^T\left\{\bar{F}\right\} \tag{87}$$

Equation 87 is written in m-normalized modal coordinates, so the system of equations become diagonal:

$$\left(-\omega^2+i\omega diag(c_n)+diag(\omega_n^2)\right)\left\{\bar{q}\right\}=\left[\Phi\right]^T\left\{\bar{F}\right\} \tag{88}$$

For the n-th mode the vibration amplitude in m-normalized modal coordinates can be expressed as follows:

$$\bar{q}_n=\frac{\left[\Phi_n\right]^T\left\{\bar{F}\right\}}{-\omega^2+i\omega c_n+\omega_n^2} \tag{89}$$

It is clear from Equation 89 that for the vibration amplitude to be different from zero the product $\left[\Phi_n\right]^T\left\{\bar{F}\right\}$ must be different from zero. This means that the projection of the force vector on the n-th mode, for a given engine order, must be non null.

Let's consider a generic cross between a forcing term with a certain *eo* and a natural frequency of the system for harmonic index *h*. Imaging that the force acting on the single sector is a point-concentrated force, the resulting force and displacements vectors can be written as follows:

$$\left\{F_p\right\} = F_p^{(1)} \begin{Bmatrix} 1 \\ e^{-i\Psi} \\ \vdots \\ e^{-i(n-1)\Psi} \\ \vdots \\ e^{-i(N-2)\Psi} \\ e^{-i(N-1)\Psi} \end{Bmatrix} \qquad \Psi = eo\frac{2\pi}{N} \tag{90}$$

$$\left\{\bar{\Theta}_p\right\} = \left\{\bar{\Theta}_p^{(1)}\right\} \begin{Bmatrix} 1 \\ e^{-i\varphi} \\ \vdots \\ e^{-i(n-1)\varphi} \\ \vdots \\ e^{-i(N-2)\varphi} \\ e^{-i(N-1)\varphi} \end{Bmatrix} \qquad \varphi = h\frac{2\pi}{N} \tag{91}$$

At this point the scalar product between the displacements vector and the force vector can be computed:

$$\left\{\bar{\Theta}_p\right\}^T \left\{F_P\right\} = \sum_{n=0}^{n=N-1} e^{inh\frac{2\pi}{N}} e^{-ineo\frac{2\pi}{N}} = \sum_{n=0}^{n=N-1} e^{in(h-eo)\frac{2\pi}{N}} \tag{92}$$

Looking at Equation 92, two different cases can be distinguished:

1. $$eo = h : \sum_{n=0}^{n=N-1} e^{-in(h-eo)\frac{2\pi}{N}} = N \tag{93}$$

2. $$eo \neq h : \sum_{n=0}^{n=N-1} e^{-in(h-eo)\frac{2\pi}{N}} = 0 \tag{94}$$

Observing Equation 93 and Equation 94 what stands out is that the scalar product between the displacements vector and the force one is not null only when the engine order is equal to the harmonic index. This implies that not all the crossings in Figure

58 represents real resonances of the bladed disk. The only three crossings that lead to the resonance of the system are those such that $eo = h$, they are shown in Figure 59:

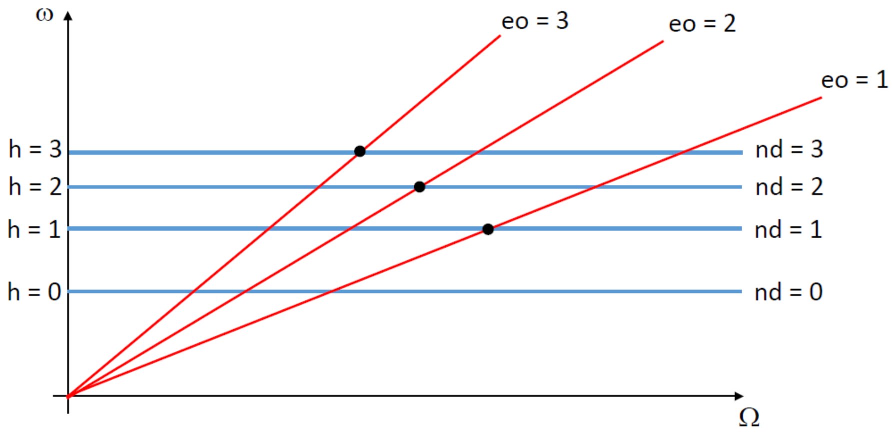

Figure 59: Resonance conditions for a bladed disk with six blades

Before concluding the discussion about the forced response of bladed disks, it is important to make a further clarification regarding the engine order.
The harmonic index can assume values from 0 to $N-1$, while the engine order can also assume higher values than $N-1$. In order to extend the result obtained in Equation 92 to this case the value of the engine order can be written as follows:

$$eo = KN + eo' \tag{95}$$

Substituting Equation 95 in Equation 92:

$$\left\{\bar{\Theta}_p\right\}^T \left\{F_P\right\} = \sum_{n=0}^{n=N-1} e^{inh\frac{2\pi}{N}} e^{-ineo\frac{2\pi}{N}} e^{-iK2\pi} = \sum_{n=0}^{n=N-1} e^{in(h-eo')\frac{2\pi}{N}} \tag{96}$$

In this case, the resonance condition occurs for $eo' = h$. Let's consider as example a bladed disk with 40 sectors excited by a force with $eo = 37$. To detect the potential resonances, according to Equation 95 eo' can be calculated as: $eo' = KN - eo$. Considering $N = 40$ and $K = 1$, $eo' = -3$. The resonance occurs when $eo' = h$, so in this case the mode shapes associated to harmonic index three are excited. In Figure 60is represented the resonance condition on the Campbell diagram:

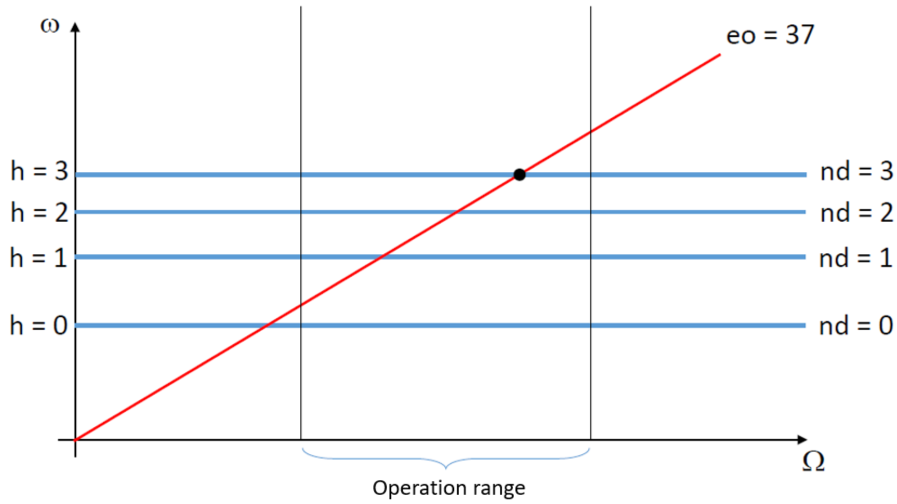

Figure 60: Campbell diagram for a bladed disk with 40 sectors excited by $eo = 37$ external excitation

This consideration about the engine order concludes the discussion about the forced response of bladed disks.